Title

The Kinetics of Dislocation Loop Formation in Ferritic Alloys Through the Aggregation of Irradiation Induced Defects

Author

Kohnert, Aaron

Publication Date

2014

The Kinetics of Dislocation Loop Formation in Ferritic Alloys Through the Aggregation of Irradiation Induced Defects

by

Aaron Anthony Kohnert

A dissertation submitted in partial satisfaction of the
requirements for the degree of
Doctor of Philosophy

in

Nuclear Engineering

and the Designated Emphasis

in

Computational Science and Engineering

in the

Graduate Division

of the

University of California, Berkeley

Committee in charge:

Professor Eric Norman, Co-chair
Professor Brian Wirth, Co-chair
Associate Professor Jon Wilkening

Spring 2014

Abstract

The Kinetics of Dislocation Loop Formation in Ferritic Alloys Through the Aggregation of Irradiation Induced Defects

by

Aaron Anthony Kohnert

Doctor of Philosophy in Nuclear Engineering

Designated Emphasis in Computational Science and Engineering

University of California, Berkeley

Professor Eric Norman, Co-chair

Professor Brian Wirth, Co-chair

The mechanical properties of materials are often degraded over time by exposure to irradiation environments, a phenomenon that has hindered the development of multiple nuclear reactor design concepts. Such property changes are the result of microstructural changes induced by the collision of high energy particles with the atoms in a material. The lattice defects generated in these recoil events migrate and interact to form extended damage structures.

This study has used theoretical models based on the mean field chemical reaction rate theory to analyze the aggregation of isolated lattice defects into larger microstructural features that are responsible for long term property changes, focusing on the development of black dot damage in ferritic iron based alloys. The purpose of such endeavors is two-fold. Primarily, such models explain and quantify the processes through which these microstructures form. Additionally, models provide insight into the behavior and properties of the point defects and defect clusters which drive general microstructural evolution processes.

The modeling effort presented in this work has focused on physical fidelity, drawing from a variety of sources of information to characterize the unobservable defect generation and agglomeration processes that give rise to the observable features reported in experimental data. As such, the models are based not solely on isolated point defect creation, as is the case with many older rate theory approaches, but instead on realistic estimates of the defect cluster population produced in high energy cascade damage events. Experimental assessments of the microstructural changes evident in transmission electron microscopy studies provide a means to measure the efficacy of the kinetic models. Using common assumptions of the mobility of defect clusters generated in cascade damage conditions, an unphysically high density of damage features develops at the temperatures of interest with a temperature dependence that is much too strong.

The so-called nucleation catastrophe motivates a re-examination of the properties of interstitial defect clusters in iron. The behavior of interstitial clusters in iron is a complex puzzle, with high mobility predicted by computational techniques, much lower thermal mobility observed in electron microscopes, and a series of discrete discontinuous motions seen during *in situ* ion irradiation performed in a transmission electron microscope. This work has combined these observations and presented a trap mediated concept of interstitial cluster motion that has been incorporated into a larger scale kinetic model. This superior description of interstitial mobility is crucial to realizing many aspects of black dot damage structures, from saturation behavior to temperature dependence.

Another focus of this work was to analyze the assumptions widely employed in rate theory models. Cluster dynamics, the rate theory method employed in this work, is usually invoked with a number of potentially dubious assumptions regarding the mobility and interaction characteristics of defect clusters. The effects of anisotropic reaction volumes and one dimensional diffusion have both been analyzed to determine the effect they have on the development of black dot microstructures. In the trap mediated system, one dimensional diffusion proved far more significant, and the cross section for interaction between one dimensionally diffusing interstitial clusters strongly influenced the size and density of visible damage structures. The validity of the reaction rate approach to determining cluster evolution in the trap mediated environment has been established by comparison with Monte Carlo methods.

In total, this work has demonstrated the ability of mean field models to capture the key characteristics of low temperature damage microstructures in irradiated ferritic alloys when incorporating the full knowledge of interstitial cluster properties in iron, and the legitimacy of the mean field assumptions by comparison to other methods.

Contents

Contents **i**

List of Figures **iii**

List of Tables **v**

1 Introduction **1**

2 Background **5**
- 2.1 Ferritic/Martensitic Steels 5
- 2.2 Mean Field Rate Theory 10

3 Methods **15**
- 3.1 Cluster Dynamics 15
  - 3.1.1 Reaction 16
  - 3.1.2 Dissociation 18
  - 3.1.3 Sinks 20
- 3.2 Additional Methods 21
  - 3.2.1 Object Kinetic Monte Carlo 21
  - 3.2.2 Molecular Dynamics 23

4 Defect Clusters in Ferritic Systems **25**
- 4.1 Defect Properties 26
  - 4.1.1 Vacancy Defects 26
  - 4.1.2 Interstitial Defects 27
  - 4.1.3 Interaction Properties 30
- 4.2 Parameter Selections 32

5 Primary Damage **36**
- 5.1 Source Term Calculations 36
  - 5.1.1 Recoil Distribution Estimates 38
  - 5.1.2 Defect Clustering and Survival 41
- 5.2 Long Term Evolution 45

6 Irradiation Activated Motion 50
6.1 Trap Mediation 50
6.1.1 Detrapping Simulations 51
6.1.2 Modeling Discontinuous Motion 54
6.2 Effects of Trap Mediation Kinetics 57
6.2.1 Prompt Reaction of Cascade Debris 57
6.2.2 Detrapping with Cascade Damage 59
6.2.3 Detrapping with Frenkel Pair Damage 64

7 Reaction Kinetics 67
7.1 Non-spherical Reaction Geometries 67
7.1.1 Defect Interaction with Dislocation Loops 68
7.1.2 Effects on Defect Evolution 71
7.2 One Dimensional Diffusion 75
7.2.1 Impact on Reaction Rates 75
7.2.2 Cross Sections 77
7.2.3 Defect Evolution with One Dimensional Diffusion 80
7.3 Kinetic Monte Carlo 86

8 Conclusions 95
8.1 Model Performance 95
8.2 Future Work 98

Bibliography 100

A Implementation and Numerical Methods 110
A.1 Cluster Dynamics 110
A.1.1 Integration Scheme 110
A.1.2 Function Evaluations 118
A.2 Object Kinetic Monte Carlo 120
References 124

List of Figures

2.1 *In situ* trends in damage microstructure evolution in an Fe-12Cr-0.1C F/M model alloy as reported in [12] showing an early saturation in defect density and continuous growth in size across a wide temperature range. 9

3.1 The sink strength multiplication factor for selected dislocation capture radii . . 21

4.1 Configurations for vacancy clusters in the bcc lattice 27
4.2 Configurations for self interstitials and their clusters in the bcc lattice 29
4.3 Crowdion bundle structure viewed in the $\langle 111 \rangle$ direction 30

5.1 Primary damage profile for heavy ion irradiation of iron 40
5.2 Defect production by size for cascades of various energies in bcc Fe 43
5.3 Trends in intra-cascade clustering behavior before and after thermal aging . . . 44
5.4 The effect of interstitial mobility assumption on dislocation loop evolution for Frenkel Pair damage at 300 K 45
5.5 Effects of temperature on loop saturation when damage appears as Frenkel Pairs 46
5.6 Visible loop density trends for cascade damage at 300 K 47
5.7 Comparison of loop saturation behavior for Frenkel Pair and cascade irradiation conditions 48

6.1 Trapping of 91 member interstitial loops using helium as a surrogate impurity . 52
6.2 Cascade impact near a 91 member interstitial loop showing interstitials (large, green) vacancies(small, red) and helium(small, blue) at various stages of cascade evolution 53
6.3 Evolution of cascade damage allowing prompt reactions 58
6.4 Evolution of cascade damage with trap mediated diffusion kinetics absent detrapping effects 59
6.5 Evolution of cascade damage with detrapping effects 60
6.6 Effect of loop interior or dislocation line trap locations on defect development . 61
6.7 Dependence of the saturation density on temperature and trap density with detrapping effects 62
6.8 Loop saturation and growth at 200 K from Frenkel pair damage 65
6.9 Saturation density with detrapping effects for Frenkel pair damage 65

7.1 Interaction possibilities for dislocation loops described by the relative position of glide cylinder axes 70
7.2 Reduction in reaction rate magnitudes for dislocation loops using torroidal reaction volumes 72
7.3 The impact of dislocation loop reaction geometry on visible defect development 74
7.4 Cross section for crowdion bundle reaction with other defects and defect clusters 78
7.5 Reduction in reaction rate magnitudes for one dimensional diffusers 80
7.6 Effect of interstitial cluster interaction cross sections on loop evolution 81
7.7 Comparison of damage evolution between trap different trap mediation approaches with 1D reaction kinetics 82
7.8 Evolution of the vacancy inventory in 1D and 3D trap mediated diffusion based kinetic models 82
7.9 Temperature dependence of black dot development under 1D and 3D reaction-diffusion kinetic frameworks 83
7.10 Impact of trap density on interstitial loop development assuming either 1D or 3D crowdion reaction kinetics. 84
7.11 Evolution of visible damage in KMC compared to CD models, showing comparisons of visible density and size 88
7.12 Net vacancy retention in KMC and CD approaches presented on both linear and logarithmic scales 89
7.13 Net retained and escaped interstitial content. 90
7.14 Depth averaged defect content as a function of cluster size. CD data are represented by points and KMC data are joined. 91
7.15 Density distribution by cluster size for defects larger than 2 nm 92

A.1 Jacobain structure in cluster dynamics 112
A.2 Performance of various preconditioning approaches which include various numbers of sub- and super-diagonals from the reaction block 114
A.3 Mass error as a function of dose 116
A.4 Global error at one second (0.0015 dpa) in bulk simulations using backward Euler integration with fixed time steps. 117
A.5 Coordinate rotations to facilitate checks for coalescence conditions between two dislocation loops. 122

List of Tables

3.1 Choice of interatomic potentials 24

4.1 Delineation between types of point defect clusters 32
4.2 Diffusion parameters for freely migrating interstitials 32
4.3 Two sets of diffusion parameters for freely migrating vacancies 33
4.4 Diffusion parameters for larger interstitial clusters 33
4.5 Capillary law constants for α-Fe (eV) 34
4.6 Default values for the thin foil α-Fe reaction-diffusion system 35

5.1 Heavy ion irradiation specifications for in-situ experiments 36

7.1 Approaches to account for non-spherical geometries of dislocation loops 72

Acknowledgments

Throughout my studies I was fortunate to have an abundance of invaluable advice and support. First and foremost I want to recognize the irreplaceable guidance and mentorship of Professor Brian Wirth. His engaging, compelling approach to irradiation damage drew me into the field, which I knew nothing of five years ago, and spared me from a lifetime of neutronics calculations. Professor Peter Hosemann also offered a rich vein of expertise on the subject. Professor Jon Wilkening assisted with the numerical aspects of my research, providing several suggestions for integration schemes. I want to thank the UCB nuclear engineering faculty in general, and Professor Eric Norman in particular, for accommodating my extended stay in Knoxville to complete this research.

This research would not have been possible without the efforts of our experimental collaborators, Dr. Arthur Motta and Cem Topbasi at Penn State as well as Dr. Djamel Kaoumi at the University of South Carolina. They generated significant *in situ* ion irradiation data, which motivates and informs this work.

Several past and current group members, both at UCB and UTK have collaborated on this work. Dr. Thibault Faney offered much appreciated initial assistance and advice regarding cluster dynamics calculations. My conversations with Drs. Xunxiang Hu, Donghua Xu, and Ben Ramirez were also very helpful in this capacity, particularly Dr. Xu, who also provided advice on kinetic Monte Carlo models. Nathan Capps and Aaron Selby were instrumental in generating the molecular dynamics data included in this document, along with Dr. Karl Hammond.

Finally, I would like to thank my friends and family for support and encouragement throughout.

Chapter 1

Introduction

Designing reliable, safe, and long-lasting nuclear power plants requires extensive knowledge of the constituent materials, not just at the moment the plant is built, but through to the day it is decommissioned. Years of exposure to high energy neutrons can induce changes in the engineering properties of structural materials and accelerate degradation processes. Understanding these phenomenon is essential not only for assessing the continuing viability of currently operating reactors, but also for making next generation reactor concepts a reality. These more ambitious designs generally require higher operating temperatures or pressures, more intense radiation doses, and in some cases a fast (more energetic) neutron spectrum. Understanding the radiation induced property changes that materials will experience in these conditions is just as crucial to a sound plant design as the neutron economy, and in the long term constitutes a much more challenging problem to solve.

Beyond maintenance and improvement of fission reactors lies the development of fusion as a viable energy source. Despite promises of bountiful yields with minimal environmental impacts, the challenges of creating materials to withstand the requirements of a fusion environment have hampered development of this technology for decades. Materials degradation concerns extend beyond merely choosing a high melting point material as a plasma facing component capable of withstanding extreme steady state and transient heat fluxes. The deuterium-tritium fusion process generates a steady flux of neutrons even more energetic than those in a fast fission reactor. These 14 MeV neutrons imply a host of negative consequences in a poorly chosen material, ranging from activation to property degradation concerns not unlike those of the fission environment, but potentially more challenging to resolve or accommodate.

Due to the substantial changes in the properties of structural materials following deployment in an irradiation environment, it is important to quantify the level of radiation exposure a material has endured. The radiation dose delivered to a material is often reported in displacements per atom (dpa), a measure of the amount of damage generated in a material based on the energy deposited through radiation exposure. A typical light water reactor (LWR) pressure vessel receives far fewer than 1 dpa in its operating lifetime while core internals absorb doses around 10 to 50 dpa. Fast reactor and fusion reactor components, on the other hand, will need to absorb a minimum of 100 dpa. Consequently, the materials employed for fast and fusion reactors will need to respond to the radiation exposure in ways that mitigate any degradation in properties.

The property changes arising from irradiation are generally restricted to a few significant phenomenon. The most prominent concerns are volumetric changes, hardening, creep, solute redistribution, and helium embrittlement. The particular degradation process which will occur varies from material to material and even within a material irradiated at different temperatures. A given damage process, should it occur in the material of interest, typically manifests within a characteristic temperature range with respect to the melting point[1].

Of the primary concerns, void swelling is among the most detrimental to operating lifetime. This process occurs at operating temperatures between roughly one third and one half the melting point and features the development of a low number density of cavities within the material which grow to larger sizes as irradiation continues. The material from these cavities is displaced, eventually resulting in dimensional changes in the material itself. Allowed to progress unchecked, the resulting changes in the dimensions of reactor components compromise design integrity in obvious ways. Volumetric swelling is not the only irradiation effect that can change a material's dimensions. Select materials expand in one direction while shrinking in another when exposed to irradiation, without a net change in volume. Such dimensional instability is evident in the zirconium based fuel rod cladding of currently deployed reactors.

At lower temperatures, below about one third of the melting point, radiation can induce hardening and embrittlement in a material. Marked by an increase in the yield strength of the irradiated material in concert with reduced ductility, this category of radiation effect has been of particular interest for the current fleet of LWRs. The reactor pressure vessels of current LWRs have experienced hardening and embrittlement, potentially limiting operational lifespans. These property changes arise from the development of a high density of obstacles which impede the motion of dislocations. These embrittling features take a number of forms and vary from material to material, although primarily they consist of precipitates and lattice defect structures. Embrittlement can occur instead by way of helium bubble formation, but typically at temperatures above half the melting point.

An irradiation environment may accelerate creep, or introduce the possibility of creep rupture where it isn't otherwise a concern, typically below half the melting temperature. In binary alloys and other multi-component systems, radiation exposure may induce segregation of its components, leading to depletion or enrichment at grain boundaries and surfaces. This effect alone may prove sufficient to compromise key material properties, namely corrosion resistance. The redistribution of solutes typically occurs between one third and two thirds of the melting point. Understanding the cause for and the extent of such effects, under which conditions they occur for which materials, remains crucial to selecting and improving materials for irradiation environments.

Long range, long term changes in material properties are the result of a hierarchical progression of much smaller events. The neutron flux through a material results in occasional scattering events through which large amounts of energy are transfered from a neutron to a lattice atom. This primary knock-on atom (PKA) becomes displaced from its lattice site and collides in turn with it's neighbors. Within a few femtoseconds, the energy distributes over a dense, nanometer scale network of displaced atoms in a phenomenon known as a displacement cascade. Some PKAs may be sufficiently energetic to travel some small distance due to channeling effects, but will slow through electronic stopping and form a cascade regardless. Cascade events resolve within a matter of picoseconds, and the underlying crystal structure re-emerges as the affected atoms cool to the ambient temperature.

The reconstituted lattice following a cascade is far from perfect, leaving behind vacant lattice sites at the center of the affected area with the atoms that should be filling them distributed about the periphery in doubly occupied lattice sites. Such lattice defects are known as vacancies and self-interstitials respectively. These defects might appear alone, in bound pairs, or even in larger clusters depending on the size of the cascade and the material in question. This characteristic core-shell structure does not last long at most temperatures, as the interstitial defects are generally highly mobile. Within a few microseconds, the interstitials have diffused far from the locations of their birth, either recombining with vacancies in the core region or escaping the vicinity of the cascade altogether.

The vacancies move on much slower timescales, if they move at all. At sufficiently late times, typically on the order of seconds or longer depending on temperature, the vacancies may escape the cascade region as well, leaving behind a healed lattice. Thus it is not the cascade itself that gives rise to radiation damage effects, but rather the lattice defects which migrate away from it. The aggregation of freely migrating vacancies results in void swelling. The enhanced and perhaps preferential diffusion of impurity or alloying elements amidst the irradiation induced defect supersaturation drives precipitation and segregation. Immobile defect clusters become obstacles to dislocation glide and contribute to hardening.

In this manner, lattice defects drive changes in the microstructure which in turn influence engineering scale mechanical and physical properties. Minimizing changes in the mechanical and physical proterties of a material becomes a matter of slowing or eliminating the microstructural evolution induced by defect generation. This in turn requires materials engineered on a microspcopic scale to promote the intrinsic recombination of vacancies and interstitials, rather than allowing them to agglomerate separately and give rise to damage features. To the extent that damage cannot be mitigated, its formation needs to be at a minimum well understood, such that reactor designs anticipate its formation and the consequences thereof.

The endeavor to predict and minimize radiation damage demands detailed fundamental knowledge about the properties of lattice defects and their clusters. From birth in cascade events, to migration and interaction with one another, to absorption at sinks, only a comprehensive understanding of defect behavior can truly illuminate the causes of, and solutions to, radiation damage. This is crucially important to a confident assessment of material properties for a number of reasons.

Due to the limitations and expense of neutron irradiations, the experimental database of irradiation effects information often deviates from the application conditions for real reactors. Problems revolving around sample activation and the length of time required render neutron irradiation trials difficult, and a great deal of information is taken from faster, safer, cheaper heavy ion or electron irradiation trials instead. Neutron irradiations themselves, as performed in test reactors, often have uncertain or variable temperature histories. Assessing how temperature, dose rate, damage conditions impact damage formation allow this data to be mapped back to operating conditions, and serves as one example of why fundamental defect behavior is important.

Thus, analyzing the formation of microstructual features during irradiation is useful not just on its own merits but for insight into fundamental defect behavior as well. This dissertation focuses on the formation of select damage microstructures in ferritic/martensitic iron-chrome based alloys, one strong candidate material for applications in both fast fission and fusion reactors. The objective is to provide defect transport based mechanisms for the formation of these microsturctures consistent with the body of existing knowledge about the properties of point defects and their clusters in iron. No such quantitative model for the formation of low temperature damage structures exists for these materials at the present time. In essence, this research aims to reproduce the damage evolution seen in experiments with a physical, rather than phenomenological or empirical, modeling basis.

Though it focuses heavily on a specific set of materials and experiments, the scope of this type of research is not limited to a mere analysis of the damage seen there. Because mesoscale kinetic models are based on fundamental properties of defects and their clusters, they can begin to develop predictive capabilities. In this capacity, such models can illuminate the complex network of processes that give rise to damage. Defect interaction properties are central to these kinetic effects, and therefore the information developed through these models is fundamental to the further understanding of a wide array of irradiation effects. While a great deal of research has been done on the structure and energetics of defect clusters, less attention has been paid to the implications for their interactions with one another, which is fundamental to damage formation. Insights into the defect properties as applied to this problem can be useful for other ferritic alloys or operating conditions that have not yet been fully studied, and may even prove relevant to other metals to the extent that the defects in them behave similarly.

Chapter 2

Background

This section aims to outline the most pertinent information about the material studied in this work and the techniques used to study it. An overview of the class of steels this research specifically targeted for analysis serves as a starting point. A discussion of the experimental techniques that provide information on the microstuctural evolution our models are designed to quantify follows. The discussion concludes with an overview of the history of kinetic modeling based on reaction rate theory and its importance in the field of radiation damage.

2.1 Ferritic/Martensitic Steels

Ferritic/Martensitic steels are a promising material for a variety of applications in fusion and next generation fission reactors[2–5]. Originally developed for commercial fossil fuel plants, these alloys boast a long history of operating and fabrication experience that provides an edge over more exotic candidate materials. The composition of most early F/M variants included roughly 9 to 12% Cr and 1% Mo, with some examination of higher and lower Cr content. Alloys developed more recently focus on various replacements for Mo to reduce radioactivity after exposure to the 14 MeV neutron spectrum typical for fusion environments. The resultant alloys, reduced activation ferritic/martensitic steels, have remained a leading candidate for the structural components of fusion reactors. In the fission context, F/M steels have a plethora of potential applications in several next generation (gen-IV) reactor designs. These reactors introduce a number of new design challenges not addressed in the current fleet of LWRs, as gen-IV designs involve higher operating temperatures and subject reactor components to higher neutron fluences than LWRs. For these reactors, F/M steels are a leading candidate for a number of internal and external components.

Strong resistance to irradiation induced void selling is perhaps the most attractive feature of these materials[6, 7]. As the neutron fluence increases, swelling places an upper limit on the service lifetime of a number of potential alloys, particularly austenitic stainless steels where steady state swelling often occurs at a rate of nearly 1% per dpa, severely restricting the neutron dose these alloys can absorb safely. F/M steels and simpler ferritic alloys demonstrate significantly less swelling over the dose increments achieved, as many as 200 dpa. It remains unclear to what extent this resistance can be attributed to a reduced rate of steady state swelling as opposed to merely a longer incubation period before swelling begins, although both are argued to contribute. There is little in the way of consensus as to what might cause such long transient regimes, and whether the swelling resistance they provide will extend to yet untested combinations of temperature and flux.

Radiation induced hardening and embrittlement dominate at lower temperatures, up to roughly $420^{o}C$[5, 8–10]. As with other body centered cubic (bcc) metals, ferritic steels fail by brittle fracture at sufficiently low temperatures. No similar change in failure mode occurs in austenitic steels. This phenomenon complicates the use of ferritic steels in irradiation environments because the ductile to brittle transition temperature - as measured in Charpy v-notch impact tests - can rise $100^{o}C$ or more. These shift are accompanied by dramatic increases in the yeild strength, and occur following only a few milli-dpa of neutron irradiation. In this regard, F/M steels exhibit similar operational challenges as the low-alloy steels which comprise currently operating LWR reactor pressure vessels. Much of the embrittlement evident in RPVs, however, stems from the development of copper rich precipitates formed through radiation enhanced diffusion. The hardening exhibited by other ferritic alloys lacks so simple an explanation, instead arising from a complex blend of irradiation induced precipitates and defect structures.

Transmission Electron Microscopy (TEM) is an indispensable technique in the characterization of the microstructural features responsible for large scale material property changes. Defect structures in the material produce local changes in the diffraction conditions, which alter the intensity of an electron beam transmitted through the material. Defect complexes as small as a few nm in size can be visualized in this manner. Following visualization, the mean size and density of any defect structures that appear can be determined through simple counting processes. Which defect structures might be causing these diffraction aberrations is often more difficult to asses by TEM alone. Some defects provide characteristic identifying features, such as the different appearance of voids in over and under focused conditions, but many structures do not. In these cases, combination with other techniques, subsequent annealing, or further irradiation can prove helpful.

The microstructure that develops in the hardening regime for F/M steels is known as “black dot damage”, so named for its appearance in bright-field TEM micrographs[11–17]. The dots themselves are typically small, on the order of 1 to 5 nm. The defect structures responsible are typically assumed to be small prismatic dislocation loops formed through the aggregation of a few dozen to a few hundred point defects, although it may be difficult to determine conclusively. When aligned on a single plane, these defects collapse into either a platelet of extra atoms in the case of interstitials or missing atoms in the case of vacancies. As such, dislocation loops can have either vacancy or interstitial character. These loops can grow or shrink by absorbing migrating vacancy or interstitial defects. When a dislocation loop grows sufficiently large in diameter, the contrast generated by the line segments can be resolved separately and the defect image resembles a loop rather than a dot. For sufficiently large loops, the character can be assessed via the “inside-outside” contrast technique, but black dot damage is typically too small to apply this technique rigorously. Hence, for loops on the scale of black dot damage the interstitial vs vacancy character is often unavailable from microscopy alone.

This microstructure is by no means unique to ferritic alloys. Hardening and black dot damage both feature prominently in radiation response at low temperatures across metals. The formation of black dots in iron, however, occurs at later doses and at a different rate than in most other metals. In many materials, the loops are typically assumed to form through the agglomeration of vacancies born in a single cascade on very short timescales. These cascade collapse events are unlikely in iron, evidenced by the long incubation time before loops appear[18, 19]. Rather, the formation of black dots in iron requires some interaction between defects produced in different cascades, either by diffusion of defects between cascades or spatial overlap of a cascade event with previously existing defect structures. Additionally, the defects that form in iron are often discovered to be interstitial rather than vacancy in nature at sizes large enough to determine directly and in post irradiation annealing studies[15, 20, 21].

Black dot microstructures dominate ferritic alloys following irradiation at temperatures up to around 300^oC to 400^oC, depending on the steel being considered. Irradiation data is spread across a number of commercial and model alloys with roughly 9% Cr and higher purity iron, which retains the bcc lattice structure. At higher temperatures, the microstructure becomes populated by a lower density of larger loops. The size of the loops increases steadily with temperature as the number density drops such that by temperatures near 500^oC a typical loop diameter is on the order of a few hundred nm[14, 17]. In this higher temperature regime the loops are clearly identified as interstitial in nature.

In addition to vacancy or interstitial character, TEM is capable of revealing the Burgers vector of dislocation loops. It has long been known that ferritic alloys can develop loops with either $a\left<100\right>$ or $\frac{a}{2}\left<111\right>$ Burgers vectors[22]. Which loops form and which do not is a complex function of temperature and composition. In high purity iron below temperatures of around 200 to 300^oC, loops are found preferentially in $\left<111\right>$ orientations, although occasionally $\left<100\right>$ loops are observed as well and at these temperatures the defects are small and orientation is difficult to asses. At temperatures above 500^oC this preference is reversed, with a transition in the intermediate regime[23]. Adding Cr to the matrix does not alter this scenario much and trends in defect properties are similar, though loops are typically smaller in size and higher in number density at all temperatures.

Black dot damage develops as early as a few tenths of a dpa, a timescale much shorter than the required in-reactor service lifetime anticipated for these materials. At higher temperatures where black dots grow into resolvable loops, the individual features expand into each other and the loops form a network of interconnected dislocations segments, also at doses lower than the service lifetime. Consequently, it is possible to observe the microstructure that develops following neutron by irradiating specimens in test reactors, then preparing samples for microscopy. Though this technique is often employed, the irradiation times required are still quite long and the specimens become radioactive in the process. To avoid these inconveniences, many studies on the formation of early dose microstructures have been performed using ion irradiation.

The advantages of ion irradiations extend beyond shorter irradiation times, lower costs, and lower activation. Ion and electron irradiations can be performed in concert with microscopy, rather than merely viewing the irradiation microstrucuture after the fact. Such *in situ* TEM studies provide a number of advantages over traditional characterization techniques. With an *in situ* experiment, the same region of foil can be tracked through long dose increments, pausing for further characterization and more detailed analysis as necessary. In post-irradiation analysis, a series of samples are irradiated to pre-planned doses, and consequently the local conditions for each dose level are different. Another key motivation for *in situ* irradiation trials is the ability to observe dynamic behavior, tracing the size and position of individual damage features as they appear, develop, migrate, interact, or vanish.

The IVEM-tandem facility at Argonne national lab has the unique capability to perform *in situ* irradiation experiments with heavy ions as a damage source[24]. A number of ferritic and ferritic/martensitic commercial and model alloys have been examined in this facility in recent years. These include a series of model alloys ranging from high purity iron to more complex alloys including up to 12% Cr and as much as 0.1% carbon have been irradiated to doses as high as 10 dpa[12, 15, 16]. Additionally, samples of the commercial alloys NF616 and HCM12A have been irradiated to roughly the same level[13]. In all cases, a number of irradiation temperatures have been examined, and the microstructural features have been examined both in still frames for counting and sizing information and dynamically to investigate kinetic behaviors.

We will focus on the observations in Fe-9Cr-0.1C and Fe-12Cr-0.1C model alloys in order to illustrate the trends in defect behavior seen in ferritic alloys at this dose level. Trends in observed defect density and size, illustrated in figure 2.1, have been collected at a wide range of irradiation temperatures. Clear saturation of defect density occurs at early doses, below 1 dpa, at all temperatures. The defect size continues to grow well past the doses where density saturates. The magnitude of defect density at saturation varies only slightly with temperature, certainly less than an order of magnitude, in the range of studies for this material. At high temperatures there appears to be some prompt growth leading to larger defect sizes upon first observation. The subsequent growth rates, however, are not clearly distinguishable.

The results of these studies should be examined with some degree of care, as the process of counting defects on a micrograph contains a number of inherent sources of error. It is not always clear which features are irradiation induced defect structures and which are not. With *in situ* irradiations this is less of a concern, as the same region of the material is continuously imaged, whereas in a conventional post-irradiation study any detailed knowledge of the pre-irradiated local microstructure is absent. Regardless, some human judgment is required in separating artifacts from data. The basis of this judgment is arguably quite sound when features are large - particularly in the *in situ* experiments - but becomes increasingly dubious when the features are near the smallest observable sizes. Furthermore, micrographs are in essence two dimensional projections of a three dimensional structure, and changes in thickness between samples will alter the observed areal density.

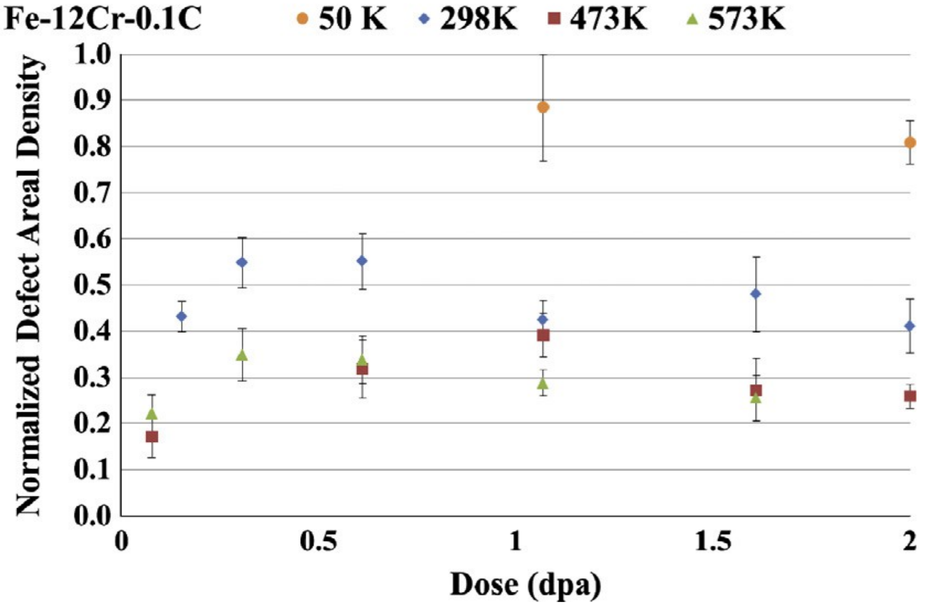

(a) Normalized areal defect density

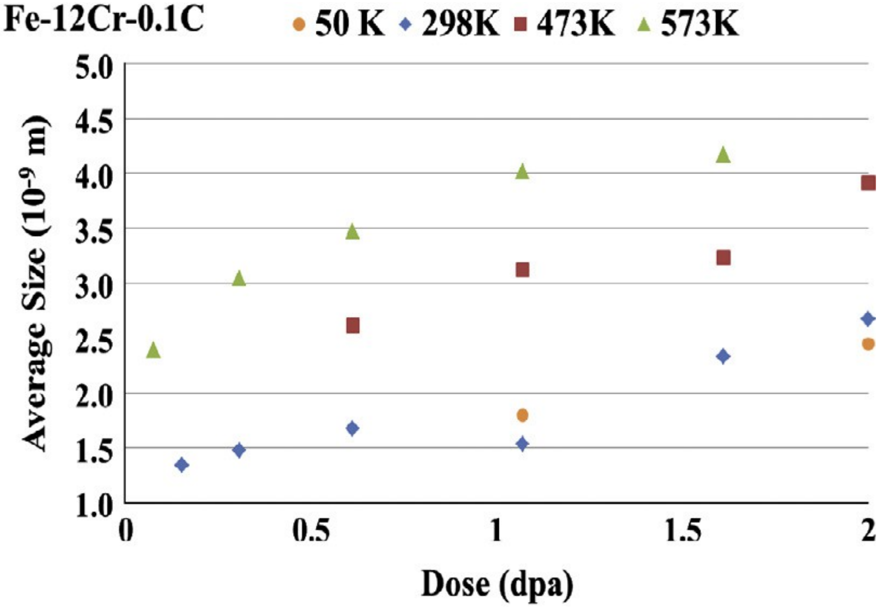

(b) Mean visible defect diameter

Figure 2.1: *In situ* trends in damage microstructure evolution in an Fe-12Cr-0.1C F/M model alloy as reported in [12] showing an early saturation in defect density and continuous growth in size across a wide temperature range.

There is some difficulty assessing defect size as well. The image size generated by a defect structure varies based on its orientation relative to the electron beam and its depth. For this reason, the image size of any individual defect is only reliable within a few nanometers. Though the mean sizes are not likely to be impacted greatly, this effect might cause some spread in the size distribution. In the regime of black dot damage, however, many of the defects are near the visibility threshold. Variability in the image size of these barely visible defects can render them undetectable, altering the visible density and the mean size as well.

The difficulty associated with counting features on a micrograph discourages strong statements about the actual defect population on this basis, particularly with regard to the defect density. Between the numerous invisibility citerion, both by size and orientation, and the human judgments requisite in the counting process, reported densities based on micrograph counting surely differ from reality by some detection efficiency. That efficiency is nominally systematic, however, such that changes observed in defect densities correspond to changes in the real defect content. Consequently, TEM data can inform the effects that irradiation temperature or continuing dose has on the true microstructure.

Such trends can still be misleading when the feature size is near the visibility threshold. For example, the commercial alloys exhibit a somewhat different apparent saturation behavior reaching maximum density at significantly later doses than the model alloy of Figure 2.1. The mean size of the defects in that case remains almost constant, near the visibility threshold. Consequently, it is impossible to determine whether this apparent difference in saturation behavior is in fact real. One might posit that defects are generated more slowly and do not grow. It could as easily be the case that growth is merely slower and obscured by the visibility threshold, promoting defects to visible size more slowly, and the size trends are unreliable due to a large number of sub-visible defects remaining uncounted at most doses. Clearly, some care must be taken in choosing which trends to analyze, and considering the effect of visibility criteria on the defect density.

The detailed information provided by *in situ* observations present an excellent opportunity to develop and fine tune theoretical frameworks to model the formation of damage microstructures. Dynamic information about defect behavior allows some direct insights into the kinetics of damage development. Such modeling endeavors can serve to provide some additional information about the fundamental properties of point defects and defect clusters, assess the legitimacy of proposed mechanisms for damage formation, and provide quantitative reinforcement for qualitative descriptions of microstructure evolution that explain observed phenomenon in terms of fundamental defect behaviors.

2.2 Mean Field Rate Theory

The problem of irradiation induced microstructural changes spans multiple scales in time and space. On the one hand, defects are generated in short lived recoil events, which last only tens to hundreds of picoseconds and produce isolated defect structures spanning distances of nanometers or less. These problems are often well understood with atomistic or ab initio methods based on well developed fundamental physics. Engineering constraints on the other hand, deal with widespread physical and mechanical property changes that develop over the course of months, years, or even decades. These effects are understood under specific conditions with empirical models rooted in prior operating experience.

In between the engineering scale and the nanoscale regimes, microstructural changes are initiated through complex nucleation, growth, and coarsening processes driven by the migration of defects to sinks and one another. Historically, one of the most widely used tools to study these mesoscale phenomenon has been the mean field rate theory (MFRT). In its earlier form, this model imagined an ensemble average of point defects diffusing to a set of pre-existing sinks, and inferred changes in the microstructure from the differences in defect arrival rates at the sinks. For example, where the flux of vacancies into voids is greater than the flux of interstitials, voids grow.

A number of independent versions of MFRT appeared beginning in the 1970s, all based on the same fundamental mechanics[25–29]. The populations of interstitials and vacancies are defined by a pair of PDEs of the form

$$\frac{dC_i}{dt} = -\sum_n D_i S_{i,n} C_i - k_{i,v} C_i C_v + g_i \tag{2.1}$$

$$\frac{dC_v}{dt} = -\sum_n D_v S_{v,n} C_v - k_{i,v} C_i C_v + g_v \tag{2.2}$$

where $S_{i,n}$ and $S_{v,n}$, the sink strengths for absorbing interstitials and vacancies respectively at a given sink n, can change over time as the sinks evolve. For example, the change in the number of vacancies comprising voids can be deduced simply from

$$\frac{dn_V}{dt} = D_v S_{v,V} C_v - D_i S_{i,V} C_i \tag{2.3}$$

and the appropriate changes in size and sink strength can be deduced from there. In principle, the defect production rates g are equivalent and the diffusivity D for each defect at a given temperature are known and constant. Consequently, the resultant equations can be integrated simply, often analytically. In their early forms, these models aimed to describe steady state void swelling.

The microstructural changes predicted by MFRT hinge on the calculation of these sink strengths. If the strength of every sink in the system is equivalent for vacancies and interstitials, then the flux of point defects to each sink is equivalent and no long term evolution of the sinks can occur. It is the sinks for which these strengths are dissimilar, the so-called "biased" sinks, which drive the formation of extended damage features. In models of void swelling only voids and dislocations were considered. The dislocations have a long range interactions with interstitial defects but not vacancies, leading to a dislocation bias in favor of interstitials. This in turn leaves an excess vacancy flux to the voids, driving swelling. It is in the calculation of sink strengths that the early rate theory models diverge.

All approaches to calculating the sink strength begin from a demand that the flux into a sink locally be equal to the rate of absorption of sinks globally. A local sink establishes some local concentration profile for diffusers $n_\alpha(r)$, where the bulk concentration from the rate equation is the mean value of n_α. Integrating the inward flux at the sink surface reveals the inward current I_α of diffusers, which is tied to the sink strength according to

$$D_\alpha S_{\alpha,\beta} C_\alpha = I_{\alpha,\beta} C_\beta = C_\beta \oint_S D_i \frac{dn_\alpha(r)}{dr} \tag{2.4}$$

for a diffuser α and sink β. A complete solution requires an estimate of the concentration profile about the sink, and this is the point of contention amongst various applications of the model.

The most common model simply assumes that the profile followed a quasi steady state solution to the diffusion equation,

$$0 = D_\alpha \nabla^2 n_\alpha \tag{2.5}$$

and solved in the appropriate geometry within an primitive cell containing that sink - and no others - to provide the flux. This relatively simple approach has been applied in a number of forms by different researchers and commonly appears in textbooks[28–30]. Despite some differences, a fairly standard set of sink strengths were developed which will be outlined in more detail in subsequent chapters.

The primitive cell model as applied came under scrutiny from Brailsford and Bullough who pointed out a number of internal inconsistencies and potential problems[25–27]. The list of contentions includes: the implicit regular arrangement of sinks, the non-vanishing flux at primitive cell boundaries in most formulations, the failure to include defect generation, and the inability to include multiple sink types consistently. In place of this approach, they advocated a model based on a lossy Poisson equation

$$0 = D_\alpha \nabla^2 n_\alpha - k_\alpha^2 n_\alpha + g_\alpha \tag{2.6}$$

solved not over a single primitive cell but rather over a much larger supercell. In this approach the action of the other sinks, including those of the same type as the one generating the profile, are accounted for as an “effective medium” with a net sink strength of k^2. In this sense, n(r) becomes the ensemble average of α about the type of sink in question, and the effective medium arises from the ensemble average of the action of other sinks. Though more rigorous, the solutions to this method are more complex and the sink strengths become coupled, often introducing a dependence on the square root of the net sink strength. The difficulty of solving the resulting equations was sufficient to discourage the inclusion of recombination terms in effective medium based models.

Though the implementation details vary the underlying idea is the same, and references to reaction rate theory or classical rate theory (CRT) could be appealing to either. What these models lack in detail they make up for in utility. The basic physics that these models formalize, the partitioning of defects to different sinks, lies at the center of understanding most irradiation effects. These models have been used as a framework for understanding loop growth, segregation, creep, and dimensional changes among other effects, but were most prolifically applied to steady state swelling.

A number of aspects of void swelling behavior can be understood quite simply in light of reaction rate theory, particularly microstructural and temperature effects. The nature of the CRT explanation for void swelling, a partition of defects between biased and unbiased sinks, requires a blend of sink types in order for swelling to persist. If only one sink type is present, it absorbs all defects of both type, resulting in no net microstructural changes even if the sink is biased. Accordingly, CRT predicts that swelling should be most rapid when the ratio between the dislocation and void sink strengths is nearly unity. This basic trend is indeed observed in many systems [31].

Another key success of these early models was in understanding the temperature dependence of void swelling. At high temperatures, cavities emit vacancies thermally, providing an upper bound on the swelling regime. At sufficiently low temperatures, the mobility of defects shrinks, leading to higher steady state concentrations and thereby greater intrinsic recombination. At sufficiently low temperatures, the defect elimination becomes dominated by recombination rather than loss at sinks. Peak swelling occurs in the intermediate interval, though the precise temperature depends on the rate of defect production. Higher rates of production demand greater diffusivity to prevent defect populations from building to levels where recombination dominates. Rate theory cleanly encapsulates this physics, leading to the development of "temperature shift" laws which correlate the peak swelling temperature to dose rate[32, 33].

For identifying and rationalizing these trends, CRT has proved invaluable. Its predictive power and physical fidelity are more questionable. Though CRT based on the dislocation bias approach can perform well with reasonable fitting parameters for modeling steady state void swelling[34], it does so only under particular conditions. The prompt swelling seen at early doses even in materials with low dislocation densities, for example, cannot be accounted for by CRT directly. Additionally, the differences in damage accumulation behavior between metals cannot be explained merely in terms of the dislocation bias. To explain these phenomenon, reaction rate theory requires heavy modifications.

A successor set of models based on the concept of "production bias" arose to attempt to resolve a number of discrepancies inherent in CRT[35–40]. The motivations for the new approach were numerous, though primarily based on observations of cascade structure enabled by atomistic computational techniques which promote a drastically altered picture of defect migration and interaction with sinks. A chief tenet of this model is a low efficiency of defect production in cascade events such that the number of Frenkel pairs produced is significantly fewer than anticipated due to inter-cascade recombination. The damage which does survive is often introduced in the form of clusters, rather than solely as isolated monomers.

The differing properties of the defect clusters generated as primary damage compete with the monomer bias of dislocations to drive microstructural changes in the production bias paradigm. As clusters behave differently than isolated point defects, the damage produced as clusters becomes partitioned to sinks differently than the monomer species, hence the moniker of production bias. Some defect clusters are presumed to be immobile in the production bias framework. These clusters, generally of vacancy type, must be eliminated through either recombination with mobile defects or absorption at mobile sinks. Other clusters are mobile, but only along a fixed glide direction. Within the context of a production bias model, the restricted dimensionality of cluster motion changes the sink strengths for absorbing one dimensional diffusers.

Determining the proportions at which these different classes of defects are produced in cascades is required in the production bias framework to determine microstructural evolution. Prompt swelling becomes a trivial consequence of a growing density of immobile vacancy clusters until they reach a steady state against annihilation with mobile interstitials. Furthermore, different lattice structures generate different cluster populations during cascades, casting light on microstructural differences between them that CRT cannot explain. The fcc metals for example, tend to generate large clusters directly in cascades with many vacancies clustered into single Frank loops or stacking fault tetrahedra. The bcc metals generate smaller clusters and more point defects, facilitating recombination and hindering the nucleation of large features.

The production bias model represents significant progress over classical rate theory in modeling the evolution damage from a physical basis. Though some may argue that classical rate theory is sufficient to explain many radiation damage phenomenon, it has a substantially weaker physical basis as its characterization of primary damage is inherently flawed. This error may prove inconsequential in certain dose and temperature regimes, but will not in others. The advantage of the production bias model lies in its applicability outside such regions, where many important problems in radiation damage lie. The transient regime of void swelling is one important example, black dot damage is another.

Further progress in radiation effects modeling requires an approach that treats the behavior of cascade induced defect with an even greater degree of fidelity. Despite the improvements of this approach, it still handles defect structures in a coarse grained manner. Typically, primary damage is divided into monomers and clusters, suppressing the true damage spectrum and ignoring the differences between clusters of different sizes. To apply deterministic kinetic models to the black dot damage problem, we intend to turn to more sophisticated methods, which retain the rate based framework, while allowing a more detailed representation of clusters both within and beyond the primary damage size range.

Chapter 3

Methods

Attempts to model the formation of extended microstructural features produced by irradiation must account for processes that occur on timescales separated by many orders of magnitude. The point defects and small clusters which are ultimately responsible for observable changes in the material are born in events lasting no longer than a few picoseconds but their recombination, self-clustering, or absorption at sinks may require microseconds, milliseconds, or longer to fully resolve. Obtaining a series of damage events lengthy enough to produce observable damage requires an incubation period of a few minutes for laboratory conditions (such as heavy ion irradiations), or even many years in the case of neturon flux environments present in the current generation of commercial reactors. Extending methods that satisfactorily represent the physics of short timescale processes to model the longer scales is prohibitively expensive. Conversely, attempting to ignore the rapid processes and use less expensive methods can be highly inaccurate.

A common resolution to the dilemma posed by the multitude of time and length scales inherent in irradiation damage problems is to analyze each scale with a separate method, with some degree of communication between them. Generally speaking, the information from small scale methods informs a suitable application of coarser methods. For ion irradiations, molecular dynamics (MD) portrays events that occur on picosecond to nanosecond intervals such as displacement cascades. Cluster dynamics (CD) then governs the longer term aggregation of the cascade remnants into extensive damage features, with Monte Carlo methods bridging any gap between the two.

3.1 Cluster Dynamics

The bulk of this work focuses on the aggregation, annihilation, and absorption of point defects as the driving force for long term development of irradiation induced damage. In order to reach doses of interest, the methods used for this purpose cannot contain any atomic level resolution but still needs to accurately represent the physics of the driving kinetic processes. The CRT approaches discussed in Chapter 2 are the simplest model designed for such a task.

Due to the now well known shortcomings of CRT as traditionally applied, a broader method is needed. A more comprehensive model could explicitly include the last two decades of information regarding the mobility and configuration of point defect clusters. A more robust model could also account for cascade damage sources. A better posed model could handle spatial variations in defect sources or sinks. The CD method allows all of these extensions.

CD models retain the basic principles of rate theory, namely deterministic calculations of point defect densities based on rates of reaction, and generalizes them to point defect clusters of arbitrary size. In addition to expanding the number of defect species included, the density of each is allowed to vary spatially. This involves a series of partial differential equations of the form

$$\frac{\partial C_i(x,t)}{\partial t} = D_i \frac{\partial^2 C_i(x,t)}{\partial x^2} - D_i S_i(x) C_i(x,t) + g_i(x,t) - L_i(\mathbf{C}(x,t)) + G_i(\mathbf{C}(x,t)) \tag{3.1}$$

each of which represents the diffusion, loss at sinks, production as primary damage, and interaction of a single cluster population. Each possible defect cluster is given a unique equation $C_i(x,t)$, in contrast to rate theory where only mono-vacancies and mono-interstitials are usually included. Each of these concentrations can be considered part of an abstract defect density vector or size distribution function $\mathbf{C}(x,t)$. Taken together, this coupled set of equations is referred to as the master equation.

Many of these equations represent clusters large enough to be observed as microstructural features. The density and mean size of observable damage features as a function of time can be explicitly characterized, given a sufficient number of equations. In practice many thousands of members of $\mathbf{C}$ may be required and these equations are all coupled through the last two terms in Eq. (3.1), rendering the full system impossible to solve analytically. In this sense, CD is an exercise in numerical integration which operates by time marching a large system of coupled equations through the desired damage interval.

Models of this form began appearing to examine nuclear materials in the late 90s. Early applications aimed to explain phenomenon such as copper precipitation in iron[41]. Adaptations designed to examine the aggregation of point defects into visible damage under electron irradiation emerged a few years later[42, 43]. Those models have been extended to examine other phenomenon, such as gas retention[44, 45] and isochronal annealing[46]. Over the past decade such models have become indispensable tools for describing dislocation loop formation and growth at both visible and subvisible levels[47–49], which is precisely the phenomenon under investigation here. CD appears to be a logical mode of analysis, so it is worth examining its core components, their derivations, and the extent to which they are applicable.

3.1.1 Reaction

The formation process for visible damage involves a long series of aggregation events of smaller clusters, which are represented in the reaction terms of Eq. (3.1). The possible interactions of defect clusters can be broken down into two types:, the annihilation reaction

$(A + B \to 0)$ and the aggregation reaction $(A + B \to C)$. The rate at which a particular reaction progresses is written in terms of its reaction rate constant, k^+, such that

$$R^+_{i,j} = k^+_{i,j} C_i C_j \tag{3.2}$$

where i and j are the reacting species. The loss term $L_i(\mathbf{C}(x,t))$ includes the rate of depletion of reactants while the production term $G_i(\mathbf{C}(x,t))$ includes the generation of reaction products. To determine the net rate of loss for a particular species, one sums over all the possible reaction in which that species is depleted[1]

$$L^+_i = \sum_j R^+_{i,j} \tag{3.3}$$

where j spans all other species in the system. Similarly, summing over all reactions that produce that species gives its production rate

$$G^+_i = \sum_{n+m\to i} R^+_{n,m} \tag{3.4}$$

where n and m span all possibilities of interacting pairs that result in the formation of i. L_i and G_i are not completely specified by L^+_i and G^+_i as additional contributions are made by other mechanisms.

In effect, the reaction rate constants specify which aggregations are preferred. Consequently, correctly determining k^+ is of prime importance in the success of a CD model. The diffusion limited flux of defects to sinks as employed in CRT models is easily generalized for this purposed. As an example, consider the typical case of two reacting species both of which are spherically symmetric and one of which diffuses isotropically. Using a primitive cell type approach, the concentration profile of the isotropic diffuser drops to zero at some fixed distance $r_{i,j}$ where the two species react spontaneously and elsewhere is governed by the Laplace equation

$$0 = D_i \nabla^2 n_i(r) \qquad \text{s.t. } n_i(r_{i,j}) = 0 \tag{3.5}$$

where n_i is used for concentration to clarify that it is not the mean field concentration C_i used elsewhere. When making an additional assumption that the concentration profile recovers to the mean field value far from the reaction radius the solution to the equation takes the form

$$n_i(r) = C_i \left(1 - \frac{r_{i,j}}{r}\right). \tag{3.6}$$

Following the procedure of 2.4, integrating the flux of i at the reaction volume surface reveals the inward current

$$I_{i,j} = \oint_S D_i \frac{dn_i(r)}{dr}\bigg|_{r_{i,j}} = 4\pi r_{i,j} D_i C_i \tag{3.7}$$

---

[1] When using this approach, some care must be taken in the special case where the two reacting species are identical $(A + A \to C)$. Although this does not influence the production rate, this reaction must be counted twice in order to determine the contribution it makes to the loss of the reacting species. In the implementation of CD suggested in appendix A this concern is taken into account in a natural and uncomplicated manner.

which is related to the reaction rate constant

$$k_{i,j} = \frac{R^+_{i,j}}{C_i C_j} = \frac{I}{C_i} = 4\pi r_{i,j} D_i \tag{3.8}$$

which is simply dependent on reaction radius and the species diffusivity. Where both species diffuse isotropically the reaction rate constant becomes

$$k_{i,j} = 4\pi r_{i,j}(D_i + D_j) \tag{3.9}$$

which could be viewed as a linear superposition of rates calculated for each species as the sole diffuser. This widely used rate constant for diffusion controlled processes, sometimes called the Smoluchowski rate, has been employed in a variety of contexts for over a century and is embedded in many MFRT and CD models. The assumption of sprerical symmetry and isotropic diffusion are not necessarily sound for BCC metals, and the relaxation of these assumptions will be discussed later.

It is worth noting that the reaction rates are essentially determined by the size and diffusivity of the reacting clusters. For this reason, correctly representing the diffusivity of the constituent clusters is of paramount importance. Diffusion generally obeys the Arrhenius relationship

$$D_i = D_{0,i} \exp \frac{-E_{m,i}}{k_b T} \tag{3.10}$$

where the migration energy $E_{m,i}$ represents the activation barrier for the transition of a cluster from one site to another. The pre-exponential factor $D_{0,i}$ contains information about the jump distance and jump frequency for a given cluster

$$D_{0,i} = \nu_{i,0} \frac{\lambda^2_{0,i}}{2N} \tag{3.11}$$

where N in this case is the number of dimensions in which the cluster can jump, and $\lambda_{0,i}$ is the jump distance. The attempt frequency, $\nu_{0,i}$, is equivalent to the phonon frequency for single defects but becomes more complicated for other species. In addition to influencing the reaction rates, the diffusion coefficient will contribute to the loss of clusters at distributed sinks and surfaces, spatial transport, and dissociation.

3.1.2 Dissociation

At some temperatures clusters can shrink in size by the thermal emission of monomers. This process, often referred to as evaporation, is crucial to understanding phenomenon such as void nucleation. It is not expected that this mechanism will affect the observable defects for temperatures considered in this work, but it may influence the populations of small clusters which are more weakly bound. The possibility of thermal emission is represented in CD in terms of dissociation reactions which follow the general form $A \rightarrow B + C$, where

C is some monomer species. The rate of this process is governed by the dissociation rate constant, k_i^- according to

$$R_i^- = k_i^- C_i. \tag{3.12}$$

The contributions to the defect loss and production rates due to dissociation are far simpler than those due to reaction. Each dissociation eliminates only one species and produces one species and a monomer. For the dissociation of a cluster i,

$$L_i^- = R_i^- \tag{3.13}$$

$$G_i^- = R_{i+m}^- \tag{3.14}$$

where m is the monomer produced in the emission process[2], and for that monomer

$$\mathcal{G}_m^- = \sum_{i \to i-m\ +\ m} R_i^-. \tag{3.15}$$

The rate constant associated with dissociation, k_i^-, is essentially determined by how strongly the monomers are bound into a cluster. The process of monomer emission could be imagined as a monomer attempting to climb an energy landscape to escape to the bulk, usually failing, but occasionally succeeding. It might seem tempting to tackle this problem in much the same way as diffusion, with some Arrhenius modification to an attempt frequency, only in this case for emission rather than making a lattice jump. A number of problems arise, however, when approaching the problem this way. The principle difficulty relates to mean field assumptions employed elsewhere in the model. An escaped monomer is strongly spatially correlated with the cluster that emitted it resulting in a higher rate of recapture than a mean field monomer. As an additional complication, there may be many monomers capable of dissociating from a given cluster and identifying them may not be trivial.

To avoid confronting the problem of emission kinetics in a mean field model, the dissociation constants are typically computed thermodynamically. Notice that each dissociation has a balancing reaction pair, such that for the dissociation process $A \to B + C$ there is a reaction process $B + C \to A$. The equilibrium condition for this process can be written as

$$\exp \frac{G_{b,A}}{k_b T} = \frac{x_A}{x_B x_C} = \frac{n_A}{\Omega n_B n_C} \tag{3.16}$$

where $G_{b,A}$ is the increase in free energy associated with transitioning from the monomer bound as a member of cluster A to unbound and separate from the smaller cluster B. This change is assumed to be dominated by the binding energy, $E_{b,A}$. At equilibrium the reaction and dissociation rates should be equal and setting $R_A^- = R_{B,C}^+$ can be expressed in terms of the rate constants for each reaction

$$k_A^- n_A = k_{B,C}^+ n_B n_C. \tag{3.17}$$

---

[2] Another special case arises here in the situation $A \to C + C$ (equivalently, $i - m = m$) where one should be cautious to avoid miscounting the contribution to the monomer species from this dissociation. Although complicated to represent in this notation it is handled naturally in the implementation discussed in appendix A.

Isolating the dissociation rate constant and solving in conjunction with Eq. (3.16) produces the expression

$$k_A^- = \frac{k_{B,C}^+}{\Omega} \exp \frac{-E_{b,A}}{k_b T} \tag{3.18}$$

which is independent of the equilibrium concentrations and applicable regardless of the system state.

3.1.3 Sinks

Any distributed microstructural features that absorb or annihilate defects or their clusters are referred to as sinks. Some examples of prominent sinks that have historically appeared in rate theory based calculations include network dislocations, grain boundaries, and voids. In CD any voids are subsumed into the cluster distribution as vacancy clusters and should not be included in the sink terms. Grain boundaries can, in principle, be implemented by imposing the proper boundary conditions. This work concerns itself primarily with thin foil irradiations, where the thickness of the foil is presumably significantly smaller than the size of a typical ferritic grain, rendering the implementation of grain boundaries unnecessary. The network dislocations, on the other hand, are not implicit in the other terms, and are the only contribution to the sinking rates in CD.

The rate of loss of defects at distributed sinks is formulated in terms of the sink strength. Although it is often denoted as k_i^2 in the literature, S_i will be used here to avoid confusion with the reaction rate coefficient k^+ and dissociation rate coefficient k^-. Dislocation sink strengths can be computed using the same method as Eq. (3.5), simply replacing the spherical coordinate system with a cylindrical one. Solving the resulting problem gives a defect current into the dislocation core of the form

$$I_{in} = \frac{2\pi D_i C_i}{\log r_c / R} \tag{3.19}$$

for some dislocation capture radius r_c, and separation distance R. The separation distance can be recast in terms of the dislocation density ρ by assuming each dislocation occupies a separate equivalent cylindrical cell such that $\pi R^2 = \rho^{-1}$. Applying this current to all system dislocations calculates the sink strength,

$$S_i = \frac{I_{in}\rho}{D_i C_i} = \frac{2\pi\rho}{\log\left(\pi\rho r_c^2\right)^{-1/2}} \tag{3.20}$$

where ρ is the dislocation density.

In some discussions of the dislocation sink strength it has been common to use a multiplication factor acting on the dislocation density, written as $S_i = Z_i\rho$. This description is a popular simplification of the diffusion limit for a number of reasons. For one, it simplifies the algebra in traditional rate theory where many expressions are solved analytically. Furthermore, for many microstructures and defects the factor Z is nearly unity and nearly

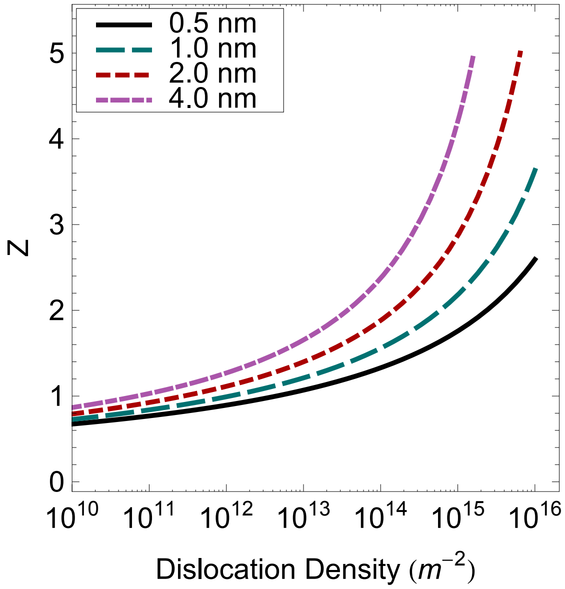

Figure 3.1: The sink strength multiplication factor for selected dislocation capture radii

independent of dislocation density up to a point, limiting any error introduced by the simplification. Finally, it allows for a straightforward presentation of dislocation bias $B = Z_I/Z_V$ (or $1 - Z_I/Z_V$, depending on convention) in applications where only Frenkel pairs are considered. Unfortunately, divergence from unity becomes relevant as ρ exceeds 10^{13}m^{-2} as noted in [50] and shown in Figure 3.1, well below the expected densities for many ferritic and martensitic microstructures. More fundamentally, when applying a CD model the radius of capture for the dislocation should be allowed to vary with cluster size which significantly impacts estimates of the sink strength.

3.2 Additional Methods

3.2.1 Object Kinetic Monte Carlo

In CD, physical properties such as radius, migration energy, binding energy, and dimensionality must be chosen for each cluster in the system, with the number of clusters stretching possibly into the thousands. From these parameters, the kinetics of interaction are calculated based on a series of mean field assumptions governing the rates of reaction as discussed previously. CD models fail to accurately portray a physical system under two conditions, if the parameters are unphysical or if the kinetic assumptions are violated. The case where clusters are spatially correlated is a prime example of the latter failure mode, and presents itself in some damage conditions. The appropriate approach for such failures retains the framework of parameterized point defect clusters which suppress atomic scale fluctuations, but sheds assumption laden reaction rates.

The method of choice for this scenario is kinetic Monte Carlo (KMC). Monte Carlo methods are a broad class of stochastic techniques which have long been employed in a variety of fields where deterministic equations are difficult to formulate or solve. These techniques take many forms, but they all involve selecting events from a probability distribution and deciding whether or not to execute them. In KMC, the probability for selecting an event is given by the frequency with which it occurs relative to the total frequency of events

$$P_i = \frac{\nu_i}{\sum_i \nu_i} \tag{3.21}$$

and the selected event is automatically executed. The time is incremented for each Monte Carlo step according to

$$\Delta t = \frac{\log \xi^{-1}}{\sum_i \nu_i} \tag{3.22}$$

where ξ is a random number uniformly distributed between 0 and 1. This procedure, typically referred to as the Residence Time Algorithm, was developed in a slightly different form to investigate vacancy diffusion in the 1960s[51] with the version in Eq. (3.22) emerging slightly later[52].

The kinetic Monte Carlo algorithms can be divided further into several different forms which vary based on how the catalog of possible events is chosen. Three popular techniques include the atomistic (AKMC), event (EKMC) and object (OKMC) variants. To briefly overview, atomistic approaches choose the event catalog by sampling the energy landscape of the current atomic configuration. In OKMC, defects are grouped into objects each of which is capable of participating in a limited number of preselected possible events. This method has a significant speed advantage at the cost of possibly neglecting unforeseen processes. Finally, EKMC further accelerates computations by altering the residence time algorithm to change the object population in each step. For this study OKMC is a fitting choice, as the events that form the predetermined catalog are supplied by the same parameters that inform a CD model, which establishes a certain coherence between the two. Some examples of events that might occur in the context of defect cluster evolution include discrete cluster jumps, a cluster emitting a monomer, or a cluster being produced in an irradiation event. In this paradigm, two clusters react not with a predetermined frequency, but rather when they happen to co-inhabit a reaction volume as the result of a jump.

The application for OKMC within the multiscale framework of a rigorous application of cluster dynamics involves aging the remnants of cascades to remove spatial correlation. At the conclusion of the thermal spike phase of a cascade event, a vacancy rich core is surrounded by a distribution of interstitials and crowdion bundles which are highly mobile. These interstitials may or may not react with the cascade induced vacancies, but the probability of reaction is much higher for these interstitials than for the concentration of interstitials found in the mean field. KMC methods and have been applied in the past to study this stage of damage evolution[53–55], and will be applied again here. Generally speaking, the main effect of spatial correlation in cascades is a local increase in the preference for recombination which reduces the number of point defects that are effectively created. It may also increase the size of primary damage clusters in cases where free point defects are highly likely to be absorbed at sinks and larger pre-existing clusters in the mean field.

3.2.2 Molecular Dynamics

In early phases of damage generation, defects cannot be identified as separate, unique objects with fixed characteristics and well defined properties. For the first several picoseconds of a cascade the energy barriers that prevent defect migration are overwhelmed by the magnitude of energy deposited by the PKA. The crystal lattice temporarily vanishes, the related notion of lattice defects becomes meaningless, and methods that rely on these concepts are inapplicable. In order to simulate these events, methods that directly calculate atomic interactions are required. There are a number of freely available, well-developed software packages capable of solving these systems. The LAMMPS[56] code is used for all MD simulations in this study.

MD progresses by integrating the Newtonian equations of motion

$$\ddot{\mathbf{r}}_i = \frac{\mathbf{F}_i}{m_i} \qquad \text{For } i = 1, \ldots, N \tag{3.23}$$

for an ensemble of N atoms whose starting positions and velocities are specified. The system of equations in specified by Eq. (3.23) amount to a system of second order differential equations which can be solved so long as the forces acting on each atom can be explicitly calculated. Time marching the system, therefore, requires employing the local gradient of the potential energy for each atom

$$F_i = -\nabla U_i \tag{3.24}$$

at every timestep. This gradient is computed from interatomic potentials.

Where OKMC and CD suppress atomic scale fluctuations by introducing parameters that govern cluster behavior, MD suppresses information about the electronic structure by introducing interatomic potentials. In principle, these are reasonably accurate representations of the potential energy an atom experiences at any given location arising from interactions with all of its neighbors. These potentials can be generated by “fitting” to a variety of data which may include the elastic constants, the formation energy of lattice defects, the binding energy of various structures, and almost any other criteria one could think of. In practice, a few of these may be fit very poorly due to the empirical nature of potentials and many competing potentials typically exist for a given interaction.

In radiation damage simulations, atoms become much more energetic than they would under normal circumstances and may make closer approaches than the potential is designed to handle. The related problems are avoided by using the Ziegler-Biersack-Littmark (ZBL) screened nuclear repulsion potential for very small atomic separations[60]. The potentials used for the MD simulations throughout are given in Table 3.1, stiffened with ZBL where appropriate.

Pair	Potential	
Fe-Fe	Ackland-Mendelev 2004	[57]
Fe-He	Juslin-Nordlund 2008	[58]
He-He	Janzen-Aziz 1997	[59]

Table 3.1: Choice of interatomic potentials

Due to the atomic scale resolution offered by MD approaches, it may be tempting to suggest that such methods be employed generally, doing away with the assumptions and simplifications introduced by OKMC and CD. Due to the computational expense of these methods, however, such an approach is not possible at the present (or likely any future) time. As each atom introduces a unique equation, the number of processors that would need to be employed to solve a representative volume for a macro-scale calculation is prohibitive. Additionally, the timestep limitation in an MD simulation is typically on the order of femtoseconds. As such, reaching relevant doses would require a minimum of roughly 10^{18} timesteps.

The daunting expense of such a project informs the continued use of mean field kinetic models, such as CRT and CD. The challenge in applying these models successfully lies in ensuring that the kinetics they embody accurately represents the behavior of lattice defects that would emerge from atomistic approaches. This in turn requires a great deal of knowledge regarding the fundamental properties of defects and their clusters spanning their structure and stability as well as their propensity to migrate and interact with sinks or one another. In the multiscale framework, fine grained methods are used to supply this information as parameters for coarse grained methods.

Chapter 4

Defect Clusters in Ferritic Systems

Understanding the fate of vacancy and self-interstitial atoms has long been, and remains, crucial to explaining and predicting the microstructural response of materials to irradiation. These monomer species are the simplest possible defect cluster, and a combination of experimental and computational techniques are employed to clarify the migration energies and configurations for these defects for many material systems. In order to construct a CD or OKMC model, however, the properties of the single defects alone are not sufficient.

Unfortunately, the information available about the more complex clusters is less complete, more uncertain where available, and sometimes apparently contradictory. The legitimacy of kinetic models for microstructural evolution is rooted in a physically meaningful parameterization of the cluster space based on accurate descriptions of the defect configurations, effective migration barriers, and pathways for interacting with other features. The purpose of this chapter is to summarize current knowledge regarding defects in bcc iron and to produce a framework for quantifying that information.

The data that inform a strong parameter set are drawn from a variety of sources. Electronic structure calculations from density functional theory (DFT) are the most reliable computational technique for understanding the basic properties of defects, and provide a great deal of information about single defects in particular. These ab initio methods compute the energetics of atomic configurations which can be used to determine the formation energy of defect structures and even the saddle point energy for defect migration. The size scale that DFT can study is quite limited, however, and the cost of studying larger clusters is often prohibitive.

For such reasons more empirical tools, namely molecular statics (MS) and MD take a prominent role in the study of fundamental properties of large defect clusters. Some degree of caution should be used when turning to these methods as their results may be involve artifacts from the potentials. Consequently, these computational approaches should be tested against experimental data where available to ensure that the predicted properties are reasonable and have some explanatory power.

Isochronal annealing experiments are the most common experimental tool used to study the basic properties of point defects. These experiments allow powerful inferences about the activation barriers for defect migration, perhaps the most important property for kinetic models. Following cryogenic irradiation, a sample is slowly heated while changes in its electrical resistivity are measured. Intense changes in the resistivity that occur at particular temperature ranges, often called recovery stages, become associated with the loss of various defect types to recombination and sinks.

The use of isochronal annealing alone cannot necessarily determine which defects migrate at which temperatures, and this information is typically combined with other techniques to aid in this regard. A powerful complimentary method in this regard is positron annihilation spectroscopy. In summary, this method gathers information about the vacancy distribution in an irradiated specimen based on measurements of positron lifetime. Lengthening positron lifetimes indicate growth of vacancy clusters which in turn implies that vacancy type defects are mobile.

4.1 Defect Properties

4.1.1 Vacancy Defects

Vacancies are simply a vacant lattice site with a slight inward relaxation of the neighboring atoms. The isolated vacancy migrates via a simple exchange with a nearest neighbor atom. No directional preference exists for such a process in a bcc lattice, resulting in a three dimensional random walk. The height of the barriers for this process are still somewhat uncertain in iron. Controversy over the vacancy mobility stems from historical disagreements over which resistivity recovery peaks are tied to the mono-vacancy, resulting in a range of reported migration energies, from 0.55 eV to 1.28 eV[61–65].

Positron measurements make a strong case for vacancy clustering beginning near the lower bound[62]. DFT calculations of the migration barrier in pure iron favor the lower range as well, returning values near 0.65 eV[66]. Other phenomenon reinforce an understanding of higher activation barriers, such as the trends in dislocation loop growth rates[67]. Understanding these discrepancies revolves around a general consensus that vacancies bind to carbon, nitrogen, and other interstitial impurities to form "complexes". The lower temperature peaks involve the migration of the isolated defects while the later recovery stages correspond to dissociation of the complexes[65].

The ground state configuration for di-vacancies occupies second nearest neighbor sites in the bcc lattice, while three and four member clusters consist of the tightest configuration of first nearest neighbors[68]. Extending this trend to larger clusters results in spherical symmetry to the extent the lattice allows, leading to observable voids at large enough sizes. Small clusters of vacancies migrate by individual members of the cluster performing exchanges with $1nn$ atoms, similar to the migration of the isolated vacancy.

In some clusters, the discrete jump may require the formation of metastable configurations[69, 70]. The di-vacancy, for example, must transition to a $1nn$ or $4nn$ configuration when one member makes a nn jump. The other member subsequently makes a similar jump, which returns the cluster to its ground state configuration. Despite moving through higher energy states, the activation barriers are lower for the migration of small vacancy clusters than for the migration of v_1. This trend is consistent with observations of a lower temperature vacancy migration stage under neutron irradiation, as these clusters are formed directly in cascades[71].

Ab initio calculations provide support for a carbon dominated picture of vacancy mobility, predicting a binding between carbon and vacancies of roughly 0.4 eV[72–74]. Though this binding is in itself too small to bridge the gap between the two energies by about half, formation of a vc_2 complex also can be considered. These clusters can be formed by carbon migration to vc complexes[75, 76]. Small mobile vacancy clusters appear to exhibit similar, though not entirely identical, binding with carbon[74, 77]. In commercial alloys, carbon content assuredly exceeds 100 ppm and the formation of impurity complexes undoubtedly plays a crucial role in the behavior of vacancies, although this is to some extent mediated by carbon precipitation.

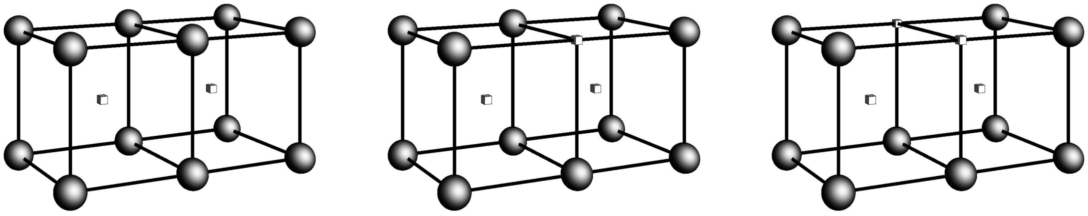

(a) Di-vacancy (b) Tri-vacancy (c) Tetra-vacancy

Figure 4.1: Configurations for vacancy clusters in the bcc lattice

4.1.2 Interstitial Defects

The interstitial is more complicated than the vacancy in bcc lattices, particularly so in iron. Even at the single defect level there are a number of possible configurations. Self-interstitials usually manifest as a "split-dumbbell", with two atoms sharing a single lattice site. When the dumbbell is oriented along a close-packed direction it relaxes into a "crowdion" as the lattice atoms are displaced away from the SIA. The crowdion might be envisioned as three atoms sharing two lattice sites or four atoms sharing three lattice sites, and in the bcc lattice are found in the $\langle 111 \rangle$ direction. Though SIAs appear as crowdions in many bcc metals, iron strongly favors a $\langle 110 \rangle$ dumbbell configuration for isolated SIAs[66, 78, 79].

Despite their orientation, the single interstitial favors migration in $\langle 111 \rangle$ directions through a combined rotation-translation pathway illustrated in Figure 4.2. This mechanism, named after Johnson, results in a final state with a $\langle 110 \rangle$ dumbbell in a different direction from its initial state[80]. As a result of the rotation on every jump the SIA has an effectively three dimensional mobility. This is notably different from crowdions, which migrate with very low activation barriers only along the direction they are oriented.

Clusters of SIAs initially develop as sets of parallel $\langle 110\rangle$ dumbbells occupying nearest neighbor sites[79]. The di- and tri-interstitial are thought to migrate similarly to the single interstitial, with a translation-rotation process that may happen one member at a time or with the entire cluster moving as a unit[78]. Many researchers associate the energy barriers for interstitial and di-interstitial migration with the stage IE and II recovery temperatures respectively[64]. These stages agree surprisingly well with DFT calculations for the Johnson mechanism barrier, which report 0.34 eV for the single interstitial and ~0.42 eV for the di- and tri-interstitial[69, 78].

It is worth noting that prior to the development of potentials tuned to these DFT results, older many body potentials had predicted a much different mechanism for the motion of SIAs and small clusters in MD. In these simulations the favored migration path involved the on-site rotation of a $\langle 110\rangle$ dumbbell into a $\langle 111\rangle$ orientation followed by translation via the crowdion mechanism[81]. The performance of empirical potentials in this case illustrates the limited accuracy of MD and MS, which can provide some basic insights into cluster properties but requires a great deal of outside corroboration in order to draw far reaching conclusions about defect behavior.

As interstitial clusters grow larger, restrictions are placed on the sites that can be occupied by dumbbells due their highly anisotropic nature. Consequently, these clusters develop on sets of lattice sites that resemble platelets, in contrast to the spherical preference in the vacancy case. As additional defects are added to the cluster it increasingly prefers a $\langle 111\rangle$ orientation, resulting in a cluster of crowdions which still take a platelet configuration. These "crowdion bundles" are the ground state for clusters of size 5 or more according to ab initio calculations, with the transition occurring at somewhat smaller or larger sizes in MS depending on the inter-atomic potentials[82]. Figure 4.3 demonstrates the lowest energy configurations for crowdion bundles, which are hexagonally symmetric[83].

Crowdion bundles can be thought of as an extra plane of atoms, and clearly become edge type dislocation loops with an $a/2\langle 111\rangle$ Burgers vector in the large cluster limit. The transition to a $\langle 111\rangle$ orientation at small cluster sizes is associated with the high stacking fault energy inherent in forming a $\langle 110\rangle$ dislocation loop in bcc. There is no clear demarcation between dislocation loops and crowdion bundles, and in many cases the two concepts are equivalently valid for conceptualizing these defect structures. Continuing interstitial absorption upon crowdion bundles nicely explains the development of $a/2\langle 111\rangle$ prismatic loops in iron irradiations, but the rationale for $a\langle 100\rangle$ loops is more elusive. Despite the plethora of mechanisms proposed, the formation of $a\langle 100\rangle$ loops remains very much an open question[84–87].

Crowdion bundles are typically too large to determine saddle point energies, so the activation barriers for migration are inferred from MD instead. A variety of studies with different inter-atomic potentials have concluded that the activation barriers for crowdion bundle motion are exceptionally low, ranging from 0.05 to 0.15 eV, and predominantly independent of cluster size[83, 88–90]. This low activation glide is restricted to the close packed direction, resulting in a crowdion motion which is strictly one dimensional. The prefactors decrease with loop size according to a power law. Laboratory observations of the diffusion behavior

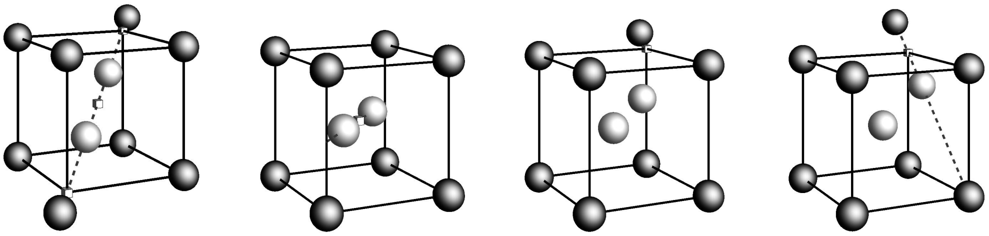

(a) Crowdion (b) ⟨110⟩ dumbbell (c) Johnson migration pathway (d) Johnson mechanism final state

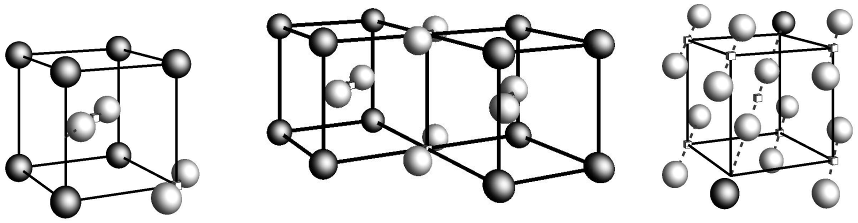

(e) Di-interstitial (f) Tetra-interstitial (g) Seven member crowdion bundle

Figure 4.2: Configurations for self interstitials and their clusters in the bcc lattice

for ⟨111⟩ loops paint a much different picture about their mobility. A similar power law dependence on loop size is reported for the prefactor, but TEM measurements of visible loops in α-iron suggest an activation energy of 1.3 eV[91]. A number of explanations of this discrepancy have been advanced which all involve the binding of interstitial clusters with various impurity atoms or defect complexes which serve as “traps”. Arguments can be advanced for the efficacy of interstitial impurities[92], impurity vacancy complexes[93, 94], and substitutional impurities or small precipitates thereof[95–97] as trapping sites. The precise nature of these traps remains uncertain with any, or possibly all, of these candidates contributing to the reduced mobility.

The properties of the clusters too small to be stable crowdion bundles and too large to behave like the SIA is perhaps the most uncertain of all. For ⟨110⟩ oriented clusters larger than three the Johnson mechanism is forbidden as it would require a change in the cluster habit plane that nearest neighbor jumps cannot accomplish. On-site rotation into a ⟨111⟩ orientation is possible, however, with a similar activation barrier[98]. MD suggests the tetra-interstital, for example, favors a ⟨110⟩ orientation but can easily transition to a crowdion configuration and exhibit low activation one dimensional glide before returning to the ground state[82, 99].

The dynamic behavior of such clusters generates a mixed 1D-3D diffusion pattern, with stretches of 1D glide interrupted by occasional direction changes. It is unclear how, or if, clusters in this size range interact with the traps that alter the behavior of larger crowdion bundles. To further complicate matters, it is nearly impossible to directly obtain experimen-

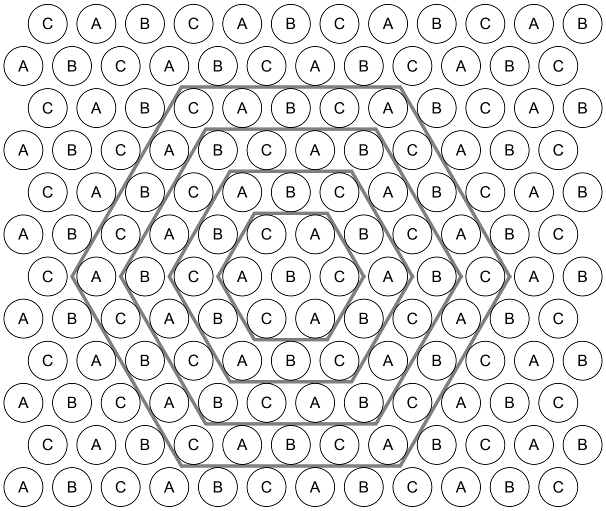

Figure 4.3: Crowdion bundle structure viewed in the ⟨111⟩ direction

tal validation of modeling hypotheses regarding the properties of these intermediate clusters. Furthermore, past experience with empirical potentials suggesting similar metastable state based motion for SIAs casts an additional degree of uncertainty on the real behavior of these clusters. At the present time, knowledge of the mobility of this crucial size range is tenuous at best.

4.1.3 Interaction Properties

The structure and behavior of isolated defects does not quite completely specify the reaction-diffusion system. Defects interact with distributed microstructural features and even one another. Determining which interactions are possible and how they proceed is fundamental in predicting damage development. For the purposes of thin foil irradiations, it is important to consider annihilation at free surfaces, defect-defect clustering, and absorption on dislocations. The free surface is simply treated as a black absorber for defect clusters of all types.

The absorption of point defects at dislocation lines is a core component of microstructure modeling. Small species are absorbed at dislocations via the climb process, adding “jogs” to the line. In a cascade damage condition, however, the interactions of larger defect clusters with dislocations are likely of similar importance as the absorption of single defects. In particular, the ability of dislocations to remove dislocation loops from the material could have far ranging implications. The interaction between line dislocations and loops has been heavily studied in MD, which has shown that loops as large as several nanometers in diameter can glide to a dislocation and be fully absorbed by creating a “superjog”[100]. A number of other events can occur, including trapping or bypass at specific stresses[101] and loop dragging for particular relative positions and orientations[102]. The interaction that occurs also changes with ambient temperature[77]. Details aside, it is clear that larger interstitial clusters can be absorbed by these sinks.

The kinetics of defect reactions with one another competes with absorption at dislocations and surfaces, driving the formation of new damage features. A longstanding interest of MFRT models is the region of spontaneous recombination, where an interstitial becomes unstable and collapses into a nearby vacancy. Lattices respond differently to distortion depending on the crystallographic direction, leading to spontaneous recombination volumes that are highly anisotropic[103, 104]. It is, however, common practice to use a spherical equivalent volume in many kinetic models[105]. Estimates of the recombination volume vary from 25 to a 150 atomic volumes, or about 1.5 to 3 nearest neighbor distances for the radius of a spherical equivalent.

The concept of a spontaneous reaction volume must be extended from Frenkel pair recombination to interactions between arbitrary clusters in the context of today's kinetic models. When extending the recombination concept to similar annihilation type reactions it is reasonable to assume a similar behavior. One would not expect a strong dependence of the reaction $i_1 + v_n$ on n, with recombination being the unexceptional case of $n = 1$. Other interactions may require a more careful consideration. MS calculations clearly show that the strain produced by small dislocation loops can cause extremely long, though anisotropic, absorption distances for vacancies and SIAs[106–109]. The high mobility of crowdion bundles in empirical potential calculations is responsible for the enhanced reaction volumes. It is unclear whether this effect, like crowdion glide, would also be diminished by trapping or how the anisotropy of the predicted volumes relax with temperature.

As a final consideration, these models aim to investigate damage in commercial ferritic alloys which contain a number of interstitial impurities and solutes at significant concentrations. Some disconnects may exist between such realities and the fundamental studies of defect properties, which largely focus on a pure matrix only. It is only reasonable to point out that the solute atoms, particularly the roughly 10% Cr, can modify the diffusion and reaction kinetics of defects. Although vacancies preferentially exchange with Cr in the matrix, their other properties are not expected to be change significantly so long as the iron remains in the α phase[110].

Interstitials are more complex. Mixed dumbbells (with one Fe and one Cr) have lower formation energies that vary less between orientations when compared to pure Fe[111, 112]. Cr-Cr dumbbells in an iron lattice have higher formation energies than both Fe-Fe and Fe-Cr dumbells, with almost no difference between the $\langle 110\rangle$ and $\langle 111\rangle$ orientation. In a concentrated alloy this has the dual effect of creating a wider range of defect formation energies depending on local Cr content, potentially weakly trapping interstitials, and increasing the uncertainty about the dimensionality of small cluster motion[113].

4.2 Parameter Selections

To employ OKMC or CD, the dimensions and mobility of each cluster must be specified. A few other properties, such as dimensionality and reaction geometry will be added in later chapters. To simplify the implementation of these properties, the clusters are discussed in terms of groups that share similar characteristics. Table 4.1 gives an overview of these divisions as well as a summary of the expected behavior. Where necessary, the dislocation loop category can be further divided by describing the largest complete "shell" in the hexagonal structure (see figure 4.3) with i_7-i_{18} as first shell loops, i_{19}-i_{36} as second shell loops, and so on. The dimensions of a cluster are contained in its radius, which is based on the cluster's physical configuration. For this purpose, voids and freely migrating clusters are assumed to be roughly spherical, while the remainder of the interstitial clusters take the configuration of a prismatic loop.

Cluster Type	Size Range	Important Properites
Void	v_5+	Immobile with nearly spherical symmetry
Freely Migrating	v_4-i_3	Mobile with well characterized isotropic diffusion
Transitional	i_4-i_6	Mixed 1D-3D diffusion with unknown influences from traps
Crowdion Bundle/ Dislocation Loop	i_7+	Platelet configuration with low activation 1D glide slowed by trap interactions

Table 4.1: Delineation between types of point defect clusters

The mobility of voids and freely migrating interstitial clusters are most straightforward to incorporate into a multi-scale framework. Voids are simply immobile, while SIAs are very well characterized. The strong agreement between isochronal annealing data and DFT calculations justifies the acceptance of those migration energies. Using a single interstitial prefactor of $D_{0,i1} = 10^{11}\text{nm}^2/\text{s}$, the diffusivity of these clusters is fully outlined in Table 4.2.

Cluster	Prefactor	Migration Energy (eV)
i_1	$D_{0,i1}$	0.34
i_2	$D_{0,i1}/2$	0.42
i_3	$D_{0,i1}/3$	0.43

Table 4.2: Diffusion parameters for freely migrating interstitials

In the vacancy case, two sets activation energies are presented for the freely migrating defects. Set v_B closely resembles modeling calculations in pure iron and lies near the lower bound for experimental inferences of the vacancy activation energy, while set v_A is likely more realistic for commercial alloys by roughly accounting for the effects of impurity complex formation, and lies near the upper bound of experimental vacancy migration energies.

Despite a preference for using v_A in mean field calculations, v_B may be more appropriate for parameterizing objects in cascade aging simulations where the vacancies are presumably yet to encounter impurities to bind to.

Cluster	Prefactor	Migration Energy (eV)	
		v_A	v_B
v_1	$D_{0,i1}$	1.3	0.67
v_2	$D_{0,i1}/2$	1.25	0.62
v_3	$D_{0,i1}/3$	1.0	0.35
v_4	$D_{0,i1}/4$	1.15	0.48

Table 4.3: Two sets of diffusion parameters for freely migrating vacancies

Additional complexity arises for the transitional clusters and dislocation loops. Whether or not the smaller crowdion bundles respond to trapping in the same way as large observable dislocation loops is unclear. A proper description of the mobility of transitional clusters is even less clear, given a multiplicity of configurations and the mixed mode nature of their diffusive processes. To this end, multiple sets of conceivable activation barriers are presented for interstitial clusters, and their effects will be examined in later chapters. These sets include the two limiting cases for trap interaction (i_A,i_D) in addition to one set that forbids trapping for the transitional clusters(i_B). Set i_C is included to examine the possibility that traps do not impact the smallest of crowdion bundles, and a linear increase in migration energies is implemented for the first shell. This approach has enjoyed some success in modeling similar experiments in molybdenum[49].

Cluster	Prefactor	Migration Energy (eV)			
		i_A	i_B	i_C	i_D
i_4	$D_{0,i1}/4$	1.3	0.1	0.1	0.1
i_5	$D_{0,i1}/5$	1.3	0.1	0.1	0.1
i_6	$D_{0,i1}/6$	1.3	0.1	0.1	0.1
$i_{7\leq n\leq 18}$	$D_{0,i1}n^{-0.7}$	1.3	1.3	$0.1\rightarrow1.3$	0.1
$i_{n\geq 19}$	$D_{0,i1}n^{-0.7}$	1.3	1.3	1.3	0.1

Table 4.4: Diffusion parameters for larger interstitial clusters

In addition to specifying the size and mobility of each cluster, CD and OKMC both require some predetermined sense of the dimensionality of motion and the conditions of reaction between objects. A Monte Carlo approach can account for dimensionality by restricting the allowed jumps to the appropriate dimensions or assigning different rates to jumps in different directions. Modifications of reaction volumes to account for anisotropy are even simpler. Mean field calculations require a more invasive set of modifications, which alter the formulations of the diffusion coefficients and reaction rate constants. Due to such complexities, the traditional set of assumptions outlined in Chapter 3 will be adopted first, and attempts to relax them will be introduced later.

In order to apply the Smoluchowski rate to a given reaction pair, the reaction radius for that pair must be specified. The reaction radius should give a good approximation of the spontaneous reaction volume for clusters of arbitrary size. A simple parameterization involves the definition of an interaction distance r_0, which is added to the cluster's physical radii to calculate the reaction radius

$$r_{i,j} = r_i + r_j + r_0 \tag{4.1}$$

where the recombination radius for comparison to classical rate theory would be $r_{I,V} = r_I + r_V + r_0$. Similar approaches to defect cluster parameterization have been implemented in OKMC and MFRT models[42, 114–116]. The clustering distance, r_0, is held fixed while the definition of a cluster's physical radius depends on geometric configuration and size. For clusters which take a spherical shape the radius is calculated as

$$r_n = \left(\frac{3n\Omega}{4\pi}\right)^{1/3} \tag{4.2}$$

where n is the number of lattice sites occupied by the cluster. For the prismatic loop arrangements taken by interstitial clusters it is more appropriate to use

$$r_n = \sqrt{\frac{n\Omega}{\pi b}}. \tag{4.3}$$

Reaction volumes of this form are applied to reactions between any arbitrary combination of clusters, and all reactions are considered to progress to completion, leaving only one product species.

Similarly, all clusters are also allowed to emit a single monomer (i_1 for I type clusters, v_1 for V type) regardless of cluster size with the obvious exception forbidding a monomer species from emitting itself. The binding energies that govern the kinetics of these dissociations follow capillary law formulas

$$E_{b,n} = E_{b,0} - E_{b,1}\left(n^{2/3} - (n-1)^{2/3}\right) \tag{4.4}$$

for a cluster with n members. The constants in Table 4.5 provide a good representation of the bcc iron system[117].

Type	$E_{b,0}$	$E_{b,1}$
Vacancy	1.73	2.59
Interstitial	4.33	5.76

Table 4.5: Capillary law constants for α-Fe (eV)

All clusters are allowed to absorb fully on dislocations, resulting in a complete annihilation of the cluster. The rate of absorption is governed by the sink strength outlined in Eq. (3.20) which requires an interaction radius between the cluster and the dislocation. Similar to the approach for clustering, this distance is calculated as the radius of the cluster added to a dislocation core radius, $r_{c,i} = r_i + r_{c,0}$. To account for bias, the dislocation sink strength is increased for all interstitial clusters via a multiplication factor, B. The bias factor is also applied to the reaction rate constants for $i_n + i_m$ type reactions. The reaction system that has just been outlined is constructed from the parameters listed in Table 4.6.

Property	Symbol	Default Value
Foil Thickness	L	100 nm
Dislocation Density	ρ	5×10^{14} m^{-2}
Lattice Parameter	a	0.287 nm
Dislocation Core Radius	$r_{c,0}$	$1.5b$
Clustering Distance	r_0	$1.5b$
Dislocation Bias	B	1.10
Visibility Threshold	–	2.5 nm

Table 4.6: Default values for the thin foil α-Fe reaction-diffusion system

Chapter 5

Primary Damage

Numerous irradiations of various ferritic alloys with heavy ions have been performed under in situ observation at the IVEM facility over the past decade. A variety of model[12] and commercial[13] alloys have been examined using a specific and consistent set of irradiation conditions detailed in Table 5.1. The available data spans several alloys and a wide range of ambient temperatures, suggesting that this condition is ripe for analysis. Cluster dynamics calculations for this condition, however, require a set of source terms designed to specifically replicate the defects generated as primary damage for these irradiations.

Beam	1 MeV Kr^{++}
Ion Flux	$5 \times 10^{-3}\mathrm{nm}^{-2}\mathrm{s}^{-1}$
Dose Rate[1]	$1.5 \times 10^{-3}\mathrm{dpa/s}$
Angle of Incidence	15^{o}

Table 5.1: Heavy ion irradiation specifications for in-situ experiments

5.1 Source Term Calculations

Generating the primary damage profile arising from ion irradiation requires knowledge of the recoil density, which is defined here as the expected number of primary knock atoms generated as a function of energy and depth. By assigning point defects to each recoil, the damage rate as a function of depth follows

$$g_0(x) = \int \rho_{PKA}\left(x, T\right) \nu(T) f(T) dT \tag{5.1}$$

where $\nu(T)$ describes the number of point defects expected as a function of recoil energy and $\rho_{PKA}\left(x, T\right)$ described the distribution of PKAs as a function of depth and energy. The

---

[1] The dose rate is consistent with the values used by the experimentalists and is included only to facilitate comparison with experiments, and was never used for generating damage in any modeling calculations

convention developed by Norgett, Robinson, and Torrens[118] is employed for a standard definition of ν, where

$$\nu_{NRT} = \frac{0.8\xi(T)T}{2E_d} \tag{5.2}$$

where ξ is the Lindhard partition factor, used to roughly account for electronic stopping. Cascades are well known to produce fewer defects than expected by any of the conventional damage formulas, however, so Eq. (5.1) includes a surviving defect fraction, f, with typical values ranging from 0.1 to 0.5.

Source terms for modern kinetic models can encompass defects beyond the Frenkel pair. This capability allows the production of clusters directly with independent source terms, consistent with MD cascade observations. To take full advantage of this, the net production rate g_0 needs to be divided into into production rates for each of a variety of defect clusters to form $\vec{g}$. Incorporating a defect cluster mass fraction vector allows the damage to be divided among clusters of various sizes. We define each entry in the vector to be the average fraction of monomers generated in a cascade that are included in a cluster of the corresponding size. The mass fraction vector has a few noteworthy properties, primarily that it varies strongly with recoil energy. Additionally, in order to conserve mass the sum of all values for interstitial clusters or all vacancy clusters must be unity.

$$\begin{aligned} \vec{\chi} &= [\chi_{v_N}, ..., \chi_{v_3}, \chi_{v_2}, \chi_{v_1}, \chi_{i_1}, \chi_{i_2}, \chi_{i_3}, ..., \chi_{i_N}] \\ 1 &= \sum_{n\in I} \chi_n = \sum_{n \in V} \chi_n. \end{aligned} \tag{5.3}$$

It is useful to introduce a modified version of the mass fraction vector in which each component is divided by the number of monomers that compose that cluster,

$$\vec{\chi'} = \left[\frac{\chi_{v_N}}{N}, ..., \frac{\chi_{v_3}}{3}, \frac{\chi_{v_2}}{2}, \chi_{v_1}, \chi_{i_1}, \frac{\chi_{i_2}}{2}, \frac{\chi_{i_3}}{3}, ..., \frac{\chi_{i_N}}{N}\right] \tag{5.4}$$

such that $\nu(T)\vec{\chi'(T)}$ is the average cluster population resulting from a cascade of energy T.

Applying $\vec{\chi'}$ to Eq. (5.1) produces a general expression for an array of production rates

$$\vec{g}(x) = \int \rho_{PKA}\left(x,T\right)\nu(T)f(T)\vec{\chi'}(T)dT \tag{5.5}$$

with elements corresponding to those in the mass fraction vector. Knowledge about the survival efficiency and clustering behavior is largely drawn from MD simulations and only available at specific recoil energies. Consequently, the integral in Eq. (5.5) becomes a discrete sum of the form

$$\vec{g}(x) = \sum_{n=1}^{N} f(T_n)\vec{\chi'}(T_n) \int_{T_n}^{T_{n+1}} \rho_{PKA}\left(x,T\right)\nu(T)dT \tag{5.6}$$

where the recoil density is determined by the irradiation condition.

5.1.1 Recoil Distribution Estimates

Calculating the damage rate requires an evaluation of the recoil density. In ion irradiations the recoil density exhibits strong spatial dependence. For a given set of incident ions the recoil spectrum is closely tied to the differential scattering cross section $\sigma_s(E,T)$ and the ion current I(E,x),

$$\rho_{PKA}(x,T) = \int \sigma_s(E,T) I(E,x) \mathrm{d}E \tag{5.7}$$

but this is difficult to evaluate analytically. As such, stochastic simulation of ion tracks using SRIM becomes an attractive choice for determining recoil density. When a sufficient number of ions are simulated,

$$\int_{x-\delta x}^{x+\delta x} \int_{T_n}^{T_n+1} \rho_{PKA}(x',T')\nu(T_i')dx'dT' = \frac{\phi}{n_{ion}} \sum_{\substack{|x-x_i|\leq \delta x \\ T_{n-1}\leq T_i \leq T_n}} \nu(T_i) \tag{5.8}$$

where x_i and T_i describe the position and energy of the i^{th} recoil. This method is used to generate a spatially discretized approximation of the number of defects produced,

$$\begin{aligned} \rho(x_m,T_n) &= \frac{1}{\Delta x} \int_{T_n}^{T_{n+1}} \int_{x_m-\Delta x/2}^{x_m+\Delta x/2} \rho_{PKA}\left(x,T\right)\nu(T) dx dT \\ &\simeq \frac{\phi}{n_{ion}\Delta x} \sum_{i\in\{m,n\}} \nu(T_i) \end{aligned} \tag{5.9}$$

which we refer to as the discretized damage density, where Δx is the spacing between spatial nodes. The notation $i \in \{m,n\}$ denotes the set of recoils produced by SRIM that fall within the appropriate bounds on position and energy as displayed in the integral form. The resultant formula is a fully discretized version of Eq. (5.5)

$$\vec{g}(x_m) = \sum_{n=1}^{N} f(T_n)\vec{\chi}'(T_n)\rho\left(x_m,T_n\right). \tag{5.10}$$

An appropriate energy discretization for the above method should be tailored to match atomic scale models of recoil events. Cascade simulations in MD provide the most reliable and extensive information about early timescale damage development. For the purposes of this simulation, a cascade database was generated at representative energies of 1, 5, 10, and 20 keV. At energies higher than 20 keV, cascades in iron are observed to split into a well known “sub-cascade” structure[119, 120]. In the sub-cascade structure, the initial recoil is sufficiently energetic that secondary recoils are separated by distances large enough to result in two distinct damage regions. Each sub-cascade resembles an isolated damage structure equivalent to a lower energy cascade. Defect survival and self-clustering are not expected to vary as strongly in this energy range.

The roughly invariant nature of highly energetic cascades suggests that a single energy increment covering all energies above the sub-cascade threshold is sufficient to include high energy recoils in the framework of Eq. (5.10). There is one notable objection to this approximation, namely that the damage generated by a high energy recoil is artificially restricted to the location where the recoil is generated. A high energy recoil may realistically travel distances spanning several spatial nodes as a result of channeling, thus generating sub-cascades distributed along the path. The degree to which this impacts the damage distribution is determined by the fraction of energy deposited in high energy recoils.

Including the spatial extent of sub-cascade damage requires a recursive modification to the discretized damage density. Rather than treating high energy recoils as localized in space, they can be allowed to deposit energy over several increments. Primary recoils above a threshold energy are divided into a series of secondary recoils. Any of these secondary recoils above the threshold are divided into tertiary recoils, and so on. Expanding the framework of Eq. (5.1) to accommodate this process involves discretizing the high energy recoil spectrum and simulating each energy increment as an incident self ion. The damage from a secondary track is divided among lower energy bins and across space according to

$$\rho_\beta(x_m, T_n) = \frac{1}{\nu(T_n) n_{ion}} \left[\sum_{i \in \{m,n\}} \nu(T_i) + \sum_{\alpha=0}^{m} \sum_{\gamma=N_L+1}^{\beta-1} \left(\sum_{i \in \{m-\alpha,\gamma\}} \nu(T_i) \rho_\gamma(x_\alpha, T_n) \right) \right] \tag{5.11}$$

where the set of recoils (i) is generated by self-ions at an initial energy of T_β and N_L is the number of energy bins restricted to one spatial increment. The first term handles damage generated locally through lower energy cascades while the second considers higher energy recoils that require further division. These factors are generated recursively, starting at bin $\beta = N_L + 1$ where the second term vansihes. To construct the damage density,

$$\rho(x_m, T_n) = \frac{\phi}{n_{ion} \Delta x} \left[\sum_{i \in \{m,n\}} \nu(T_i) + \sum_{\alpha=0}^{m} \sum_{\beta=N_L+1}^{N_T} \left(\sum_{i \in \{m-\alpha,\beta\}} \nu(T_i) \rho_\beta(x_\alpha, T_n) \right) \right] \tag{5.12}$$

where N_T is the total number of energy discretizations, including those treated non-locally.

Both approaches were considered for the irradiation of Fe-9Cr with 1 Mev Krypton. Several interesting aspects of the primary damage profile for this case are presented in figure 5.1. Comparisons of the damage density from the primary recoil analysis of Eq. (5.10) and sub-cascade analysis of Eq. (5.12) are shown with SRIM estimates of the damage energy distribution. The primary recoil calculations closely matched SRIM's Kinchin Pease "quick" calculations[2]. The damage spectrum given by a complete calculation, however, much more closely resembled the sub-cascade based source term calculation. The primary difference was a notably less uniform damage profile in the sub-cascade analysis which deposited significantly fewer defects near the surface. The fraction of damage assigned to high energy cascades also differed between the two approaches. The sub-cascade analysis assigned significantly less damage to the highest energy increment, as very high energy recoils lose energy

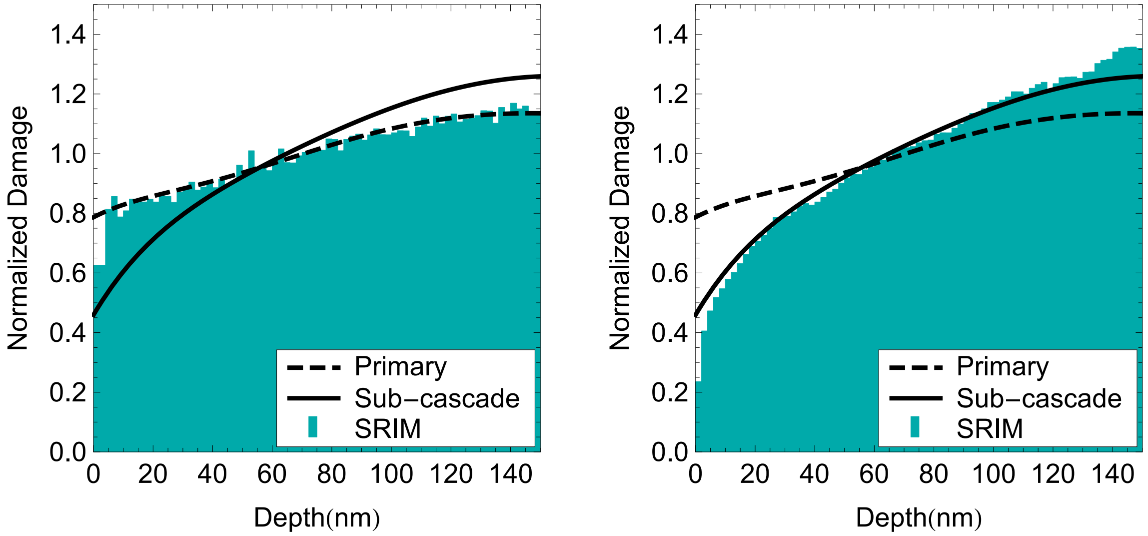

(a) Calculated damage distributions as compared to a SRIM "quick calculation" damage energy distribution

(b) Calculated damage distributions as compared to a SRIM "full cascade" damage energy distribution

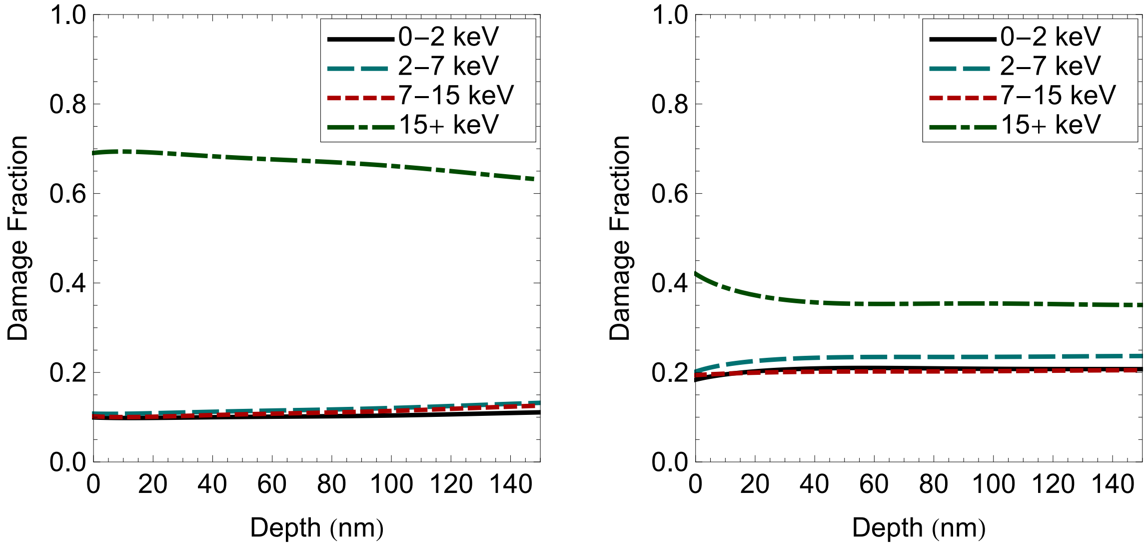

(c) Fraction of damage energy in different ranges following primary recoil analysis

(d) Fraction of damage energy in different ranges following subcascade analysis

Figure 5.1: Primary damage profile for heavy ion irradiation of iron

in numerous low angle collisions between denser cascade events, however the amount of damage in each energy range did not vary strongly with respect to depth in either case. All subsequent calculations employ the sub-cascade analysis due to its more realistic spatial distribution.

5.1.2 Defect Clustering and Survival

The surviving defect fractions and clustering behavior associated with cascade damage must be specified before source terms can be calculated. For a simple example of this process, consider Frenkel Pair damage. In this case, defects come only in clusters of one ($\chi_{i_1} = 1$,$\chi_{v_1} = 1$) and the survival fraction is unity ($f = 1$). Cascade damage requires a more complex characterization, drawing on information from small scale damage simulations.

For our calculations, the cluster partition vector for heavy ions was generated from averaging over the product of MD cascades in α-Fe. Though the intended application is FeCr, independent studies have found almost no difference in defect production between the two systems[122, 123]. The inter-atomic potential selected for these simulations promotes the correct ground states for small interstitial clusters in iron. Lattice defects were identified at the conclusion of each simulation using a Wigner-Seitz cell approach. This methodology involves dividing space into regions bounded by planes that are equidistant to two points on the perfect lattice. Each lattice site is then associated with a cell containing all space nearer to that lattice point than any other. Defects are identified based on the number of atoms contained within each Wigner-Seitz cell. Empty cells are identified as vacancies and doubly occupied cells are identified as interstitials.

A competing algorithm draws spherical cells around each lattice site with a typical cutoff radius of about $^1/_3$ of a lattice parameter. Empty cells are identified as vacant sites while atoms not contained within a sphere are identified as interstitial. Certain inherent advantages are associated with each approach. For example, the isolated SIA in the latter method takes the form of two atoms identified as interstitials on opposing sides of a vacant lattice site. The SIA presents as a combination of three objects comprising a single defect, which slightly complicates any automation of the defect counting process. On the other hand, this method preserves some information about the orientation of isolated SIAs and allows for more detailed visualizations.

Clusters of defects can be identified in both approaches, either through visual judgment or automated algorithms. In our automated analysis, interstitial cells were considered to be clustered at fourth nearest neighbor positions or closer. For vacant cells the separation criteria was reduced to a second nearest neighbor distance. Select cascades were analyzed with both identification methods and hand counted before comparison to the automated clustering algorithm showing no difference in the defect cluster population.

---

[2] There is a known flaw in the SRIM code that calls the magnitude of vacancy distribution estimates into question, particularly for full cascade calculations. The damage distribution estimates were obtained instead from the damage energy according to the procedure recommended by Stoller[121]

The defect clusters present at the conclusion of MD cascades were used to initiate OKMC aging simulations. These calculations began with the appropriate object placed at the center of mass of each of the defect clusters identified from an MD cascade. The Monte Carlo simulations were run in cubic boxes with black absorber boundary conditions. The center of the box was coincident with the center of mass of all defects in a cascade. An aging simulation terminated when no objects remained in the box with an event frequency higher than a specified cutoff. At the time of termination the remaining box contents were added to the objects absorbed at boundaries to determine the final defect composition. Each cascade was aged 500 times, reducing the statistical uncertainty of the aging process far below that of the cascade database itself. The size of the box was expanded until subsequent expansions failed to change the surviving defect fraction beyond the statistical error.

As discussed in Chapter 4, the mobility of many defects in iron are presumably reduced by the presence of foreign interstitial atoms. Any such effects were deliberately neglected in these OKMC aging simulations, which adopt a set of mobility parameters guided by the behavior of defects in pure iron. In particular, the mobility of clusters was generated using mobility sets i_D and v_B as listed in Tables 4.3 and 4.4. Interstitial clusters of size 4 or larger were restricted to one dimensional mobility while other clusters were allowed to jump in any direction. The effects of cascade aging on the cluster population are shown in figure 5.2.

After the MD stage, the bulk of damage remained as single defects, particularly for low energy cascades. The maximum size was largely equivalent for vacancy and interstitial type clusters and increased for both with cascade energy. The observations of clusters with larger than roughly six members occurred only at the two higher cascade energies. The aging process increased cluster sizes and reduced the number of single defects for cascades at all energies. For lower energy cascades, these trends are clear and straightforward, but are slightly more convoluted for the higher energy cascades. It might appear, for example, that in 10 and 20 keV cascades the preponderance of clusters around size 20 decreases after aging as the concentration values are lower in magnitude. This is offset by the appearance of cluster sizes not observed at all in the MD. Interpreting the information contained in the mass fraction vector is often greatly simplified by looking at the clustering fraction and mean cluster size rather than the individual values. These two quantities are defined here as the sum of all values except the single defects, and the mean value of the mass fraction weighted by cluster size, respectively. These calculations are shown alongside the survival fraction in figure 5.3.

Around 40% of defects were found in clusters following MD cascades. This is largely consistent with the body of work done in iron[124–127], and similar to findings in other BCC metals[128]. The clustering fraction roughly doubled after aging in all cases. The resultant increase in mean size for vacancy clusters during aging was generally larger than that for interstitial clusters. Interstitial clusters exhibited largely the same behavior in the aging process regardless of ambient temperature, though a modest difference in the size of interstitial clusters emerged at higher cascade energies. Vacancies, on the other hand, exhibited a decrease in both clustering fraction and mean vacancy cluster size with rising temperature. The drop in clustering fraction was associated with the evaporation of weakly

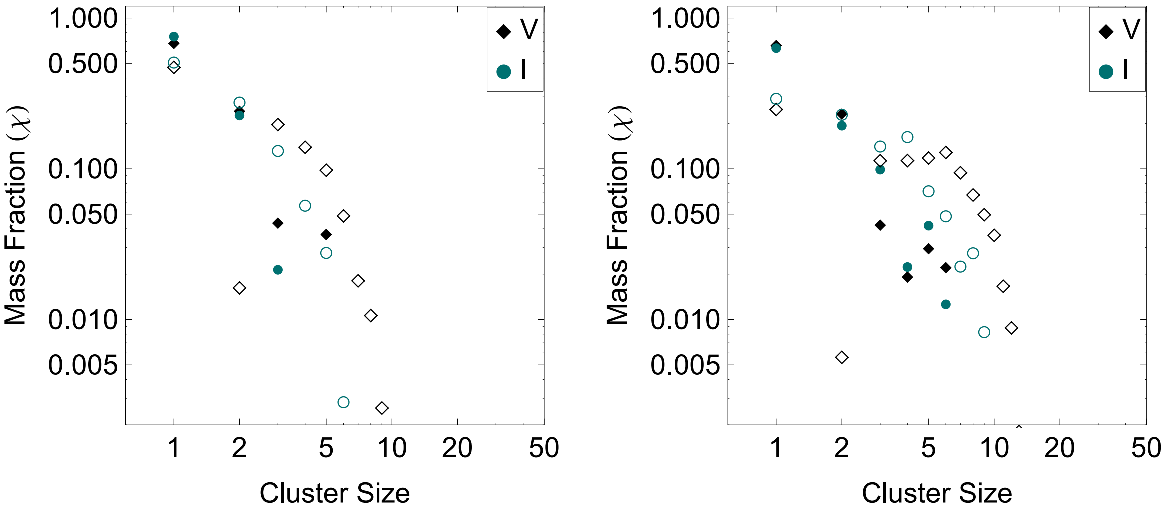

(a) 1 keV (b) 5 keV

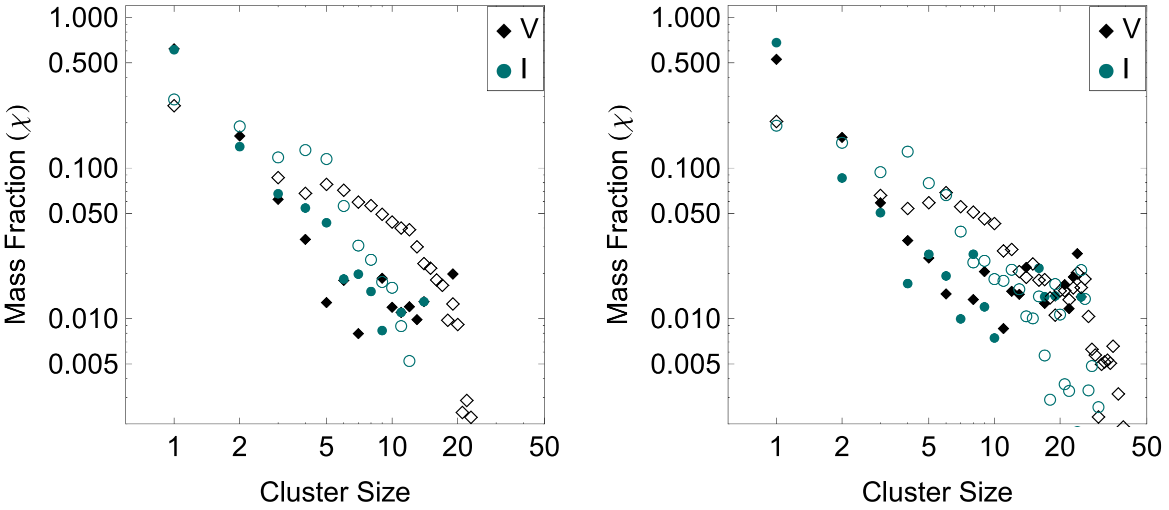

(c) 10 keV (d) 20 keV

Figure 5.2: Defect production by size for cascades of various energies in bcc Fe. Filled points indicate the mean distribution from MD simulations while open points indicate the mean distribution following cascade aging at 573 K. The concentration range was truncated for clarity and some points below the lower bound do not appear.

bound small vacancy clusters, particularly the di-vacancy.

Defect survival was significantly higher for lower energy cascades than higher energy ones during the MD stage. Aging the cascades reduced the number of defects in all cases, but the effect was more pronounced for the lower energy cascades. The surviving defect fraction was not influenced by the aging temperature, nor should it be. Survival is modified only by

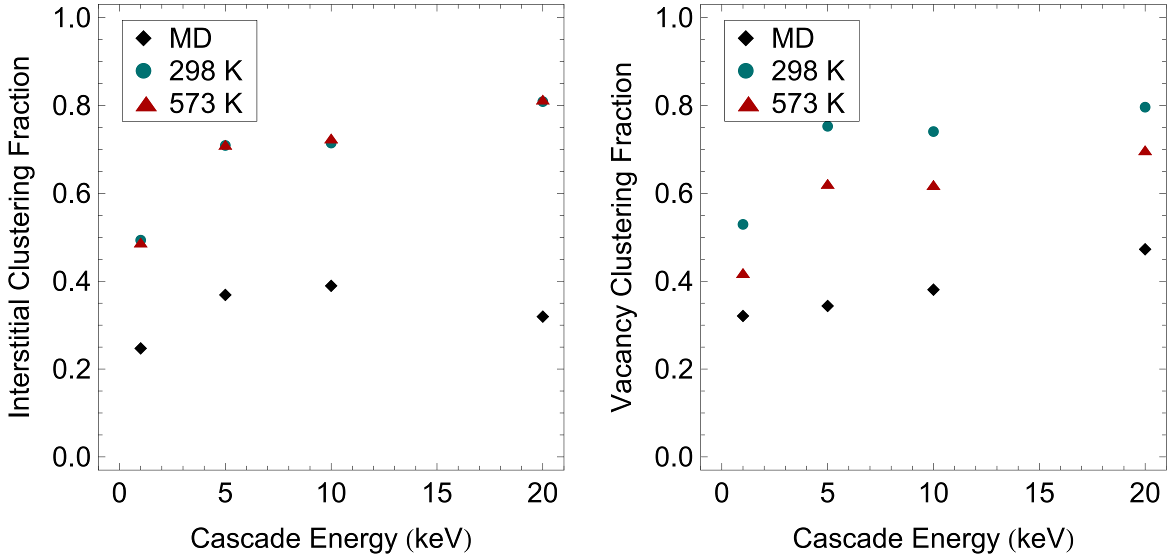

(a) Interstitials found in clusters $(1-\chi_{i_1})$ (b) Vacancies found in clusters $(1-\chi_{v_1})$

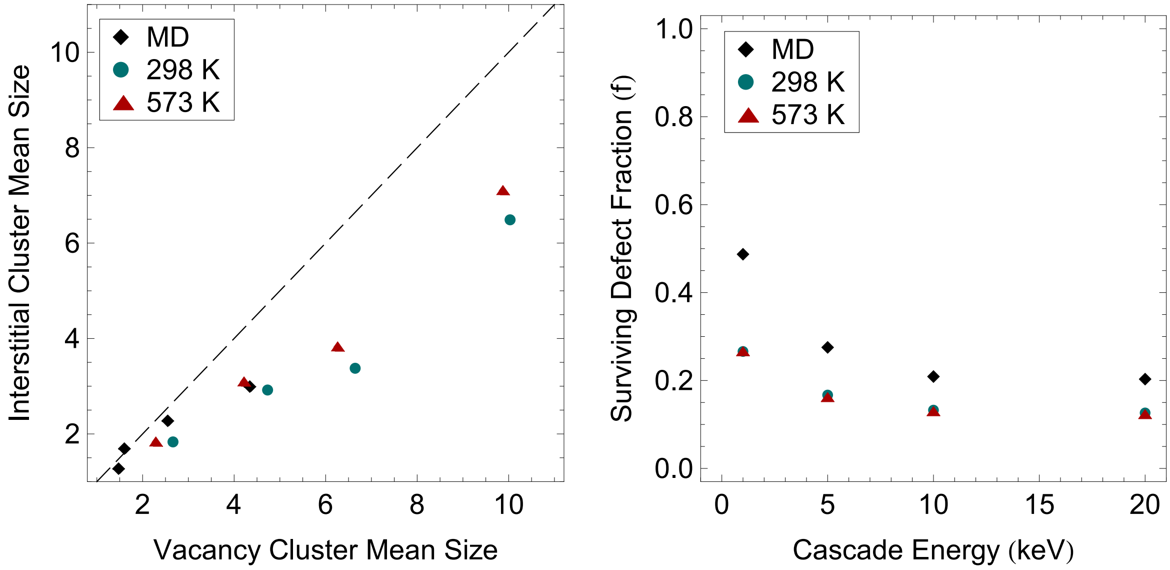

(c) Weighted mean size of defect clusters (d) Mean surviving defect fraction

Figure 5.3: Trends in intra-cascade clustering behavior before and after thermal aging

recombination events, not self-clustering. The interstitials all move on a much more rapid scale than the vacancies, suggesting that recombination is solely a function of interstitial mobility and will remain more or less identical so long as interstitials remain highly mobile (above roughly 100 K).

5.2 Long Term Evolution

We utilized the values of f and χ from small scale methods in Eq. (5.12) to create source terms for Krypton ion irradiations for CD. As a point of comparison, these calculations were also performed using assumptions of Frenkel pair damage. We did this to isolate the effects of cascade damage on long term evolution. Using a Frenkel pair source term is somewhat analogous to an electron irradiation condition, although the spatial distribution of damage is not correct. Interestingly, experiments suggest that a dislocation loop dominated microstructure should develop for a wide range of temperatures under both irradiation conditions.

The Frenkel pair case was analyzed using all four interstitial mobility sets and both vacancy mobility sets listed in Tables 4.3 and 4.4. In the case that represents no trapping of dislocation loops whatsoever (i_D) no observable loops were formed. In each of the other cases, the density of observable defects reached a saturation value within 0.1 dpa and remained constant thereafter. The average size of observable loops grew linearly with time, with the faster growth rates occurring with lower saturation densities. In some cases the loops grew to the maximum size considered by the system resulting in an artificial stagnation in loop growth. Generally speaking, mobility sets that assume a greater number of low activation energy clusters resulted in lower loop densities. Examples of these trends are illustrated in figure 5.4.

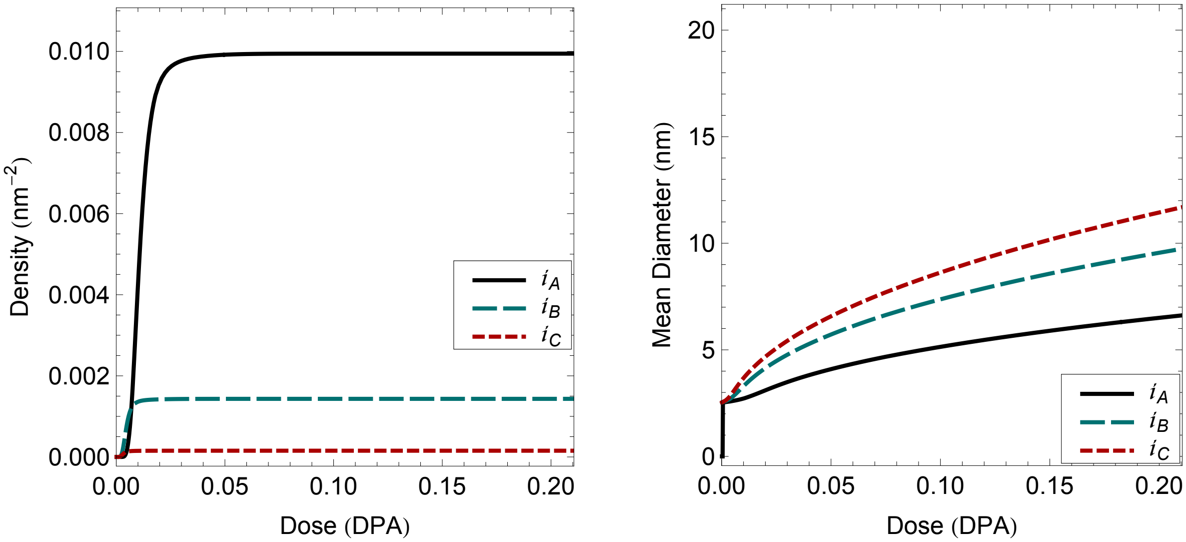

(a) Areal denisty of observable loops

(b) Mean size of observable loops

Figure 5.4: The effect of interstitial mobility assumption on dislocation loop evolution for Frenkel Pair damage at 300 K

The saturation in loop density occurred for the entire temperature range investigated, though the saturation density changed significantly. Arrhenius plots of the maximum loop density are presented for various mobility sets in figure 5.5. The saturation densities spanned several orders of magnitude in all cases, however the temperature dependence became more severe with an increased number of mobile interstitial clusters. The impact of vacancy cluster mobility on loop density was less evident. Any difference in saturation density was apparent only near the high temperature bound. Increased vacancy mobility halted, or even reversed the decline in loop density with temperature in these scenarios. Saturation densities were most sensitive to vacancy behavior where interstitial cluster mobility was lowest.

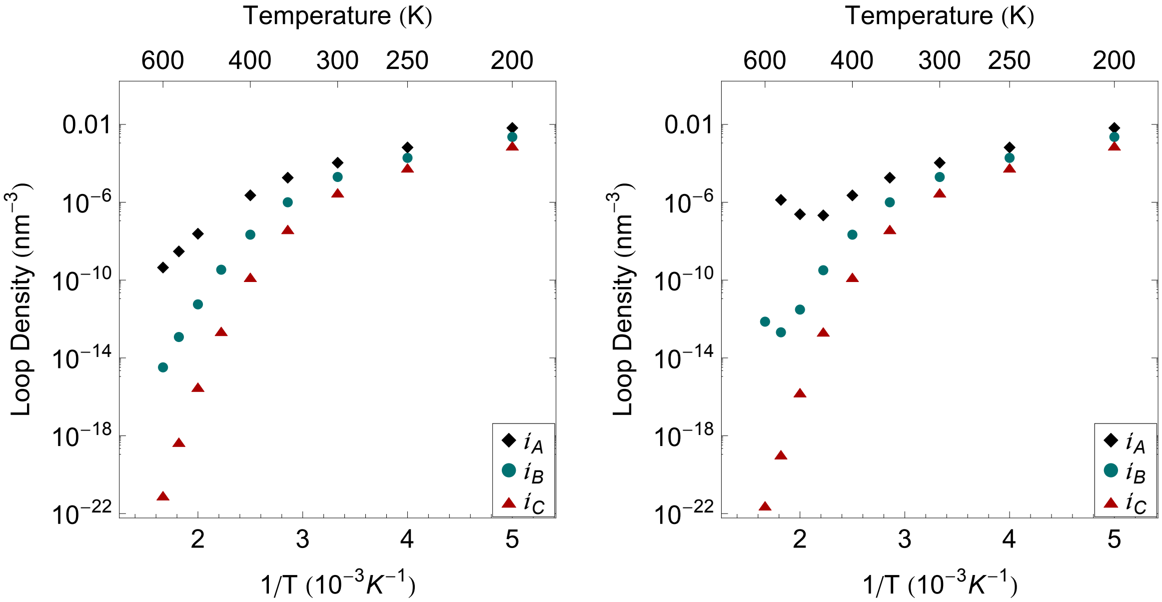

(a) High activation for vacancies, v_A (b) Low activation for vacancies, v_B

Figure 5.5: Effects of temperature on loop saturation when damage appears as Frenkel Pairs

The same approach was applied to heavy ion irradiations. Two different set of source terms were considered, one using the MD database and one which included 300 K aging. As with Frenkel Pairs, no visible clusters were produced when free glide was permitted for all crowdion bundles. In all other cases, observable loops developed, but differently than in the Frenkel Pair case. At many temperatures a saturation in density was not reached for as long as 10 dpa. New loops continuously appeared with negligible growth using either source term. The number densities produced in this manner reached unphysical levels, as demonstrated in figure 5.6.

The damage density appeared to increase most rapidly with more cluster sizes assigned low migration energies. This was not due to a lower retention of interstitial clusters, in fact just the opposite. The number density of sub-visible interstitial clusters for higher activation sets reached higher densities than lower activation sets. The larger density of small loops grew more slowly with fewer, or even none, reaching visible size. Saturation of visible loops is eventually reached for some mobility sets at sufficiently high temperatures.

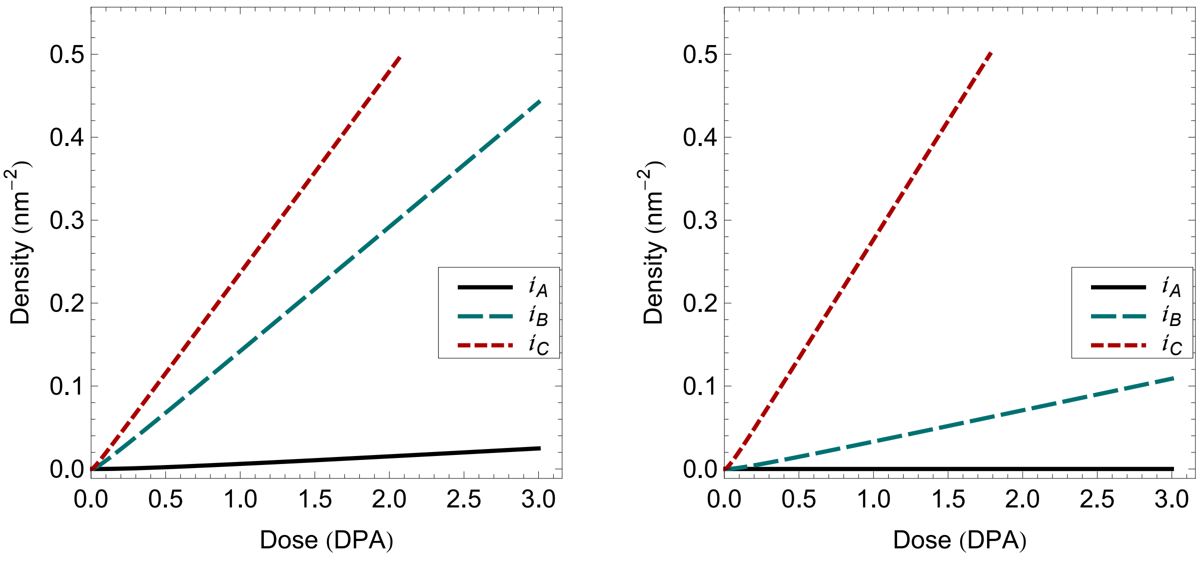

(a) Areal denisty of loops with MD based source terms

(b) Areal denisty of loops with aged source terms

Figure 5.6: Visible loop density trends for cascade damage at 300 K

Figure 5.7 compares the saturation behavior of cascade damage to that of the Frenkel pairs when assuming mobility sets i_C and v_A. Even in cases where damage eventually saturates with cascade source terms, it is at much higher densities.

We assert that these trends in loop development are easily understood in the context of a nucleation and growth paradigm. With Frenkel pair damage, an increasing temperature decreases the steady state monomer concentration, which in turn reduces the nucleation density. Faster growth follows as the same quantity of damage is absorbed on a smaller number of loops. A simple nucleation and growth framework qualitatively accounts for the impact of defect activation energies as well. When crowdion bundles and transitional clusters are rendered immobile they become stable nuclei. In this sense, the reaction chain leading from produced monomers to a stable loop nucleus becomes shorter, and the nucleation density increases. At temperatures where vacancies become mobile they participate in fewer recombination events, as more of them reach sinks and free surfaces, leaving a higher density of interstitials to form loop nuclei than if the vacancies were immobile.

A nucleation and growth description also clarifies the radically different loop population these models predict under cascade damage conditions. In this scenario, stable nuclei are generated directly in cascade damage events. Due to the continuous production of these clusters in the model, a saturation in the number of nucleation sties can never be reached. When some mobility is allowed for crowdions, such as in set i_C, these clusters begin to diffuse as temperature rises, and eventually saturation becomes possible. This reduction in the number of stable nuclei allows for faster growth, leading loops to reach observable sizes more quickly.

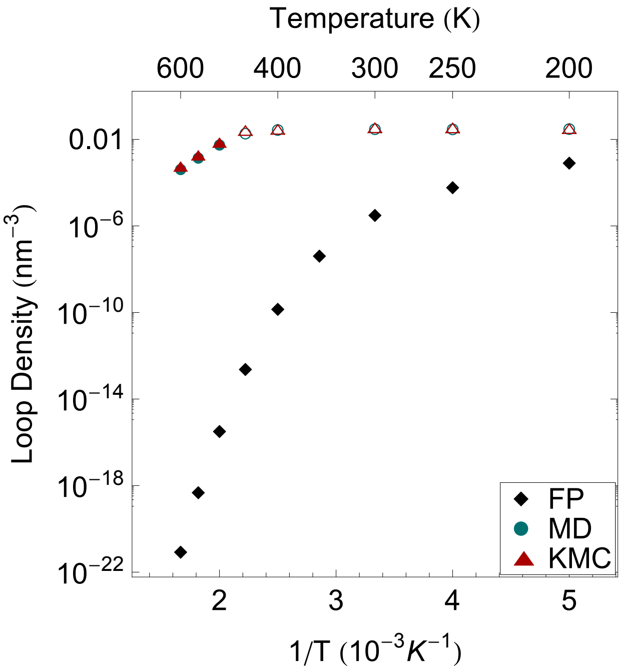

Figure 5.7: Comparison of loop saturation behavior for Frenkel Pair and cascade irradiation conditions. If saturation was not reached by 10 dpa the final density is shown instead (open points).

In situ observations of loop density over the temperature range indicated in our calculations give a much different picture. In electron irradiation, for example, the density of observable loops does not change at all with temperature below about 300 K[129]. Loop density does not vary by more than an order of magnitude for heavy ion irradiations, with no observable change in saturation behavior between 475 and 575 K in model alloy irradiations and less than a factor of two difference from room temperature irradiation (see Figure 2.1). The data in commercial alloys looks similar. These densities are significantly lower than CD predicts with cascade based source terms, even at high temperatures. The calculations presented in this section simply cannot be reconciled with experimental data.

We emphasize that any resolution is not likely to lie in the fundamental properties (i.e. migration energy, dimensionality, recombination distance) of defect clusters. Though many details of these clusters remain uncertain, the mobility sets we have used fully cover the range of reasonable values. Past research often focuses on fine tuning defect migration energies to achieve the desired results, however our results clearly indicate the untenability of this approach when multiple temperatures and damage conditions are considered. Over-nucleation in cascade damage conditions, for example, might be relaxed by simply assuming that crowdions have a lower effective mobility barriers than we have assumed in i_C, but this would only further discourage loop nucleation in the case of electron irradiation. Furthermore, any proposed migration energy set that satisfies experimental observations for ion irradiation at a particular temperature will show under-nucleation at higher temperatures and over-nucleation at lower ones. Indeed, the alloying effects mentioned in Chapter 4 suggest that the interstitial mobility is actually over-estimated by our parameters, and accounting for this would worsen over-nucleation.

We also find it unlikely that the dimensionality of cluster motion holds the key to resolving this conundrum. The nucleation catastrophe observed in the heavy ion case should occur regardless of whether some clusters diffuse with one dimensional or mixed dimensional character, so long as they continue to respond to traps. If none of the clusters respond to traps, the damage depletes on other sinks independent of dimensionality. The nature of the quandary is unaffected. Other oft finessed kinetic factors such as the size and shape of reaction geometries or the dislocation bias are similarly unable to give rise to a temperature independent loop density. We set all these factors aside for the moment, and suggest instead that simple thermal activation is a fundamental mis-characterization of the kinetics governing loop nuclei in a high dose rate irradiation environment, such as *in situ* TEM experiments.

Chapter 6

Irradiation Activated Motion

In-situ irradiation experiments have demonstrated that the mobility of loops is often directly influenced by irradiation itself[15, 16, 95, 97, 129–131]. Thermally immobile loops become capable of motion under specific irradiation conditions, which may vary from material to material. Interestingly, the motion observed in these cases is not the smooth continuous transport one would expect from a typical thermally activated diffusion process. Instead, visible defects move via a series of rapid, isolated, long range jumps which punctuate extended periods of complete immobility. These "hops" take varied lengths which depend on the material being studied, generally on the order of a few to a few tens of nanometers. Hopping may or may not be restricted to some subset of the full loop population. Regardless, these motions appear to significantly alter the defect population by transporting loops to sinks and through a point defect populated medium. Indeed, in situ experiments occasionally observe loops which suddenly vanish, presumably due to annihilation at a foil surface following such a hop. This chapter aims to include such a mechanism in cluster dynamics models to examine its importance.

6.1 Trap Mediation

The hops exhibited under irradiation can be understood rather simply using the same trapping model that explains the low thermal mobility of loops in the first place. In such a framework, loops are thermally immobile because they are bound with high activation energies to trapping sites. Under irradiation, ballistic events deposit the energy required to unbind from a trapping site, following which the loop glides freely until encountering a new trapping site. This "detrapping" process is most clearly understood in the case of heavy ion irradiation, where a cascade near a trapped loop significantly disturbs the matrix with a local spike in heat and pressure. A comparable mechanism exists under electron irradiation, where traps can be negated by ballistic ejection of the constituent atoms. Infrequent irradiation induced detrapping events - followed by rapid glide to new traps - describes precisely the type of motion observed in in-situ TEM experiments.

The trap based approach explains many experimental observations of hop behavior in addition to merely being intuitively attractive. The frequency of hops is directly proportional to increasing beam intensity[97], supporting a recoil based initiation mechanism. Additionally, hop length shows a clear inverse correlation to impurity density[131], consistent with a trap mediation model positing impurities of various kinds as the responsible agent. The modeling community has focused most of its efforts in this area on examining the possible compositions and binding energetics of traps, leaving the dynamic aspects of trap stability under irradiation to conjecture. Consequently, we have examined the ability of cascades to initiate hops with atomistic simulations.

6.1.1 Detrapping Simulations

Cascade simulations near trapped $\frac{a}{2}\langle 111\rangle$ dislocation loops demonstrated the efficacy of the irradiation detrapping model of defect hops. Impurities populating the dislocation lines acted as traps in these simulations. Helium served as a surrogate impurity for carbon and nitrogen to avoid the complexities of inter-atomic potentials required for those elements. Trapped loops were distinguished from free loops based on measurements of the diffusion coefficient, as calculated using the mean square displacement of the center of mass of the loop. Thermal simulation for a 10 ns increment provided sufficient data to calculate diffusion coefficients down to temperatures of 100 K. Possible initial configurations included one, three, or six helium placed at tetrahedral positions near the edge of the dislocation loop, as well as the loop alone. Figure 6.1 demonstrates the initial locations of helium, and shows the effect of impurities on the loop's thermal mobility.

This analysis yielded an activation energy of 0.044 eV and a prefactor of $1.5 \times 10^{11}\text{nm}^2/\text{s}$ for a bare loop, consistent with earlier measurements of loop mobility. Based on qualitative observation, one helium was sufficient to immobilize loops at lower temperatures, while higher temperatures permitted mobility. The initial impurity location proved inconsequential, as helium diffused quickly along the dislocation core throughout the simulation. Other researchers have observed similar behavior with carbon[92].

The loop displayed no evident mobility up to 500 K when laden with three or more helium. Helium still diffused quickly along the core, however, leading to cluster formation. It was unclear whether the further reduction in diffusivity was due to the clustering of helium or simply the presence of additional helium on the dislocation line. Arrhenius temperature dependence disappeared with three or more impurities, in conjunction with visual immobility during the timescale of an MD simulation. Additional calculations studying the binding energy could shed light on the stability of such a configuration for more extended intervals, but would say nothing of ultimate mobility. The loop is certainly sufficiently trapped for the duration of a cascade simulation, regardless.

The cascade detrapping simulations used 1, 5, or 10 keV recoils as potential stimuli and included all six helium for a fully trapped loop. The distance of the of the recoil from loop center of mass varied over 30 trials at each energy, as did the angle of inclination between the recoil location and the loop Burgers vector. The PKA velocity vector took high

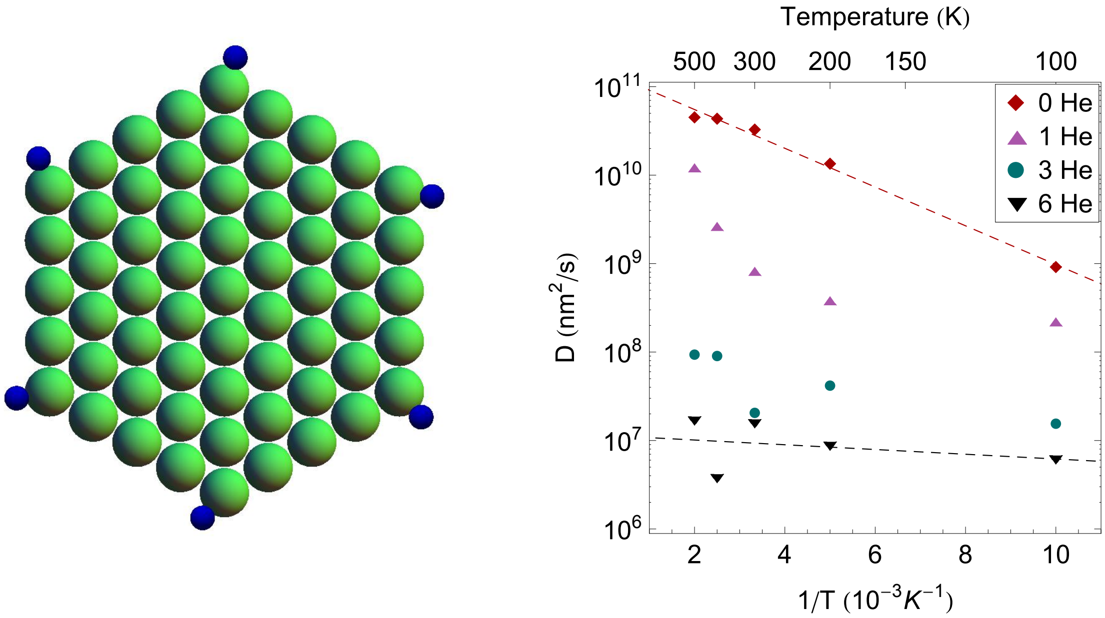

(a) Initial locations of He impurities (blue) viewed along the ⟨111⟩ direction

(b) Diffusivity when laden with various amounts of helium

Figure 6.1: Trapping of 91 member interstitial loops using helium as a surrogate impurity

index directions values to avoid channeling. Qualitatively, little to no long term effects were observed following 1keV recoils. At 5 keV and above, however, some loops clearly de-trapped during the cascades, as shown in Figure 6.2.

The process of cascade induced detrapping, where it occurred, happened after peak displacement as the disordered region begins to collapse and the crystal structure re-emerges. During this process, the loop is drawn toward the cascade core during this phase, leaving the impurities in place. This effect was most pronounced when the cascade core lay in the direction of the loop's Burgers vector, and the magnitude of displacement exhibited by the loop during this process was typically the separation of the loop and PKA. After the cascade had completely collapsed, loops continued to glide indicating an event consistent with the detrapping based hopping model. The impurities at this point diffused thermally, and in some cases, one or more rejoined the dislocation loop. This process occurred most reliably when the recoil was positioned in the direction of the Burgers vector of the loop.

Other dynamic behavior occurred during these simulations but did not result in significant displacement. Recoils positioned in the direction of the Burgers vector caused an early, temporary displacement of the loop away from the cascade during its developing stage. The loop quickly returned to the impurities as the cascade reached peak size. This was possible at all recoil energies, but never resulted in significant displacement unless followed

(a) Initial locations of trapped loop and PKA

(b) Cascade at peak damage partially overlapping loop

(c) Cascade during collapse with rapid loop transport

(d) Resolved cascade demonstrating a loop significantly displaced from its initial position

Figure 6.2: Cascade impact near a 91 member interstitial loop showing interstitials (large, green) vacancies(small, red) and helium(small, blue) at various stages of cascade evolution

by subsequent transport toward the dislocation core. Recoil locations at higher angles to the Burgers vector were less likely to cause either displacement effect.

In 10 percent of the 10 keV cascades, Burgers circuits drawn through the defect cluster center of mass indicated a change in loop orientation, with the Burgers vector aligned to point closer to the cascade core. In an additional 10 percent of all 10 keV cascades, circuits transversing the cluster in different locations revealed junctions in some loops, with $a\langle 100\rangle$ Burgers vectors evident for some fraction of these loops. A change in loop size and shape was also evident in some cascades. Loops usually shrank over the course of cascade interaction. Some grew however, and the distribution of loop sizes was wide, particularly at high recoil energies.

To prepare a first order estimate of how frequently loops should be expected to hop according to this mechanism, we applied the recoil distribution from SRIM used earlier for primary damage. Each recoil was assigned an effective volume given by

$$V(T) = \Omega \frac{T}{3k_b T_m} \tag{6.1}$$

for a recoil energy T and melting temperature T_m. The detrapping frequency was estimated from the cascade volumes by summing over all recoils

$$\nu_{DT} = \frac{\phi \sum_i \eta_{DT} V(T_i)}{\Delta x} \tag{6.2}$$

where η_{DT} is some detrapping efficiency less than 1. Our simulations indicated that for cascades near 1 keV in energy, the appropriate efficiency is zero. Parameterizing cascades in the 5, 10, and 20 keV energy ranges is less straightforward. Applying an efficiency factor of unity suggested a detrapping rate of 0.14 Hz at the center of a 100 nm foil for the 1 Mev Kr irradiation condition. The MD simulations qualitatively suggested that reasonable values for η_{DT} are close to 0.3, although a more thorough coverage of cascade locations within the loop solid angle may result in lower or higher values. Not all detrapping events would result in a visible hop, as backward glide toward the original trap is also possible. Assuming hops result from half of detrapping events, this mechanism remains feasible for hop frequencies on the order of 10 per dpa.

6.1.2 Modeling Discontinuous Motion

The complex dynamics of interstitial cluster transport, as illuminated by in-situ experiments, hold two important implications for large scale kinetic models of radiation damage accumulation at high dose rates. Otherwise stable loop nuclei are free to migrate to free surfaces, background dislocations, or other sinks and may even coalesce into a single cluster as a result of an irradiation induced detrapping. Sudden disappearance of visible damage occurs frequently, lending credence to a loop density kept in equilibrium via such mechanisms. The nucleation catastrophe that reaction-diffusion based models, like the CD model used here, have predicted when damage appears as cascade debris may be alleviated through such processes. Additionally, in the paradigm of a cluster population that alternates between states of limited mobility at trapping sites and free glide elsewhere, cascade debris is likely produced into the latter condition. Migration to sinks or other clusters competes with the formation of an immobile loop nuclei (which occurs as a result of trapping interactions with impurities) to be the fate of large clusters produced in cascades.

Cluster dynamics models can accommodate the hopping motions of loops in a number of ways. This section outlines two competing methods of incorporating detrapping kinetics. The first involves increasing the diffusivity of dislocation loops to account for hops. The second defines two separate types of cluster, a trapped loop and a free loop, and prescribes kinetics for transitioning between the two. We refer to these approaches as the “two-mode” and "two-state" models respectively. Both require some quantification of the hop length, which in the context of trap mediation corresponds to the mean spacing of traps along a cluster's glide cylinder. To calculate such spacing for a given loop, λ_i, it is useful to consider the loop's cross section for interacting with traps such that

$$\frac{1}{\rho_T} = \lambda_i \sigma_{i,T} \tag{6.3}$$

where ρ_T is the trap density.

Quantifying these cross sections presents a daunting challenge given the numerous possible trap compositions. Fortunately, potential traps can be roughly divided into two categories: those that act on the dislocation core directly and those that act when positioned interior to the loop. The former includes traps comprised of interstitial or substitutional impurities. The appropriate cross section resembles a ring with a radius equal to the loop radius and yields a cross section of the form $4\pi r_i r_T$ where r_T is the interaction distance between the trap and the dislocation line, as suggested by previous researchers[131]. Recent atomistic modeling efforts have made a compelling case for carbon vacancy complex traps, however, which fall into the later category. Here, an interaction cross section of πr_i^2 is more appropriate. The responsible agent remains uncertain, so we included both possibilities in our calculations for completeness. In either case, the trap density becomes the sole parameter determining all hop lengths.

The two-mode diffusion model is fairly straightforward, and merely involves adding an irradiation activated component to the diffusion coefficient. This approach augments the net diffusivity of the appropriate range of interstitial clusters above the thermal value $D_{i,th}$ according to

$$D_i = D_{i,th} + \frac{1}{2N}\frac{\nu_{DT}}{2}\lambda_i^2 \tag{6.4}$$

where λ_i is the mean hop length of a cluster with i members and ν_{DT} is the frequency of detrapping due to irradiation. The activation frequency for this mode assumes that half of all detrapping events result in glide to the next trap, while half end with the loop returning to its original trap causing no net displacement, hence an activation frequency of ${}^{\nu_{DT}}/_{2}$.

For the moment, this framework assumes that the overall dimensionality of motion, N, remains three dimensional. Although individual hops clearly follow one dimensional trajectories, it is not clear that the overall motion is strictly one dimensional as cascades may also result in changes of Burgers vector. Indeed, the ultimate paths of clusters in a trap dominated medium may more closely resemble the mixed 1D-3D migration patterns observed for tetra-interstitials than those of crowdions in a pure metal. Regardless, one dimensional trajectories are probably more realistic, particularly for small clusters with long hop distances. Realizing a one dimensional diffusion, however, requires invasive modification of the reaction kinetics in addition to the diffusion coefficients, and will be introduced here.

The two-state model splits interstitial clusters into trapped and free states. The free state migrates at an activation barrier consistent with MD simulations, while the trapped state takes on the higher activation energy found in experiments. Additional kinetics must be implemented to allow a loop in a trapped state to transition to a free state and vice versa. The transition of loops from trapped to free states is analogous to dissociation events, with a rate constant equal to the detrapping frequency. Trapping events, on the other hand, resemble a reaction event. Unfortunately, the reaction rates constructed in Chapter 3 cannot describe this reaction, due to the plainly one dimensional nature of glide from trap to trap.

The concentration profile of free loops within a glide cylinder obeys the Poisson[1]equation along one dimension and falls to zero at a spacing of λ_i. Equating the total population in this profile to the bulk concentration of free loops gives a system of equations for $n_i(x)$

$$\begin{gathered}\frac{\partial^2 n_i(x)}{\partial x^2} = a_0 \\ \int_0^\lambda n_i(x)\mathrm{d}x = C_i \\ n_i(0) = n_i(\lambda) = 0\end{gathered}$$

where a_0 is a constant. Following the procedure presented in Chapter 3, the flux into each trap is integrated over the trapping cross section to determine a trapping rate of

$$k^+_{i,T}\rho_T = \frac{12 D_i \sigma_{i,T}\rho_T}{\lambda_i} = \frac{12 D_i}{\lambda_i^2} \tag{6.5}$$

which agrees with the suggested solutions of other researchers for similar geometries[28]. The dimensionality of free loop diffusion and the associated reaction rates remain three-dimensional for the same reasons as in the two-mode approach[2].

Employing the extra set of states complicates the reaction network. Any reaction product within the two-state region could potentially fall into either category. This distinction is not arbitrary, and the choice of state for reaction products impacts the kinetics of the entire reaction network. The methodology employed for state selection is as follows: if either parent cluster exists in a trapped state the daughter does as well. If both parents are in free states, the daughter is as well. Outside of the two-state region, all clusters are treated as free clusters for such purposes.

Each model has inherent advantages and limitations. The two-state model allows cascade damage to react or reach sinks before trapping where appropriate, if source terms are applied to the free state, whereas the two-mode model does not clearly accommodate prompt reaction. Additionally, some assumptions embedded in the two-mode model are not universally valid. The transport of loops between traps slows at sufficiently low temperatures, for example, reducing effective diffusivity. Furthermore, the two-mode model does not explicitly address any reactions with other defects which may occur during detrapping events that

---

[1] The only solution to the Laplace is trivial, $n(x) = 0$. Instead, an implicit continuum source of loops in the glide cylinder increment must be assumed to arise from such effects as detrapping and system interaction to employ a primitive cell approach. This informs the use of the Poisson equation.

[2] Note that the trapping rate and reaction rates are addressed with different assumptions about the dimensionality of diffusion. This discrepancy will be resolved with a more robust approach later.

ultimately return the cluster to its original position. On the other hand, it promises reduced complexity and computational expense by requiring fewer equations and a smaller reaction matrix.

6.2 Effects of Trap Mediation Kinetics

The apparent discontinuity of defect motion suggests two additional kinetic pathways which have not yet been included in CD, prompt reaction of primary damage and hop dominated transport of interstitial clusters. We analyzed the impact of these trap mediation effects separately and together. A consistent parameterization of the trap mediated system was applied to all interstitial clusters with four or more members. In this light, mobility set i_A was used for the two-mode model and for trapped clusters in the two-state model while set i_D was used for free clusters.

Trap mediation requires a few additional parameters. Foremost among these is the trap density, approximations of which are complicated by uncertainty in the composition of the traps. Consequently, our estimates relied on observations of hop length rather than the material composition. Rigorous measurements of hop distances are not straightforward either, and vary within and between materials. For high purity iron these hops may be as long as hundreds of nm[15], but are shorter for more complex materials with average hop lengths under 10 nm[95, 132]. Trap concentrations of a few hundred ppm give hop lengths of this magnitude for small visible clusters under both trap cross section assumptions. Varying this parameter through a range of possible values tested the sensitivity of trap mediation models to such uncertainty. Other specifications were held fixed throughout, with a detrapping frequency of $\nu_{DT} = 0.05$ s^{-1} and a fourth nearest neighbor separation used for the trap interaction distance r_T where applicable.

6.2.1 Prompt Reaction of Cascade Debris

Within the framework of trap mediated reaction-diffusion kinetics, defects born in cascades are highly mobile and may react with other components of the system or annihilate before finding traps and becoming sessile loop nuclei. It is entirely possible that the over-nucleation catastrophes demonstrated in Chapter 5 are simply the result of neglecting these prompt interactions. We examined this possibility using the two-state trap mediation model with the detrapping rate set to zero. For trap mediated cluster sizes, source terms were applied to the free state using the aged cascade database at 300 K.

When performing two-state calculations, the size of the reaction matrix significantly increased with the addition of new equations. In order to minimize this, free states were not included for interstitial clusters of all sizes. Large free clusters were not expected in these simulations because they could not be generated in detrapping events. As such, truncating the two-state range did not introduce significant error, but significantly improved computational performance. Figure 6.3 shows the observable defect development assuming interior traps at a variety of densities.

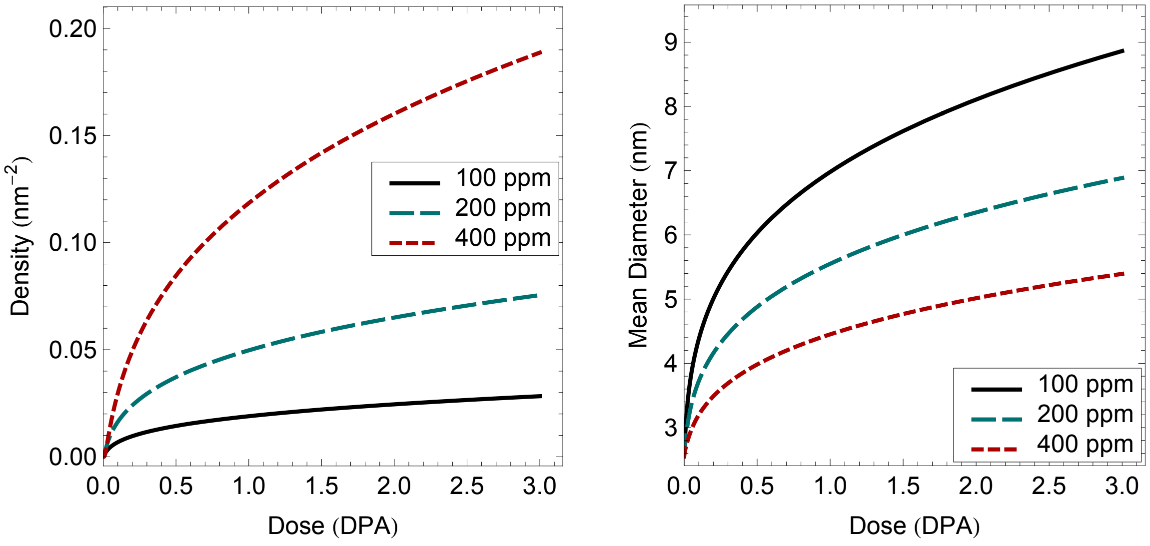

(a) Defect density

(b) Defect size

Figure 6.3: Evolution of cascade damage allowing prompt reactions at 300 K with a free state truncation at i_{80}

The additional mobility afforded to primary defects effected a clearly different damage profile compared from simple thermal activation. Mobility set i_A developed no visible loops within 3 dpa leaving an enormous supersaturation of sub-visible nuclei, whereas in the trap mediated model visible loops developed across a wide range of reasonable trap densities and exhibited noticable growth. An increased number of traps caused an increase in loop density concurrent with diminished growth rates. In all cases, the rate of growth was notably slower at the end of the simulation than near the beginning. The obvious downward concavity of loop density marked a singificant improvement, hinting at possible saturation, in comparison to simple thermal activation simulations where loop density increased linearly if loops grew to visible sizes at all.

To guarantee that truncating the extent of the free state was not impacting the system, we ran additional simulations with the truncation point at i_{800}. The additional order of magnitude of free states indicated a relative error of no more than 10^{-9} in the observed loop density and sizes. Using the i_{80} truncation point, we tested for saturation at a variety of other temperatures, as shown in Figure 6.4. Prompt reaction had notably less impact on temperature sensitivity. Similar to thermal activation, a saturation density was not reached except at the highest temperatures, and even then the loops were too numerous. Regardless, the slowing nucleation rates manifested as a lower loop density particularly for interior trap cross sections.

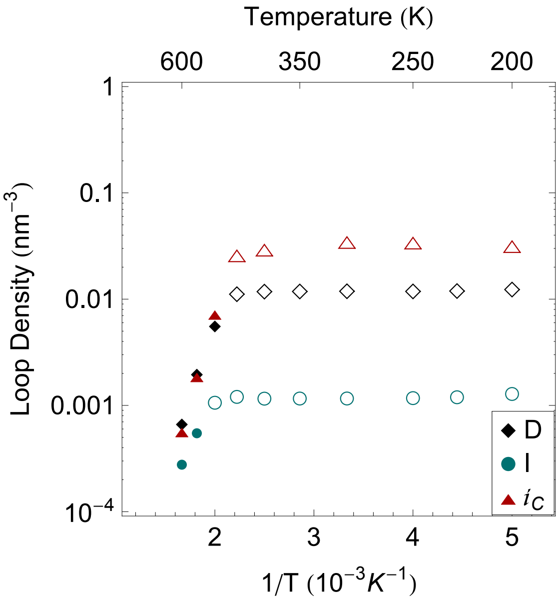

Figure 6.4: Temperature dependence of maximum loop density with prompt reactions at a trap density of 200 ppm. Interior (I) and dislocation line (D) trap location models are compared with the most mobile thermal activation set(i_C). Open points indicate that saturation was not evident by 10 dpa.

Despite some promising developments, the inclusion of prompt reactions was unable to reconcile our models with experiment. Even with interior trap locations - where the preference for prompt reactions is strongest - the system favored continuous nucleation. In observable effects, prompt reactions mimic the simple reduction of thermal barriers for some crowdion bundles, as in set i_C. Clear saturation in density still fails to occur at most temperatures, though the increase in population is somewhat mitigated. Defect densities still climb to unphysical levels at low temperatures, and the thermal dependence that emerges at high temperatures is still too strong. Lowering the trap density parameter several orders of magnitude could mitigate low temperature over-nucleation, but would not address thermal sensitivity, and higher temperature defect densities would plummet as well. Prompt reactions alone fail to resolve the dilemma raised in the previous chapter.

6.2.2 Detrapping with Cascade Damage

Discounting prompt reaction as the driver for loop saturation, detrapping remains as a potential solution. Using both the two-state and two-mode trap mediation approaches, we analyzed the effects of detrapping on long term loop development in CD models. Given the success of the truncation point approach to limit the number of equations in previous simulations, a similar tactic was adopted here. In this case, clusters past the truncation point were treated with the two-mode model. Again, source terms were applied to free cluster states where appropriate and interior traps were assumed to determine trapping cross sections. The impact of detrapping followed the trends demonstrated in Figure 6.5 when interior traps were assumed.

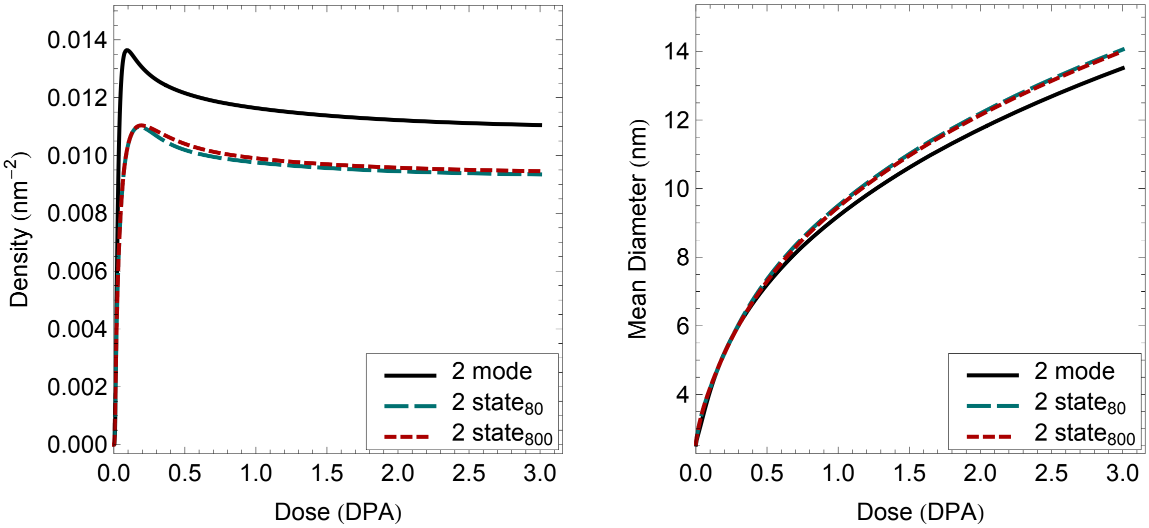

(a) Defect density

(b) Defect size

Figure 6.5: Evolution of cascade damage with detrapping effects at 300 K with a trap density of 200 ppm. The two-mode model is compared to the two-state model using two different truncation points

Under both models of detrapping kinetics, the damage density peaked quickly and subsequently declined for the remainer of the simulation. The rate of loop loss continually slowed, as the density appeared to approach a steady state value. The peak and apparent equilibrium density in the two-mode approach exceeded those of the two-state simulations. Loop growth progressed more quickly with detrapping effects, with the final size nearly double that of simulations that ignore hopping. The trend of decreasing growth rate with dose, however, was still apparent. A near, but not quite perfect, agreement in loop size and density was apparent between various truncation points for the free cluster states.

If traps acted on the dislocation line rather than from the loop interior, the saturation behavior changed, as shown in Figure 6.6. Though the same progression occurred - a peak density followed by decline - the peak was notably sharper and the reduction in population was more pronounced. Where only a small percentage of the loops were lost in an interior trapping model, more than half vanish with a dislocation trapping model. Loop growth is not affected as strongly, with only a small reduction apparent in final size. The difference in size manifests early in the simulations, when the loop density is highest, and remains mainly constant for the remainer. The two trap mediation approaches produced fewer observable differences with dislocation traps.

In addition to limiting the defect density, including hops significantly reduced temperature dependence. Figure 6.7(a) shows the insensitivity of peak loop density to temperature

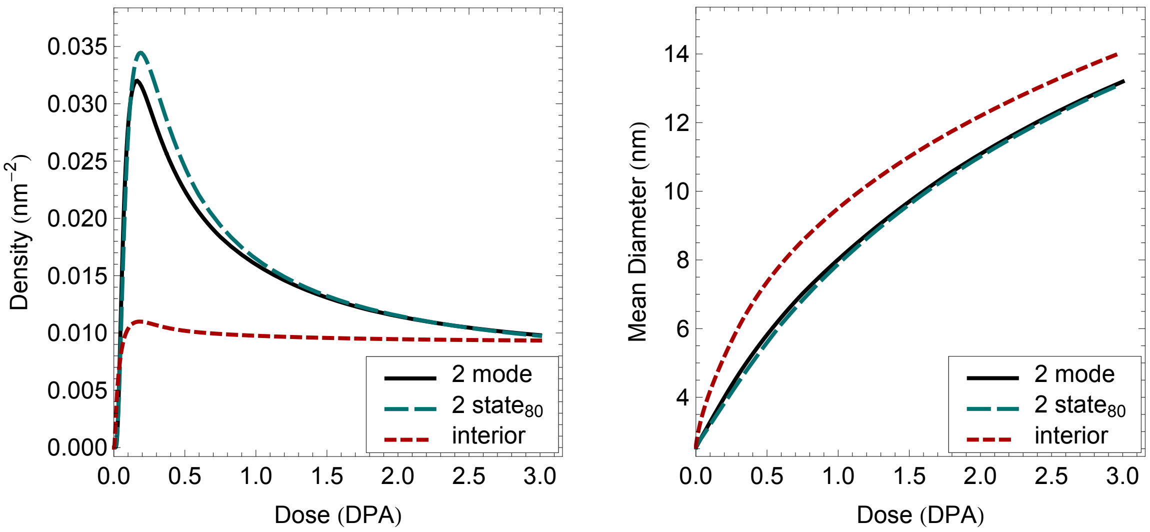

(a) Defect density

(b) Defect size

Figure 6.6: Effect of loop interior or dislocation line trap locations on defect development at 300 K with a trap density of 200 ppm. Both models are shown for dislocation trapping, while only the two-state model is shown for interior trapping.

for both types of possible trap. Interior trapping resulted in greater variation, still within a factor of two over the range of temperatures analyzed. As in the thermal activation scenario, vacancy mobility did not greatly impact saturation magnitudes, with some small deviations observed at higher temperatures. The trapping cross sections played a larger role, with different assumptions separating the peak damages by a factor of two to three, through the rapid loss of damage seen with dislocation cross sections mitigates this effect past peak damage.

Loop density depended on trap density instead. Peak damage density followed a predominantly linear dependence on trap concentrations. A higher order scaling emerged at low densities, suggesting that a different mechanism controlled loop density at high and low concentrations. The non-linear region emerged at similar densities in strictly two-mode simulations, suggesting that prompt reaction is not responsible for limiting the density in either region.

Hops impact the system evolution primarily by providing a drive toward saturation and the eventual loss of loops. From a nucleation perspective, the cascade damage that served a continuously increasing density of stable nuclei in a simple thermal activation approach are no longer stable. Transport to surfaces and other defects through hops limits the density of sub-visible, cascade-implanted interstitial clusters. As these nuclei grow to visible size, their number remains limited. Visible loops are also subject to transport. Annihilation at free surfaces, absorption of vacancies to shrink to sub-visible sizes, or absorption at sinks explains the declining loop population at later doses, in combination with any possible loop coalescence.

As trap density changes, the mechanism controlling the nucleation density changes as

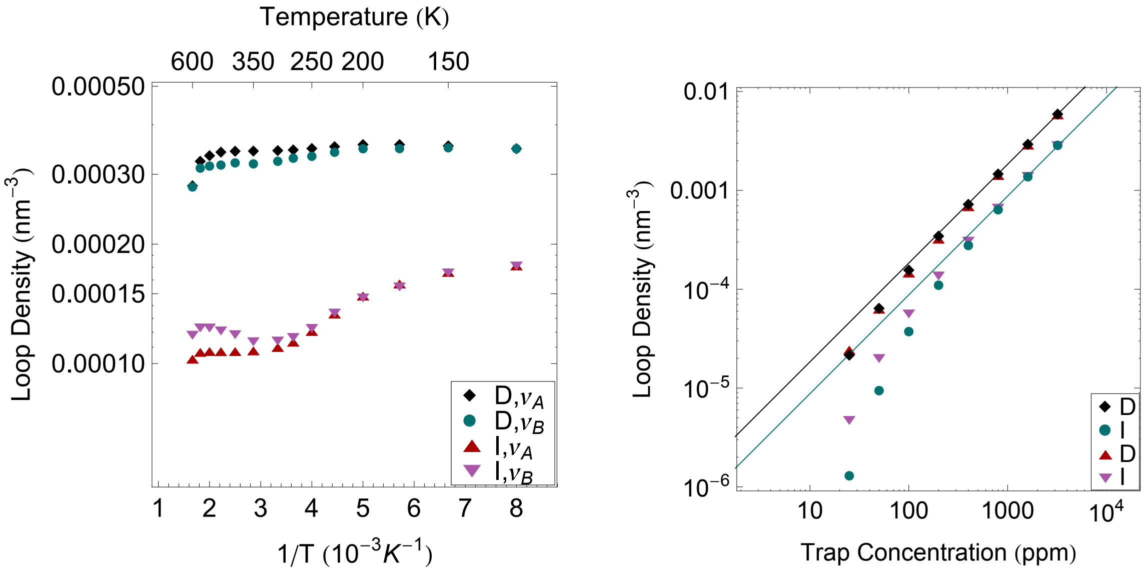

(a) Saturation at 200 ppm trap concentration

(b) Saturation at 300 K with linear fits

Figure 6.7: Dependence of the saturation density on temperature and trap density with detrapping effects. Dislocation line (D) and interior (I) trapping systems are both shown.

well. At high densities primary damage is absorbed primarily on other clusters, analogous to the recombination dominated scenario familiar from traditional rate theory models. At an equilibrium density, the source rate of nuclei is equal to loss on other loops, which is quadratic in defect concentration. In a rough approximation of the full reaction network, $g \propto DC_{eq}^2$ and $D \propto \lambda^2 \propto \rho_T^{-2}$, such that peak damage scales linearly with trap density as $C \propto \rho_T \sqrt{g}$. As the trap density falls and fewer defects are retained, such that sinks control the defect density instead. In the sink dominated case, $g \propto DC_{eq}$ suggesting that loop density should scale quadratically with traps, explaining the deviation from linear behavior observed in CD models at low densities.

The effects of different trapping cross sections also logically follow from their contribution to interstitial cluster mobility. When traps act on dislocation lines, small cluster cross sections are larger than for interior traps resulting in lower nuclei mobility and hence a higher nucleation density. As those clusters grow, the hop length falls off more slowly with a cross section that scales as ${}^1/_r$ rather than ${}^1/_{r^2}$. A greater fraction of loops continue to escape or react after reaching visible sizes, exacerbating density decline. The other notable cross section effect is a decrease in the importance of prompt reactions with line based traps, as evidenced by the closer agreement between two-mode and two-state simulations. This effect also stems from the larger cross sections assigned to cascade born clusters, which decreases the importance of prompt reaction.

Cross section effects are a minor factor, however, alongside the inclusion of hops which enables saturation and loss in the first place. Hopping also overrides any contributions of prompt reaction kinetics in this system. Including or excluding the initial mobility of cascade born defects in the thermal case resulted in only slight changes to the saturation density with almost no contribution to loop growth. Considering the prompt mobility of clusters separately from the irradiation activated motions had little impact as well. In fact, the surprisingly close agreement between the two models generally and simulations with different truncation ranges suggests that the two approaches are roughly physically equivalent, even though they act on the reaction-diffusion system in very different ways. One model introduces direct boosts to diffusivity with an implicit change to the reaction system only through resultant rate coefficient increases. The other establishes a secondary reaction system, with implied changes to net diffusivity arising from the trapping and detrapping rates. The agreement between the two, therefore, provides additional confidence in the internal consistency of the reaction-diffusion system and the physical meaningfulness of both models.

Inherent uncertainties plague experimental determinations of defect density, complicating any direct comparison with modeling predictions. At any time, some fraction of the loops in a material are excluded due to visibility criteria. Additionally, identifying damage features on a micrograph requires some degree of human judgment, as most are not fully or clearly resolved. Ferritic and martensitic materials display complex microstructures even before irradiation, which complicates loop counting even further, particularly in commercial alloys. Finally, defects are measured by areal density which is inhently sensitive to foil thickness, a factor that is often imprecise, variable over the counted area, or both. Modeling compliments this uncertainty with the trap density, which is very much unknown and can easily be treated as a fitting parameter to achieve any density desired. Caveats aside, experimental estimates and modeling calculations yield roughly similar saturation densities, on the order of 10^{-3} to $10^{-2}\mathrm{nm}^{-2}$

One assumes that that the errors in loop counting are systematic. Comparisons of relative density with respect to either dose or temperature, therefore, remain highly informative. In this regard, the trend of peak damage followed by slow decline aligns with experimental observations, particularly in the case of interior cross sections. It is more difficult to reconcile the more intense loop loss evident with dislocation line traps. The measurements of Kaoumi initially presented in Figure 2.1 demonstrate a saturation dose below half a dpa, in good agreement with our models. Furthermore, the elimination of strong temperature dependence brings our models much closer to experimental trends. The mild variation left by interior cross sections mimics experimental conditions, where loop densities are 2 to 5 times higher at lower temperatures. In this light, hop driven kinetics offer a clear resolution to the thermal dependence conundrum.

Crucial flaws remain between our model calculations and empirical data. Loops grow rapidly under the detrapping model, while the in-situ experiments indicate a much more modest trend. As with density, the experimental measurement of loop size contains some systematic errors. Again, human judgment and visibility hamper precise measurements of image size. Furthermore, the image size of a defect may not exactly match its physical size. The growth rate, however, should remain largely immune to such problems. Kaoumi and Topbasi both observe a significantly slower rate of growth when compared to our models. Potential sources of such errors, including reaction geometries and assumptions about defect dimensionality, are discussed in Chapter 7.

6.2.3 Detrapping with Frenkel Pair Damage

Including loop hops in CD models improves performance, creating a reasonable saturation of visible dislocation loops under cascade damage conditions which did not exist otherwise. In contrast, Frenkel pair damage did allow for the formation of loops at realistic densities in a simple thermal activation model alone. Hops occur under electron irradiation as well, though the activation mechanism is likely different. Regardless, including hop kinetics in the Frenkel pair damage context can serve as a test of the trap mediated diffusion framework. The explanatory power of this model could be undermined if detrapping compromises the development of loops under Frenkel pair damage conditions. On the other hand, the temperature dependence of thermal activation models remains irreconcilable with experiments, and including hop kinetics may close the gap.

The same detrapping frequency and trapping cross section assumptions used in cascade conditions were applied to Frenkel pair damage using a two-state model truncated at i_{80}. The effects on defect development are shown in Figures 6.8 and 6.9. Interestingly, many of the same trends evident in cascade conditions featured prominently with Frenkel pairs as well. Defect populations saturated quickly and proceeded to decline. Dislocation line traps produced higher peak densities and increased defect loss with only slight reductions in growth. The magnitude of loop density was similar to cascade conditions as well, and varied with trap density rather than temperature.

In contrast to cascade damage, strong thermal sensitivity was still evident at sufficiently high temperatures. The transition between a thermal and athermal region occurred regardless of trapping cross section, but was more pronounced with traps acting on dislocation lines. Under these conditions, the athermal saturation density was nearly constant. Trap density affected the athermal saturation density, but not the transition temperature to a thermally controlled loop density. A two region trend in loop density marked with a transition near 250 K is remarkably similar to the observations of Arakawa *et al*[129], who note such behavior in in-situ electron irradiations at each of two dose rates separated by an order of magnitude. In further agreement with our models, they also note a declining loop population past an early damage peak.

Prudence dictates some degree of caution when comparing these Frenkel pair models to electron irradiation experiments. In addition to all the concerns raised with heavy ion experiments, comparing to electron irradiation introduces a mismatched damage distribution with respect to depth. Furthermore, the estimates of hop frequency used in the modeling rely on a cascade based mechanism. As in the previous section, none of these errors compromise the validity of relative measurements. A relative decline in density with dose and a transition

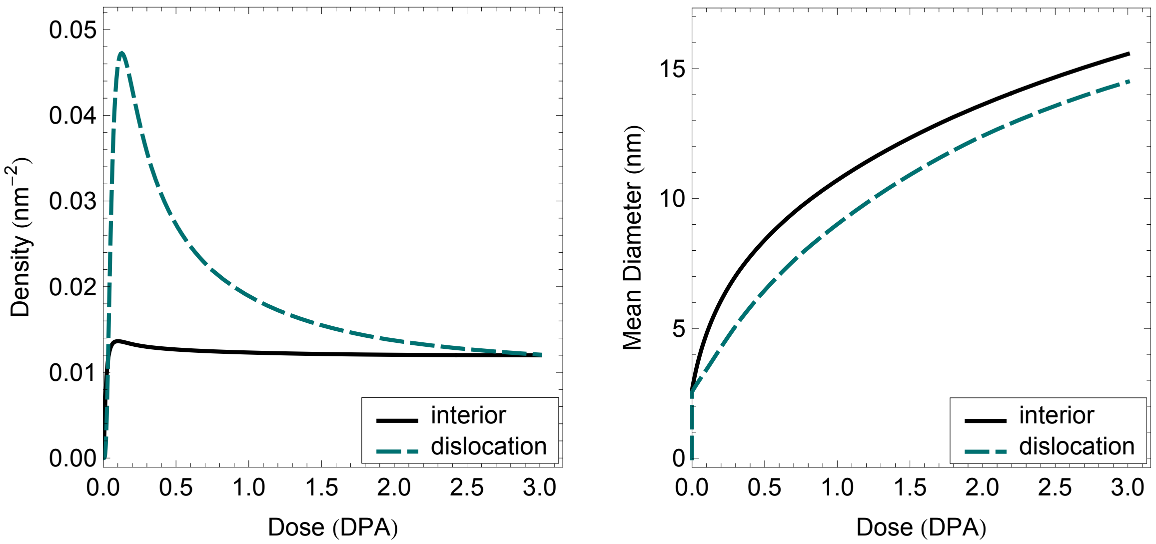

(a) Loop areal density

(b) Loop size

Figure 6.8: Loop saturation and growth at 200 K from Frenkel pair damage with a trap density of 200 ppm

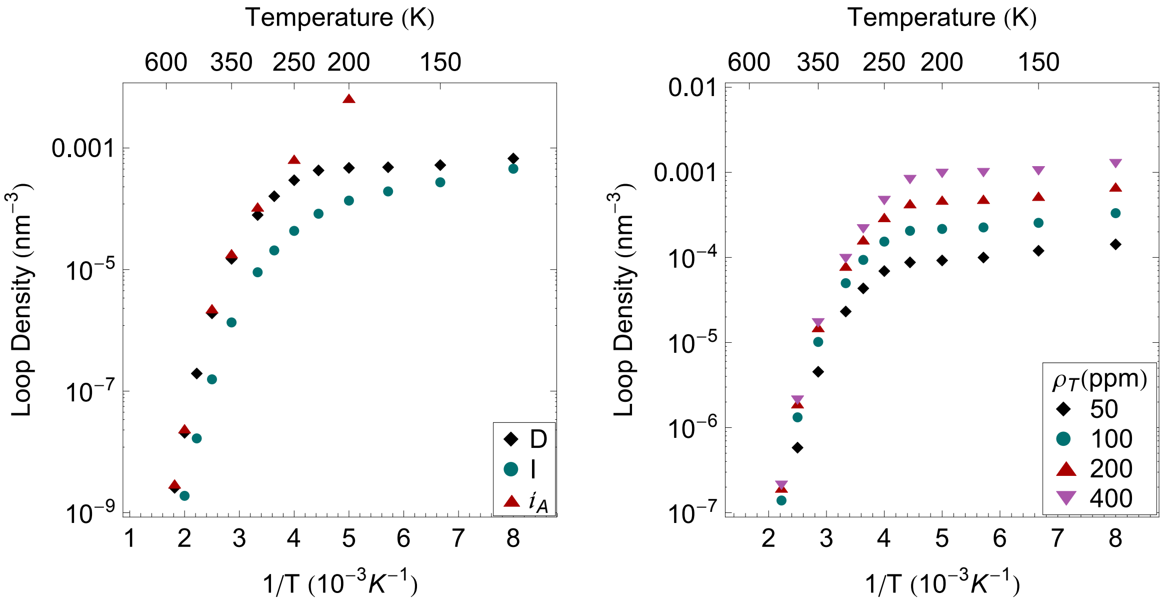

(a) Saturation at 200 ppm trap concentration

(b) Saturation at different trap densities acting on dislocation lines

Figure 6.9: Saturation density with detrapping effects for Frenkel pair damage. Dislocation line (D) and interior (I) trapping systems are both shown.

to athermal behavior - both evident in experiments - arise only when irradiation activated hops participate in defect diffusion and clustering. Trap mediation provides a means of explaining these experimental observations where thermal activation alone cannot, further highlighting its fundamental importance in clustering kinetics.

This chapter has made the case for irradiation activated transport of interstitial clusters between traps as a crucial driving force in defect cluster evolution in ferritic alloys. The models have incorporated the discrete hops evident under irradiation, providing a more comprehensive representation of the diffusion and interaction capabilities of interstitial clusters. Including this mechanism has incurred a number of pronounced changes in the course of defect evolution. A saturated density of loops developed regardless of temperature or primary damage conditions, in contrast to thermal kinetics. Additionally, the model has shown an emphatically decreased sensitivity to temperature up to 600 K in ion irradiation conditions and roughly 300 K in electron irradiation conditions. Both demonstrate a vastly improved agreement with experimental observations suggesting that trap mediation and irradiation activation, as presented, hold a fundamental role in the development of loops in these alloys.

Despite such improvements, the model remains imperfect. Hops introduced additional loop growth to the model, far out-pacing experiment. Indeed, the increased mobility of interstitial clusters leads to a growth process heavily influenced by the absorption of crowdion bundles in addition to monomer species. As discussed earlier, these clusters do not satisfy many of the assumptions made by the reaction rates employed in these models. The next chapter attempts to accommodate two features of crowdion bundles and dislocation loops which are not currently included: one dimensional motion, and asymmetric reaction volumes.

Chapter 7

Reaction Kinetics

The previous chapter introduced trap mediated diffusion as a mechanism for the aggregation of interstitial defects into visible damage. Trap mediation accommodates the observed behavior of visible defects in a variety of experimental conditions, as well as the behavior indicated by molecular dynamics simulations. As a comprehensive description of the mobility of dislocation loops in iron, it is a logical extension of long standing models of dislocation glide in bcc metals. Though CD models based on the trap mediated paradigm agree with experiment in a qualitative sense, particularly with respect to density, the quantitative agreement is quite poor. The ubiquitous overestimation of loop size suggests that the kinetic assumptions built into our CD models require a re-examination, which serves as motivation for this chapter. The impacts of anisotropic reaction volumes and one dimensional diffusion are both considered in the mean field kinetic assumptions, and models employing them are compared against kinetic Monte Carlo simulations to establish their efficacy.

7.1 Non-spherical Reaction Geometries

A number of assumptions employed in constructing the reaction kinetics for common CD models indulge a highly liberal simplification of the real properties of defects discussed in Chapter 4. A precise treatment of the absorption of point defects by a collection of dislocation loops of arbitrary size is extremely difficult to realize in practice. The extent to which smaller interstitial clusters behave like dislocation loops remains unclear, and the cascade-born defect clusters which might interact with loops span a variety of sizes. Furthermore, the mobility of larger interstitial clusters introduces the possibility of loop coalescence events. Whatever the finer details may be, the reaction volumes for larger loops with clusters are certainly not isotropic.

Much as a cylindrical geometry approximates the capture characteristics of an infinite straight dislocation, a toroidal geometry roughly represents the absorption characteristics of a dislocation loop. Just as an infinite, straight, and isolated dislocation is unrealistic from the start, it might be argued that a perfectly circular, isolated loop equally oversimplifies the loop as a defect sink. As with network dislocations, the distinction between regions of spontaneous capture and drift driven by interaction energy is unclear, and complicated further by strain field anisotropies. Nonetheless, the torus has been used ubiquitously in CRT as a capture geometry for dislocation loops[133, 134]. Treating the loop as a torus fares no worse than treating the line dislocation as a cylinder, at least for the absoprtion of point defects on sufficiently large dislocation loops.

In a cascade damage paradigm, larger clusters are expected to play a significant role in the formation of visible features, loops and voids alike. Consequently, the steady state growth rate for loops hinges not just on the absorption rate of point defects, but of mobile vacancy clusters and small cascade-born crowdion bundles as well. These circumstances further strain the physical veracity of a toroidal reaction volume, even before considering strain field effects. Consider the extreme limit: two interacting interstitial clusters of similar size, sufficiently large to demand treatment as loops. Such coalescence events amount to more than a simple thought experiment, and even play a crucial role in the mechanism of $\langle 100\rangle$ loop formation advocated by Marian[85].

The interaction of small crowdion bundles with one another - both within cascade debris and later during long range diffusion - is a related phenomenon which promises to feature in damage evolution at low temperatures because the TEM visible defect clusters that develop are nominally aggregates of interstitial type defects. Due to the long range anisotropic strain fields generated by these clusters, the conditions under which they react are far from simple. Attractive and perhaps even repulsive interactions over ranges much larger than the cluster sizes themselves are conceivable, altering the reaction kinetics in a manner not unlike the dislocation bias of CRT models. A rigorous approach for handling these interactions remains elusive, aside from cumbersome atomistic methods. The 1D diffusion of crowdion bundles complicates the matter further, and will be discussed later. For the moment, we will retain the framework of a "mechanical contact" approach to determining reaction volumes, whcih informs the use of a torus even in these cases.

7.1.1 Defect Interaction with Dislocation Loops

Seeger and Gosele derive a solution for the flux into a torus and present an analytical expression for the sink strength as

$$S_L(r_L, r_p) = \frac{4\pi^2 r_L}{\log(8r_L/r_p)}\rho_L \tag{7.1}$$

where r_L is the loop radius and r_p is the defect capture "pipe" radius[133]. This is a simplification of the exact solution, and remains valid for $r_L \gtrsim r_p$. This expression has been adopted in past CD models to more accurately handle the flux of point defects to loops[42].

Cascade damage conditions demand caution in applying Eq. (7.1), due to the highly dissimilar properties of the mobile defect clusters the loops may be absorbing. Consequently, the pipe radius is not necessarily a property of the dislocation loop itself, but rather of the cluster the loop is interacting with. Vacancy clusters and crowdion bundles have a larger size than point defects, suggesting that the pipe radius for interaction increases as well. Using a pipe radius of the form $r_p = r_0 + r_j$ retains the framework of the isotropic reaction volume scaling of Eq. (4.1), where j is the absorbed species.

The reaction physics must account not just for the diffusion of point defects to trapped loops, but also for the diffusion of free loops to other defects. Consider the migration of a crowdion bundle to a larger void. A non-spherical geometry is involved, but the size of the spherically symmetric defect dominates. In a general form, the reaction rate must converge to Eq. (7.1) for large values of r_L/r_p, but to Eq. (3.9) - the spherical sink rate - in the opposing limit. The expression

$$\begin{aligned} k^+_{i,j} &= (D_i + D_j)\left((1-\alpha_{i,j})z^d_{i,j} + \alpha_{i,j}z^v_{i,j}\right) \\ \alpha_{i,j} &= \left(1 + \left(\frac{r_i}{3(r_j + r_0)}\right)^2\right)^{-1} \\ z^L_{i,j} &= \frac{4\pi^2 r_i}{\log(1 + 8r_i/(r_j + r_0))} \\ z^V_{i,j} &= 4\pi(r_i + r_j + r_0) \end{aligned} \tag{7.2}$$

satisfies all these constraints (as cast in the form of a rate constant instead of a sink strength) for a loop i interacting with some arbitrary cluster j. The function $\alpha_{i,j}$ can be thought of as determining how poorly the applicability condition $r_L \gtrsim r_p$ is met for the reaction in question. In z^L, the logarithm in Eq. (7.1) is slightly modified to prevent a negative singularity as $r_i/r_j \to 0$, and does not effect the solution where z^L contributes significantly to k^+. Consequently, the transition to loop-like absorption behavior is handled continuously, with no need for a strong distinction between interstitial clusters that behave like point defects and larger crowdion bundles which behave like loops.

Though Eq. (7.2) has a number of desirable properties, it still suppresses a great deal of atomic scale interaction characteristics, and likely performs particularly poorly with respect to handling interactions with other interstitial clusters. Loops and crowdion bundles are restricted to four possible $\langle 111 \rangle$ orientations. As a result, all possible trajectories of approach require an intersection of glide cylinders. A few select cases, shown in Figure 7.1 demonstrate how this impacts the reaction conditions of crowdion bundles. Two interstitial clusters with the same orientation have parallel glide cylinders. When the separation distance between the glide cylinder axes is much larger than the loop radii, any interaction between parallel clusters is clearly impossible. With decreasing separation distances, coalescence becomes more plausible. In the limiting case of coaxial glide cylinders, however, the strain fields between loops suggests repulsion, again rendering coalescence unlikely.

Non parallel glide cylinders present a more complex set of possibilities. As with a parallel configuration, the glide cylinders may or may not overlap. The cylinder axes for most potential interactions are skew, and a decreasing line to line distance results in a greater degree of overlap. In the case where the cylinder axes are coplanar, repulsion is not necessarily expected in contrast to the coaxial case. To the contrary, the dislocation lines can meet and form a junction in these cases, and the strain field interactions are less straightforward. Indeed, the Marian mechanism for ⟨100⟩ loop formation depends on precisely such a process.

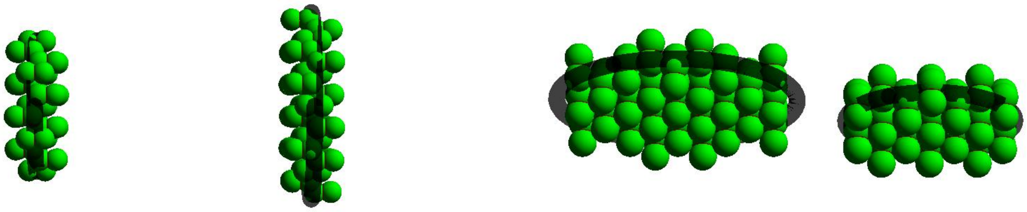

(a) Coaxial

(b) Parallel

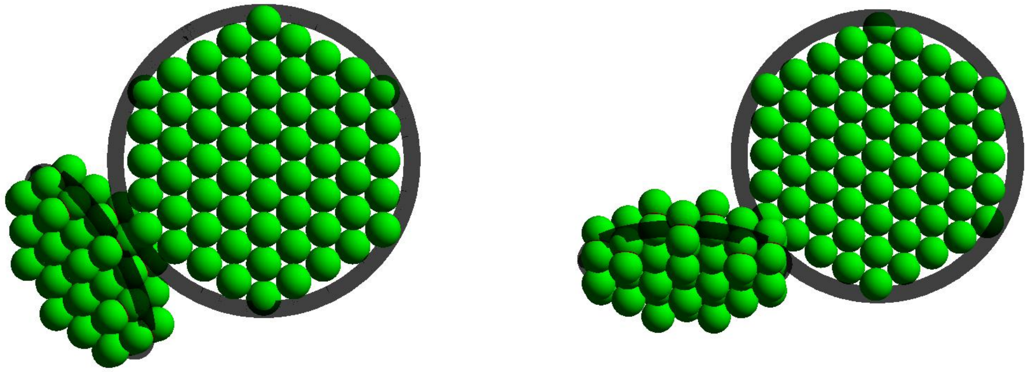

(c) Co-planar

(d) Skew

Figure 7.1: Interaction possibilities for dislocation loops described by the relative position of glide cylinder axes

Although some atomistic studies have demonstrated the coalescence of loops[135] the phenomenon is not well characterized, and it is not clear under which circumstances loops will react and under which they will not. Furthermore, the studies that do exist neglect any possibility that one loop is trapped, as is likely the case in a real material containing several to several hundred ppm impurities. As such, we consider a range of possibilities for constructing a loop reaction volume. One limiting case includes any loop positions that result in contact between the dislocation lines. This is the largest possible reaction volume, and precisely follows the form of z^L as presented in Eq. (7.2). This geometry is rather generous, even allowing the coalescence of two equally sized coaxial loops. A more restrictive approach allows coalescence only if a limited area of the interstitial clusters overlap. In such a case, the reaction volume has a radius of the combined radii of the coalescing loops such that

$$\begin{aligned} z^L_{i,j} &= \frac{4\pi^2(r_i + r_j)}{\log(1 + 8(r_i + r_j)/r_c)} \\ \alpha_{i,j} &= \left(1 + \left(\frac{(r_i + r_j)}{3r_c}\right)^2\right)^{-1} \end{aligned} \tag{7.3}$$

where r_c is the distance at which the dislocation lines react. A limiting case forbids coalescence entirely, specified by $r_c = 0$.

Comparing these approaches to one another allows an assessment of how crucially defect evolution hinges on the reaction volumes, and how carefully these effects need to be considered. For example, the reaction rates generated by the standard approach outlined in Chapter 3 exhibit several interesting and perhaps unintended properties arising from the different configurations of interstitial and vacancy clusters. The radii of these clusters are specified differently, such that a given interstitial cluster has a larger radius than a vacancy cluster with the same number of constituents. These size differences manifest as a bias in reaction rates in favor of interstitial clusters, however it is not clear whether this effect is real or merely an artifact of spherically symmetric simplification. Furthermore, it remains unclear whether this affects the formation and growth of visible damage features.

The modified loop reaction rates presented in this section indicate an opposing effect, particularly for large loops absorbing point defects. To indicate the magnitude of such a correction we introduce the notation $\beta_{loop} = k_{i,j}/k^{3D}_{i,j}$ where $k^{3D}_{i,j}$ is the isotropic reaction rate. In a case where the coalescence of loops is forbidden, β_{loop} is zero. Elsewhere the reductions are more complex, and vary based on the reacting species, as seen in Figure 7.2. In the case of simple defect absorption, the reaction rates can be reduced by as much as a third for large loops absorbing point defects with no reduction at all in the opposite limit. The coalescence calculations produce slightly more pronounced reductions in the rate of small interstitial cluster absorption by loops, and even larger reductions for the rates of reaction between large loops. In both cases the reaction rates are modified by no more than a factor of two.

7.1.2 Effects on Defect Evolution

Changing the reaction geometries may or may not induce changes in the calculated defect distributions, a possibility investigated using CD with a variety of assumptions. These calculations used reaction rates based on toroidal reaction geometries for all interstitial

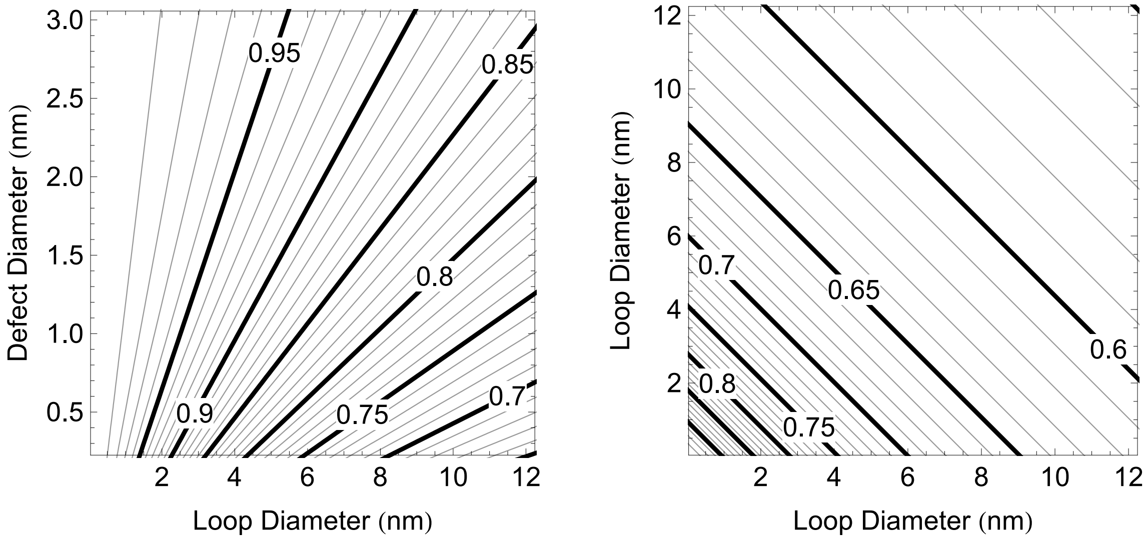

(a) Defect absorption Eq. (7.2)

(b) Loop coalescence Eq. (7.3)

Figure 7.2: Reduction in reaction rate magnitudes for dislocation loops, β_{loop}, for toroidal reaction geometries

clusters size four or larger. Construction of these rates followed one of three variations. In the first, Eq. (7.2) governed the rates for all defect clusters interacting with a loop, regardless of whether the other cluster was of vacancy or interstitial type. If both species were loops, the larger cluster was used to determine the loop radius, and the other to determine the pipe radius. The second variant instead used Eq. (7.3) if both species were loops with an interaction distance equivalent to the core radius. The final variant is identical to the second with the interaction radius set to zero, effectively forbidding any loop coalescence. These are summarized in Table 7.1.

	$(v_\infty - i_3) +$ $(v_\infty - i_3)$	$(v_\infty - i_3) +$ $(i_4 - i_\infty)$	$(i_4 - i_\infty) +$ $(i_4 - i_\infty)$	Comments
S_0	Eq. (3.9)	Eq. (3.9)	Eq. (3.9)	Isotropic geometries
L_1	Eq. (3.9)	Eq. (7.2)	Eq. (7.2)	Toroidal absorption geometry for loops
L_2	Eq. (3.9)	Eq. (7.2)	Eq. (7.3) $r_c = r_0$	Modified torus for coalescence
L_3	Eq. (3.9)	Eq. (7.2)	Eq. (7.3) $r_c = 0$	Toroidal absorption geometry for loops, no reactions between loops

Table 7.1: Approaches to account for non-spherical geometries of dislocation loops. A formula for the reaction rate constant is supplied for each of three scenarios, sphere-sphere sphere-loop and loop-loop reaction reactions

Using both trapping cross sections, CD calculations indicated similar loop densities regardless of the reaction volumes used as shown in Figure 7.3. The spherical reaction volume control case generated a slightly lower saturation density than toroidal variants for both trapping models, though the difference in final concentration was always within roughly ten percent. The effects of trapping cross section seen in the isotropic case were largely unperturbed by modifications of the reaction geometry. The only pronounced difference occurred when coalescence was forbidden completely (L_3), where the peak visible damage occurred with lower magnitude and at later doses, particularly with traps situated at dislocations. The unique behavior of even this case, however, did not persist past about 1 dpa.

Loop size proved more sensitive to assumptions of the reaction geometry. Modifying the reaction geometry for point defect absorption (L_1) only slightly reduced loop growth, with additional restrictions on the coalescence reactions (L_2) providing additional damping to growth. The impact of the two modifications reversed in magnitude based on trapping cross section, with point defect absorption playing a more significant role with interior trapping and a smaller one otherwise. Completely forbidding loop coalescence drastically hampered loop growth in either case, producing roughly half the growth rate - both prompt and long term - compared to the control case. With traps situated on dislocation lines, the prompt growth was damped enough to delay the appearance of visible damage.

The effects on defect evolution are quite modest, certainly not producing any of the substantial effects that defect mobility had in the previous chapter. None of these approaches deliver the reduction in the growth rate required to bring the model in line with experimental observations, except perhaps for the highly unphysical limiting case where reactions between crowdion bundles were completely forbidden. Furthermore, the assumptions underlying these reaction kinetics remain largely unsatisfying. Without any consideration for the one dimensional diffusion of interstitial clusters, the interaction rates of crowdion bundles with one another or stationary vacancy clusters remain poorly constructed. Resolving this inconsistency is addressed in the next section.

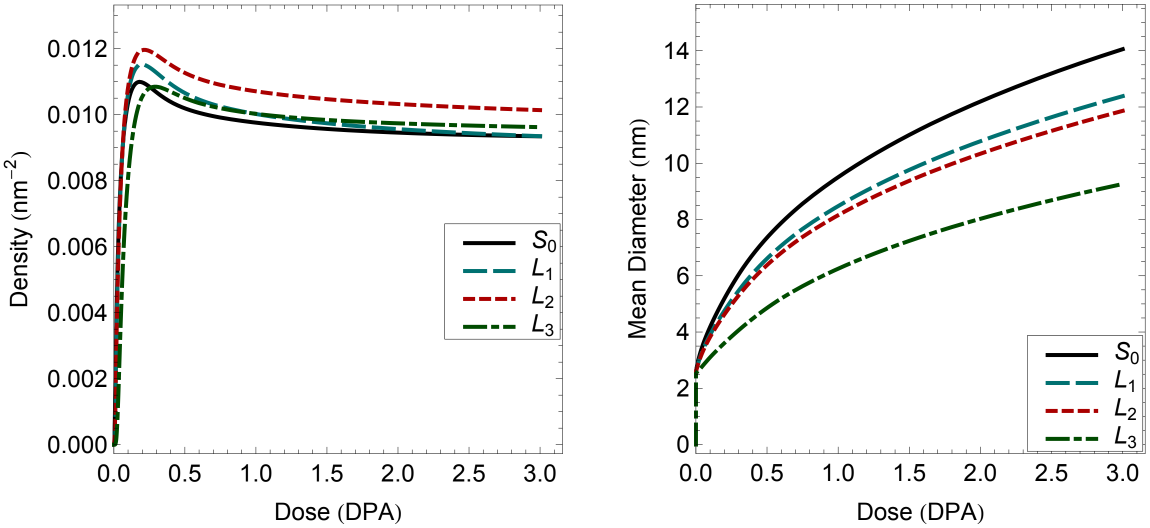

(a) Visible defect density with interior trapping

(b) Average size with interior trapping

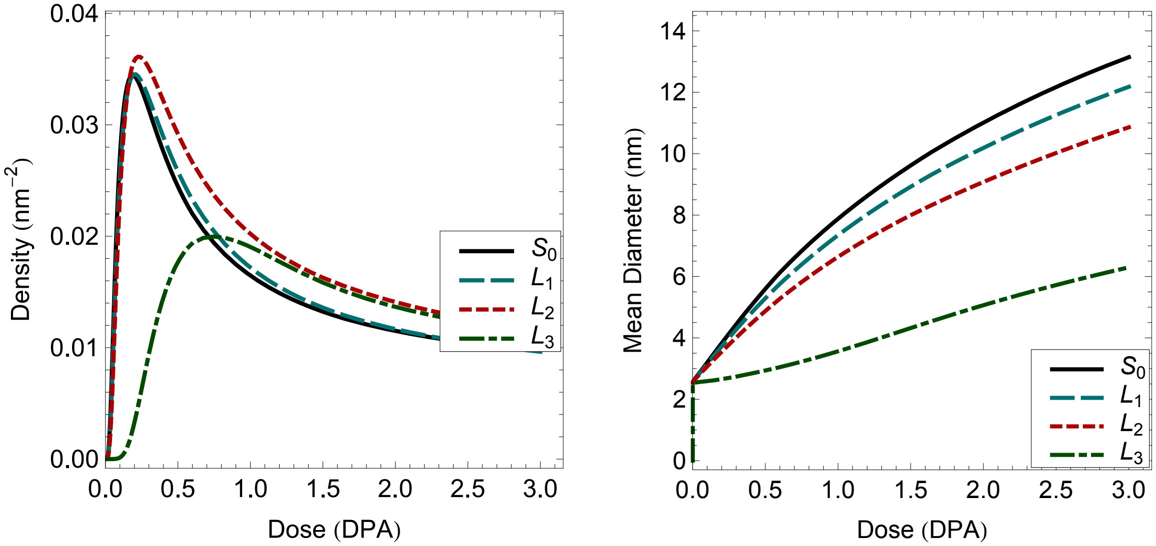

(c) Visible defect density with dislocation trapping

(d) Average size with dislocation trapping

Figure 7.3: The impact of dislocation loop reaction geometry on visible defect development. The areal density and mean size for are compared across the systems outlined in 7.1 for the influence of traps situated at dislocation lines or loop interiors.

7.2 One Dimensional Diffusion

Past studies have investigated the changes in sink strength that arise from anisotropic diffusion[136–140]. These demonstrate significantly lower rates for absorbing 1D diffusers than 3D diffusers, particularly when the sink density is low. In this literature, a great deal of attention has been afforded to the impact of occasional direction changes or transverse migration, and the impact this has on defect absorption at voids. Consequently, a semi-empirical "master curve" expression developed within this literature describes the sink strength of voids over a wide range of mixed-dimensional defect behavior. This expression is difficult to cast in a reaction rate form suitable for implementation in CD models. Furthermore, the applicability of this expression to a non void-dominated environment is questionable. The trap dominated medium required to stabilize interstitial clusters unseats the assumptions made to produce the master curve, rendering its complexity both unwarranted and unnecessary.

In order to generate rate coefficients appropriate for the trap mediated diffusion environment, it is important to consider the separation of timescales in the problem. Due to the very fast 1D glide of interstitial clusters even at low temperature, they interact with other point defects in the system by two very different kinetic pathways. The defects either thermally diffuse to the interstitial cluster while it is trapped, or are swept up by the interstitial cluster in the process of rapid glide during a hop. Similarly, interstitial clusters interact with one another when a free cluster glides to a trapped cluster along an appropriate approach trajectory. The high diffusivity of these clusters during glide segments renders the probability of two free loops encountering each other negligible, except during the annealing stage of a cascade. In all cases, one reaction partner is effectively immobile with respect to the other. In this context, the rate of reaction has two distinct contributions such that,

$$k^+_{i,j} = k^+_{i\to j} + k^+_{j\to i} \tag{7.4}$$

which can be calculated separately. As in the three dimensional diffusion case, the reaction network for a trap mediated diffusion system can be constructed by introducing multi-mode diffusion or additional equations to describe separate cluster states.

7.2.1 Impact on Reaction Rates

In the two-mode diffusion approach, trapped and free clusters lack any distinction and the reaction rates should be calculated accordingly. The migration mechanism of interstitial clusters consists of rapid hops spanning distances much larger than the lattice spacing separated by long timescales comparable to the rate at which damage is introduced. For any interaction for which these hops are the dominant kinetic pathway such as the migration of interstitial clusters to stationary vacancy clusters, no long range concentration profiles are established. The rate of reaction is thus determined by the activation frequency for hopping, with any defects distributed between traps in a given interstitial cluster's glide cylinder swept up during the course of a hop. Consequently, these motions express a reaction-limited rather than diffusion-limited interaction, specifically one governed by

$$k_{i\to j} = \frac{\nu_i}{2}\sigma_{i,j}\lambda_{i,T} \tag{7.5}$$

where $\sigma_{i,j}$ is the cross section for reaction between species i and j and will be discussed in more detail later. The nominal rate for detrapping by cascades is divided by 2 for consistency with the formulation of the diffusion coefficient in the two-mode model (see eq 6.4).

A number of objections could naturally be raised to such an approach. As in the the three dimensional transport case, there is no guarantee that clusters generated as primary damage will be properly described by these kinetics, as they are designed to represent clusters moving between discrete traps. Secondly, this approach assumes that other defects are uniformly distributed about the interstitial cluster when it hops. Lastly, the properties of a given cluster may change over the course of a single hop as a result of defect absorption, particularly for small clusters which may even shrink to three dimensional diffusers by way of vacancy absorption. It is not clear *a priori* that any of these assumptions are satisfactorily addressed in the reaction limited formalism implemented here. A description of trap mediation as a two-state system is less vulnerable to these concerns.

The two-state model promises additional rigor, but requires a more complex analysis. Distinctions are made between the states, and the free state requires diffusion limited rates to describe not only trapping interactions, but reaction with other clusters as well. As with previous approaches to this complex topic, we invoke the effective medium approach described by Eq. (2.6). When applied to the one dimensional case, this approach returns an inward flux of defects i at sink j of the form

$$I_{in} = 2D_i\sigma_{i,j}C_i\sum_j \sigma_{i,j}C_j \tag{7.6}$$

where $\sigma_{i,j}$ is the interaction cross section between i and j and the quantity $\sum\sigma_{i,j}C_j$ is equivalent to λ_i^{-1}, the inverse mean free path for cluster i. The reaction rate coefficient follows as

$$k^+_{i\to j} = \frac{2D_i\sigma_{i,j}}{\lambda_i}. \tag{7.7}$$

which is equivalent to the derivation by Woo[136] for pure one dimensional diffusion. We note briefly that an alternative derivation is provided by Borodin which follows a more complex method but returns the same result[137].

The 1D rate coefficient can be applied to the interaction of one dimensional diffusers with traps in addition to all other defects in the system. All of these interactions should be considered when determining the mean free path. This contrasts with the approach taken in the previous chapter where the one dimensional nature of diffusion was accounted for only in trapping reactions. Interestingly, the trapping rate derived in that case using a primitive cell model (implying equally spaced traps) differs from the effective medium approach by a factor of six. The approach here treats arrival at other defects identically to arrival at traps, and both obstacles as randomly arranged in the mean field. Unfortunately, the use of Eq. (7.7) causes the coefficient matrix k^+ to vary slowly with the defect concentration. The additional cost associated with this is minimal, as only λ changes, resulting in only one additional operation at each time step.

7.2.2 Cross Sections

The cross section for reaction figures prominently in either model. For a gliding cluster i, all locations for cluster j that lie within a reaction volume for the two species form the cross section when projected onto a plane perpendicular to the glide direction. Posing the problem in these terms generates simple expressions for a select few reactant pairs. For example, a large void absorbing much smaller crowdion bundles has a circular cross section with a radius slightly larger than the void radius. In the opposing limit, the cross section for a large gliding loop absorbing point defects is a ring with a thickness of twice the dislocation capture radius. Yet again, we find that the interaction between interstitial clusters presents a greater challenge.

The simplest approach to estimating the cross sections for loop coalescence follows the logic of the cross section for void interaction. In this approach, interstitial clusters might be said to interact whenever any of their constituents overlap spatially. In general, the habit planes of the two clusters may be coincident - giving a spherical cross section - or inclined, resulting in an elliptical cross section as illustrated in Figure 7.4(c). Though straightforward, such a construction contains a number of intuitively obvious flaws. As discussed earlier, the strain fields of two loops with coaxial glide cylinders suggest a strong repulsion. Glide toward one another in this scenario would be forbidden, suggesting an entirely different cross section. Instead, consider reaction volumes of L_2 of the previous section which allows spontaneous reaction only when dislocation cores overlap. This results in a set of annular cross sections, as illustrated in Figure 7.4(d).

For the interaction of loop i with an arbitrary spherical cluster j, the cross section can be constructed from

$$\sigma_{i,j} = \begin{cases} 4\pi r_c \left(r_j + r_c\right) & r_i > r_j + r_d \\ \pi \left(r_i + r_j + r_c\right)^2 & r_i \leq r_j + r_c \end{cases} \tag{7.8}$$

which is applicable for the scenarios of Figures 7.4(a) and 7.4(b). For a loop which occupies a habit plane perpendicular to its glide direction, the cross section based on a defect agglomeration paradigm follows

$$\sigma_{i,j} = \frac{\pi}{4}\left(r_i + r_j\right)^2 + \frac{3\pi}{4}\left(r_i + r_j\right)\left(r_i + r_j/3\right) \tag{7.9}$$

for $\langle 111\rangle$ loops, where the first term accounts for encountering loops in the same glide direction and the second term accounts for loops in other orientations. Loop coalescence based on dislocation interaction is described by a similar expression,

$$\sigma_{i,j} = \frac{\pi}{4}\left(a_+^2 - a_-^2\right) + \frac{3\pi}{4}\left(a_+ b_+ - a_- b_-\right) \tag{7.10}$$

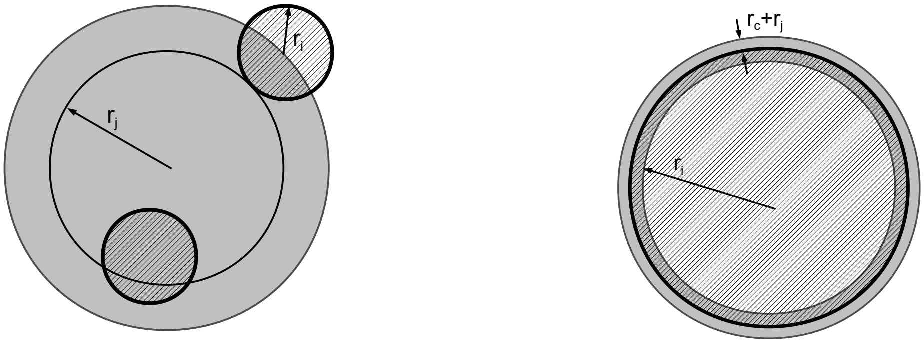

(a) Void

(b) Point defects

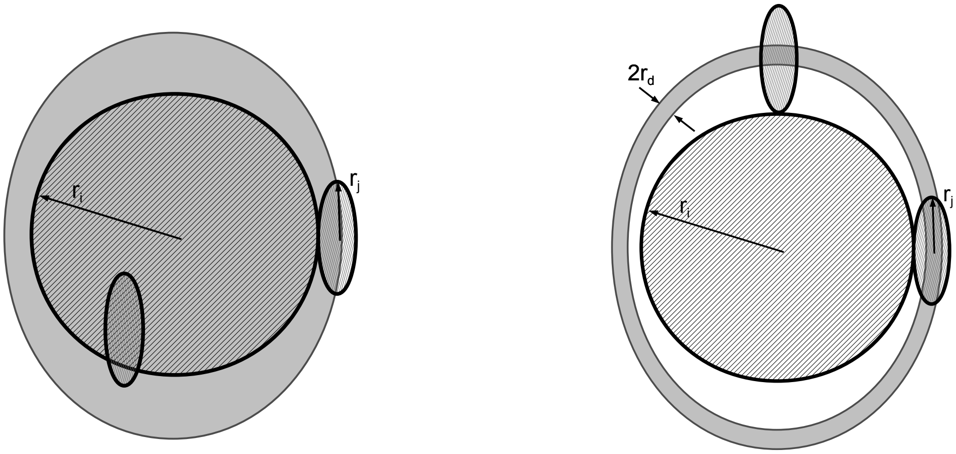

(c) Loop-loop with a cluster agglomeration basis

(d) Loop-loop with a dislocation interaction basis

Figure 7.4: Cross section for crowdion bundle reaction with other defects and defect clusters. Cross sections are shown in grey, with examples of relative positions of defects superimposed. Crowdion bundles (loops) are shown hatched.

where

$$a_+ = r_i + r_j + r_d \qquad a_- = \max(r_i + r_j - r_d, 0)$$
$$b_+ = r_i + r_j/3 + r_d \qquad b_- = \max(r_i + r_j/3 - r_d, 0)$$

and r_d is the line to line distance between dislocations that results in a reaction between them, analogous to r_c in the three dimensional reaction kinetics in Eq. (7.3).

The real physical significance of r_d is somewhat convoluted, as the assumption that loops will spontaneously coalesce whenever their dislocations overlap in the manner suggested - and only in those conditions - is quite strong to begin with. While it useful in establishing an appropriate scaling of the interaction rates with loop size, particularly in the limit of small cascade-born crowdion bundles diffusing to much larger dislocation loops, these cross sections should not be taken to be strictly physical as posed. There is no guarantee that r_d is constant (or even non-zero) throughout, that it is identical for loops with similar as opposed to dissimilar glide directions, or that it is independent of reacting loop sizes. The few atomistic calculations that have been performed on the subject even indicate a range of potential outcomes for identical interaction conditions[135]. Instead, r_d should be viewed as an effective average interaction distance which establishes a linear relationship between the reaction probability of two loops and their combined line length.

In any case, the reaction rates for loop-loop interactions are significantly reduced in comparison to similarly sized 3D diffusers. As with the loop geometry, the impact of one dimensional diffusion can be measured by the unitless quantities $\beta_{1D} = k^{1D}_{i,j}/k^{3D}_{i,j}$. Values of β_{1D} are shown for the full phase space of loop-defect interactions in Figure 7.5 with a trap concentration of 200 ppm. Owing to the potential change in reaction rates in the two-state model with defect concentration, the reaction limit based two-mode approach of Eq. (7.5) is used in illustrating the trends in β_{1D}. Additionally, changes in the trap concentration impact the magnitude of the 1D reaction network, even in the reaction limited case.

Overall, the reductions in reaction rates as a consequence of one dimensional diffusion are much larger than those arising from changes in the reaction geometry. As a consequence, the steady state concentration of crowdion bundles in the system will likely be a good deal higher. It is the partition of primary damage species between clusters of different types, however, that ultimately determines the microstructural evolution. Thus, the more pronounced size dependence of β_{1D} as compared to β_{loop} is of greater importance than the difference in magnitude. β_{1D} for collisions with vacancy clusters from Eq. (7.8) is almost purely a function of the size of the 1D diffuser. Unsurprisingly, in the case of reactions between two 1D diffusers the size of both becomes important. Note that for a one dimensional diffuser of a particular size (a vertical line on these plots) the most drastic reduction is for reaction with small loops. Additionally, for these the parameters chosen here, β_{1D} for small crowdion bundles is nearly identical for loops and voids. The magnitude of the loop-loop interaction rate, however, is linearly proportional to the coalescence distance r_d, and consequently we expect the partition of crowdion bundles between interstitial and vacancy clusters to be highly sensitive to this parameter.

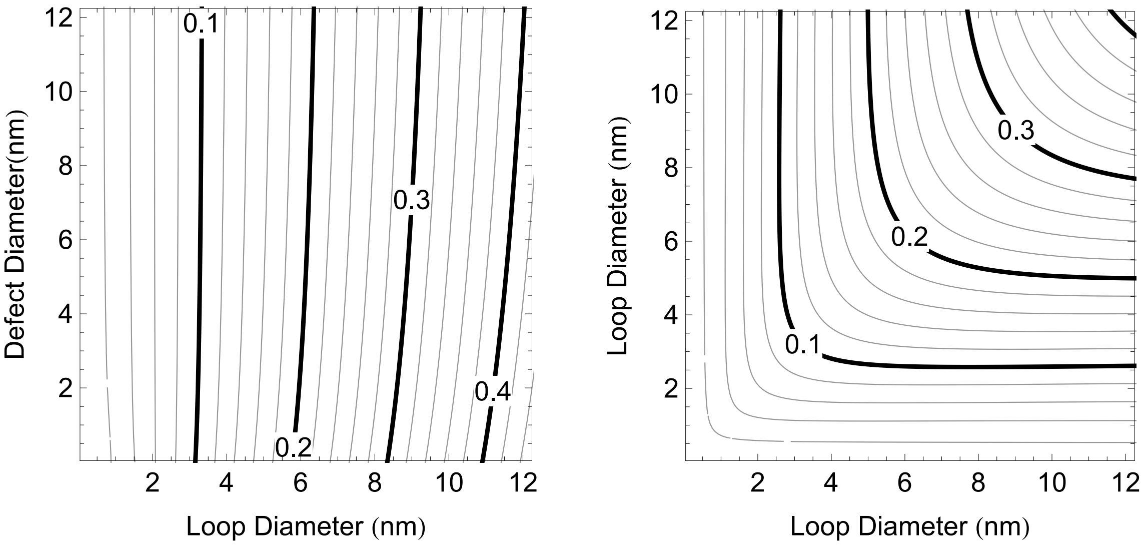

(a) Defect absorption Eq. (7.2)

(b) Loop coalescence Eq. (7.3)

Figure 7.5: Reduction in reaction rate magnitudes for one dimensional diffusers β_{1D} in a trap mediated system using a coalescence radius $r_d = 3b$ and a trap concentration of 200 ppm

7.2.3 Defect Evolution with One Dimensional Diffusion

To analyze the effect of one dimensional diffusion on the evolution of black dot damage microstructures, we applied both the two-mode and two-state reaction models. Due to the uncertainties governing the interactions amongst crowdion bundles, a number of cross section magnitudes were utilized. The critical distance for coalescence r_d was varied from $1.5b$ to $6b$. Additional calculations considered the cluster agglomeration condition described by Eq. (7.9), employing solid disk cross sections. As in the previous section, a case forbidding crowdion bundles from interacting with one another was imposed by constricting r_d to zero.

The impact of the coalescence cross section are presented in Figure 7.6, which shows the observable damage developed in a two-state calculation with dislocation traps. A number of interesting features appeared in the defect populations under these conditions. Notably, observable damage failed to develop when the coalescence of crowdion bundles was forbidden. Aside from this instance, the basic progression of damage evolution mimicked that of other reaction kinetics scenarios. The peak damage density, however, occurred at slightly later doses.

The aggregation cross section, which scales quadratically rather than linearly with loop size, gave an accelerating rate of growth. For the coalescence cross sections, shorter interaction distances resulted in slower growth rates. This may seem unsurprising, but a closer analysis reveals that such an effect is not as intuitive as it appears. A decreasing coalescence cross section also generated lower peak damage densities with the peak shifted to higher

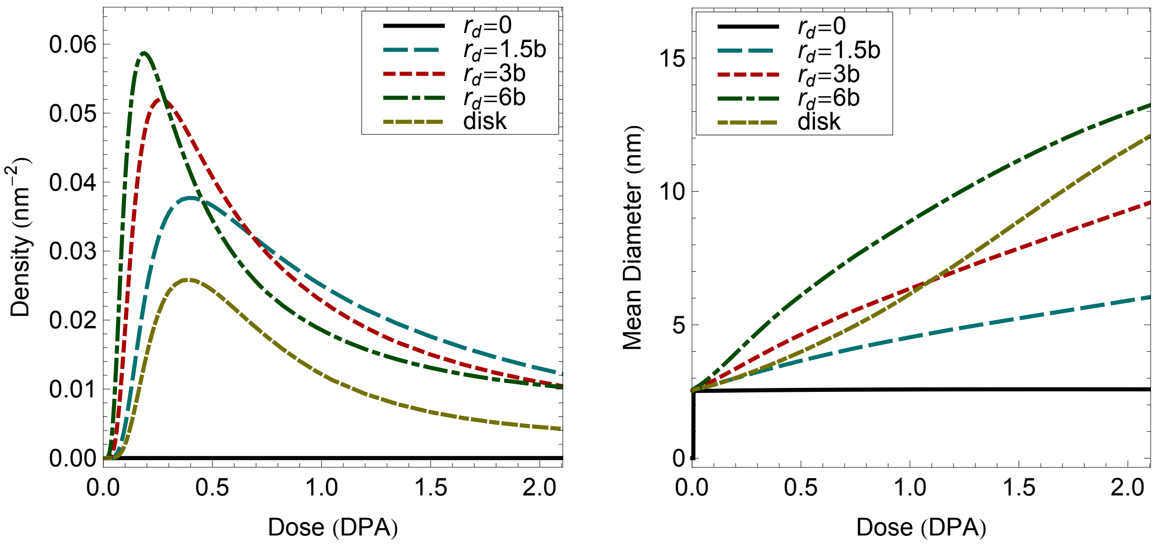

(a) Areal Density

(b) Size

Figure 7.6: Effect of interstitial cluster interaction cross sections on loop evolution. Defect areal density and size are shown for each of four differently sized cross sections based on Eq. (7.2.2) and one based on Eq. (7.9)

doses. This marks a deviation from the behavior noted in previous chapters, where parameter changes (as in the trap density for example) lowered the damage density but also hastened growth. Furthermore, the failure to grow to visible size when coalescence is forbidden, an effect not seen with three dimensional diffusion, indicates that the fate of single interstitials changed such that they were no longer permitted to drive growth.

Significant divergence appeared between the two trap mediated diffusion approaches, as compared to nearly identical performance for 3D reaction networks. Though the two models remained roughly comparable with dislocation traps, the differences between them became more pronounced with one dimensional diffusers. With interior traps, however, the two models exhibited widely different growth rates with defect densities separated by at least an order of magnitude. Figure 7.7 provides an example of these differences.

The discrepancy between the two approaches manifests in the vacancy population as well. Although no voids reach experimentally visible size using any of the reaction-diffusion systems considered in this chapter, a dense distribution of sub-visible nanovoids and isolated vacancies develops over the course of the irradiations. Typical of a recombination dominated regime, the immobile vacancy population is controlled through annihilation by mobile interstitials rather than diffusion to sinks. The total fraction of sites occupied by the vacancies, either as monomers or as members of clusters, is shown in Figure 7.8 for dislocation trapping.

The lower visible interstitial density observed within the two-mode approach was accompanied by a much denser vacancy population. Initially, the vacancy density increased similarly under both approaches, and more rapidly than in the three dimensional systems.

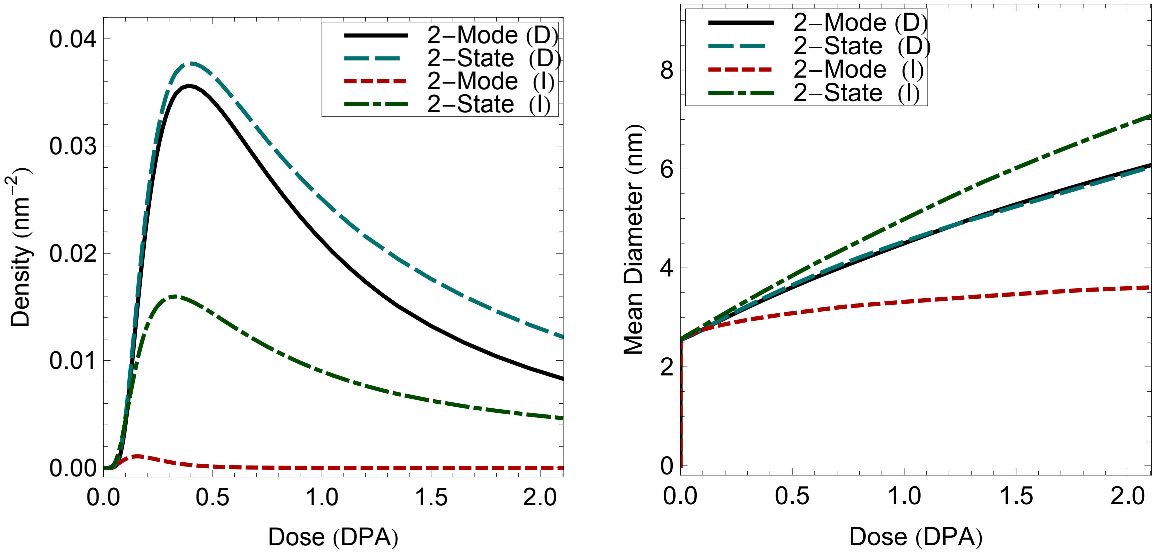

(a) Areal Denstiy

(b) Size

Figure 7.7: Comparison of damage evolution between trap different trap mediation approaches with 1D reaction kinetics. Loop density and size are shown assuming either dislocation(D) or interior(I) trapping mechanisms.

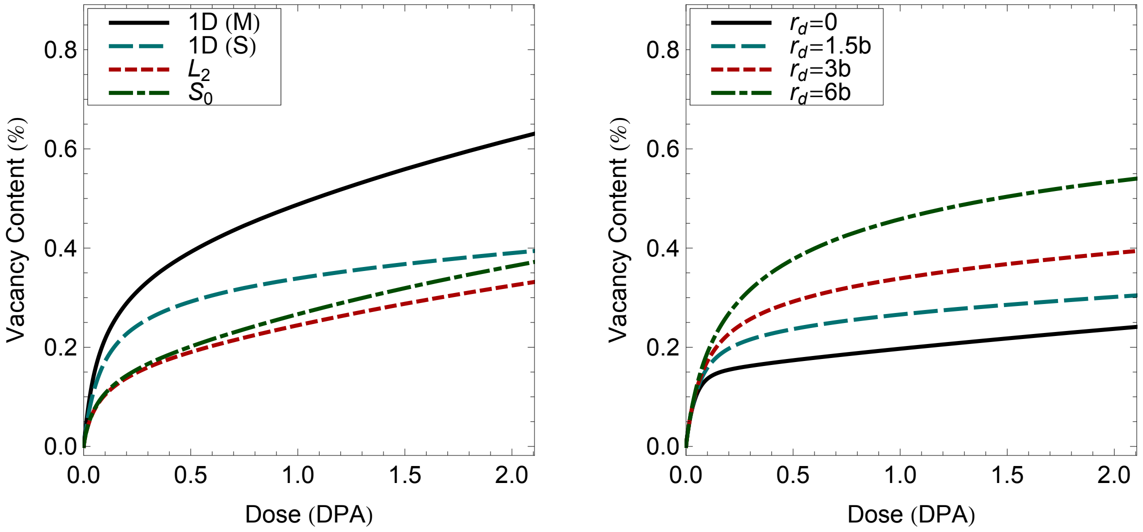

(a) Comparison of two-mode (M) and two-state (S) 1D reaction-diffusion systems alongside otherwise equivalent 3D systems

(b) Effect of interaction cross section in the two-state model

Figure 7.8: Evolution of the vacancy inventory in 1D and 3D trap mediated diffusion based kinetic models

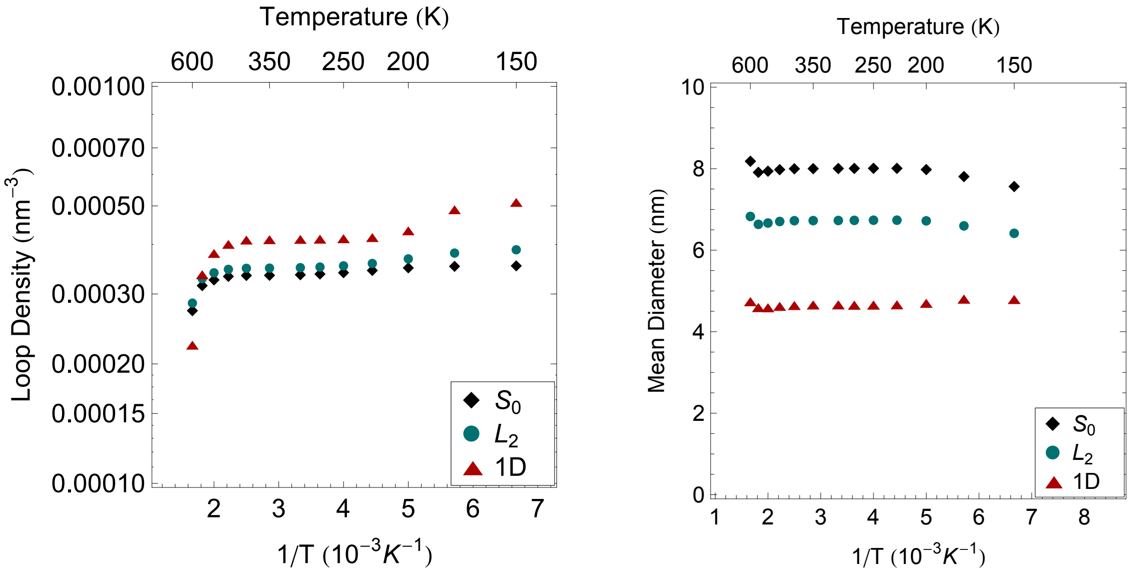

(a) Peak observable density (b) Mean diameter at 1 dpa

Figure 7.9: Temperature dependence of black dot development under 1D and 3D reaction-diffusion kinetic frameworks

Over longer time scales, however, population growth rates sharply diverged. Steady state growth of the vacancy density was slower in the two-state model than for either of the 3D reaction networks. The two-mode approach, by contrast, continued to rapidly seed vacancies to a concentration several times larger than in the other models. The cross section for coalescence also strongly impacted the vacancy density. As seen in Figure 7.8(b), a decreasing probability for coalescence coincided with a sparser vacancy inventory and a clear delineation between a prompt and steady state regime. This transition was present for larger coalescence cross sections as well, although it occurred over a longer dose increment.

The temperature dependence remained unaltered, despite the strong effects of one dimensional diffusers on loop growth. Figure 7.9 compares the density and size of loops over a range of temperatures examining the effects of dimensionality and reaction geometry. All three cases employed dislocation traps. The coalescence radius was set to $1.5b$ for the one dimensional case. The fundamental temperature trend persisted regardless of reaction kinetics, retaining minimal variation with temperature below 500K and decreasing defect densities at higher temperatures. This indicates that the effects of reaction geometry and one dimensional diffusion seen at 300K are not specific to that temperature. Some slight variations appeared below 200K, where the peak damage density increased only for the case of one dimensional reaction networks and growth rates slowed under three dimensional reaction networks.

Reaction dimensionality exerted a stronger influence on the relationship between loop density and trap density. Although the loop content still scaled with trap content, it did so

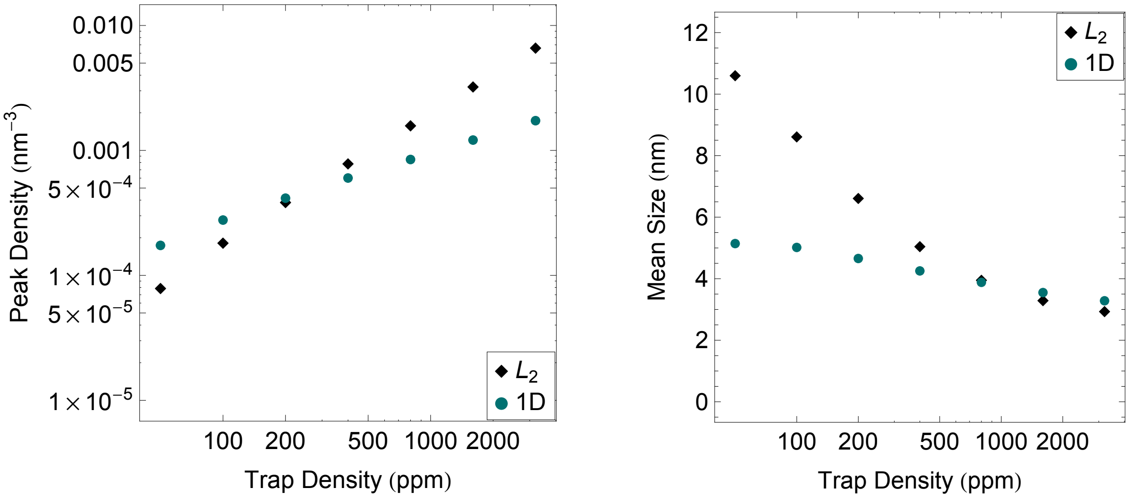

(a) Peak observable density

(b) Mean diameter at 1 dpa

Figure 7.10: Impact of trap density on interstitial loop development assuming either 1D or 3D crowdion reaction kinetics.

at a lower order with one dimensional kinetics as shown in Figure 7.10. One dimensional reactions also mitigated the impact of trap density on loop size. As with the temperature comparisons, a 1.5b coalescence radius was used in these calculations.

The effects of 1D diffusion are a natural consequence of the reduced reaction rates between crowdion bundles and other defects in the system. Recall that values of β_{1D} are as low as a few percent for the smallest of the one dimensional diffusers. These are the crowdion bundles produced in cascades, which contribute both to recombination and loop growth. This reduction, and a variation in its magnitude between models, is responsible for all of the changes seen in defect evolution.

The higher vacancy densities developed under one dimensional reaction networks are a clear consequence of the reduced ability of crowdion bundles to contribute to recombination. Due to the lower reaction rate with small vacancy clusters, crowdion bundles prefer traps or free surfaces. A higher density of both vacancies and crowdion bundles is required to achieve the same rate of annihilation, resulting in a higher vacancy concentration. As we will demonstrate later, the density of crowdion bundles is higher as well due to an increased preference for trapping over reaction.

The irradiation time required to reach the higher steady state crowdion bundle populations in a 1D diffusion framework is naturally longer, informing later saturation doses for visible damage. The higher density of small defect clusters in turn impacts the behavior of single, di-, and tri-interstitials, as a result of sink competition. These defects increasingly absorb onto the higher density of sub-visible clusters rather than visible loops. The depletion of the interstitial population before reaching visible clusters slows the apparent growth rates, and hampers the effectiveness of these defects at driving visible growth. This informs the absence of visible damage when coalescence is forbidden, despite the ostensibly identical reaction rate coefficients with single interstitials in the two systems.

The sensitivity to coalescence cross sections with faster visible damage growth rate also suggests that the absorption of crowdion bundles rather than isolated point defects drives loop growth in the one dimensional reaction network, although drawing such a conclusion may be less straightforward than first appearances might suggest. Indeed, increasing the coalescence cross section increases the rate of absorption of crowdion bundles on larger loops, but it also enhances the reaction of cascade born crowdions with one another, leaving fewer small trapped crowdion bundles in the bulk. In effect, a large coalescence cross section mitigates the effects introduced by applying one dimension reaction kinetics in the first place. A lower inventory of crowdion bundles implies both an increased vacancy density and a reduced contribution to the sink strength for single interstitials. The clear correlation seen between the vacancy inventory and the coalescence cross section reinforces this explanation.

The convoluted impact of crowdion bundle reactions leaves some uncertainty as to the true mechanism for loop growth as the coalescence cross section grows. The lower density of trapped crowdion bundles at larger coalescence cross sections reduces the net sink strength for point defects suggesting that more single interstitials reach the visible loops. On the other hand, the vacancy inventory also increases, which mitigates and perhaps even negates the effect of the lowered interstitial cluster density. In either case, the preference for interstitial absorption on dislocations as opposed to recombination increases. Indeed, the mass flux to the visible loops is identical regardless of whether the interstitials arrive one by one or in clusters, and distinguishing between the two is somewhat semantic.

More importantly, the reduced growth rate evident for smaller coalescence cross sections is accompanied by a lower damage density. The primary motivation for examining the reaction kinetics was that the model predicted clusters which were too large, too dense, or both when using standard three dimensional kinetics. The cross section effects are unique in our parametric explorations within the the trap mediated diffusion framework, where such adjustments generally decrease the density at the expense of increased size or vice versa. Furthermore, the strong correlation between the loop size and coalescence rates came coupled with a decrease in the sensitivity of loop size to trap density. Consequently, the experimental results could be easily reproduced in a one dimensional framework by selecting a sufficiently small cross section for interstitial cluster coalescence, and tuning the trap density to give the desired defect population.

At present, the information regarding the interaction of crowdion bundles is insufficient to justify any such attempts. Modifying the cross sections to produce a desirable fit would amount to little more than a curve fitting exercise, leaving the model with little physical significance. We instead point to the trends in loop density and size and suggest that a diminished preference for interstitial-interstitial reaction is required to explain the development of experimentally observed microstructures. In short, loops should feel repulsive rather than attractive interactions in a significant fraction of relative positions. If this is found not to be the case, the entire prospect of inter-cascade diffusion and agglomeration of interstitials into visible loops in a trap dominated medium becomes questionable, and some other mechanism for visible damage formation would be required.

The lack of temperature dependence persists regardless of reaction geometry or dimensionality, as is expected since no thermally activated effects are introduced by altering the defect dimensionalities or reaction conditions. Ballistic detrapping processes remain the driving force controlling the nucleation density in the trap mediated system. Consequently, the defect densities and sizes remain predominantly insensitive to temperature regardless of reaction rate details. Some minute changes occur at low temperatures, and fit well with the other effects of one dimensional diffusion discussed thus far. At these low temperatures, the di and tri interstitial mobility begins to decrease. Consequently, their transport to visible clusters is diminished and growth in the three dimension reaction networks slows. In networks with one dimensional diffusers, these defects are primarily absorbed by a high density of vacancy clusters and crowdion bundles in the first place, and their mobility is less evident in the growth rate.

The divergent solutions of the reaction limited two-mode and two-state effective medium approach to characterizing the trap mediated system deserve attention, and we concede that it indicates a critical flaw in the construction of one or possibly both models. As previously discussed, the two-mode diffusion approach requires a number of assumptions which are not generally satisfied. Additionally, this model was implemented with reaction limited contributions from irradiation activated hops which are not necessarily valid for clusters produced directly in irradiation events or clustering undergoing hops long enough to produce multiple reactions. Notably, the solutions became incomparable only when interior traps were assumed. Under these conditions, small cascade born crowdion bundles have very long paths between traps, and it is likely that the reaction limited rate coefficients are inapplicable for these clusters. We would not attempt to insist, however, that the clear flaws in this approach indicate that the other model is fully viable. Instead, we will attempt to provide other computational validation of the two-state reaction networks.

7.3 Kinetic Monte Carlo

Failure of a rate theory model to accurately describe the true system stems either from a mis-characterization of the fundamental properties of the defects or a violation of the mean field kinetic assumptions that form the foundation of the reaction rates of the system. The previous chapter focused on analyzing the first of these, modifying the defect mobilities and sizes to accommodate a number of physical phenomenon and investigate their importance to the system as a whole. This chapter modified the mean field kinetic assumptions to more accurately reflect the properties of interstitial clusters, however, this has introduced the second type of uncertainty. In the 3D case, the consistency of two different rate theory approaches provided some confidence that the mean field kinetics as implemented were well founded. Here, however, the two display contradictory behavior under certain conditions. Consequently, we turn to an inter-method comparison to establish confidence in the legitimacy of CD models in this domain.

Earlier, we used OKMC simulations to relax the spatial correlations associated with early stage cascade damage that are not handled well in mean field models. These methods can be applied on a larger scale to study longer term defect behavior, and serve as a companion or comparison model for CD. The objects that comprise the Monte Carlo method can be defined with the same properties that govern the rate theory models. In this manner, the OKMC model contains all the same defect mobilities, sizes, and other such physical specifications, but no assumptions about the resultant rates of interaction. Comparing the two models, therefore, serves as a suitable test of the accuracy of the reaction rate formula that drive cluster dynamics. Such comparisons have been performed for various simulation conditions in the past[141–143].

One might suggest that OKMC should be used generally in favor of rate theory models based on the smaller number of assumptions required. In practice, this is not tenable due to the enhanced computational restrictions associated with the residence time algorithm. As a consequence, the number and scope of our OKMC simulations were notably smaller than those achievable with CD. We selected only a few cases for inter-model comparisons, and the phase space of conceivable cluster properties was consequently constricted. These properties reflect, in our subjective judgment, the best characterization of the physical system. Consequently, only 1D diffusion was considered for crowdion bundles sized 4 and larger. Cross sections based on an interior trapping mechanism or a cluster agglomeration interstitial reaction were neglected entirely.

To emulate a thin foil configuration, the simulations were housed in orthorhombic boxes with periodic boundaries in two directions and black absorbers in the third. The box size matched the foil thickness in the absorbing direction, but could be varied freely in the periodic directions. Simulation in a box with periodic dimensions much larger than the foil thickness might seem ideal for obtaining defect populations free of statistical anomalies, but in practice the simulation time scales linearly with volume at best, and increasing these dimensions much beyond the foil thickness becomes prohibitive. Instead, multiple identical simulations were run in smaller boxes.

The thermal mobilities of clusters were parameterized identically to the rate theory case. The conditions for reaction were defined identically to the rate theory as well. Loops were considered stable in the vicinity of a set of randomly distributed trap objects which did not interact with any other defects in the system or one another. Newly created defects moved in a one dimensional instantaneous random walk checking for reactions at each step. Detrapping events were implemented as a sequence of jumps in a single direction, again checking for reactions at each step. Both processes continued until reaching a trap, shrinking to a three dimensional cluster, or reaching an absorber.

Primary damage was introduced in the form of isolated defects and clusters rather than cascades. The probability of producing any given cluster was drawn from the aged cascade distribution used as source terms in the CD models. This approach was taken because the purpose of these simulations is to analyze the reaction-diffusion networks in CD. The isolated damage approach maintains strict consistency with the CD implementation of primary dam-

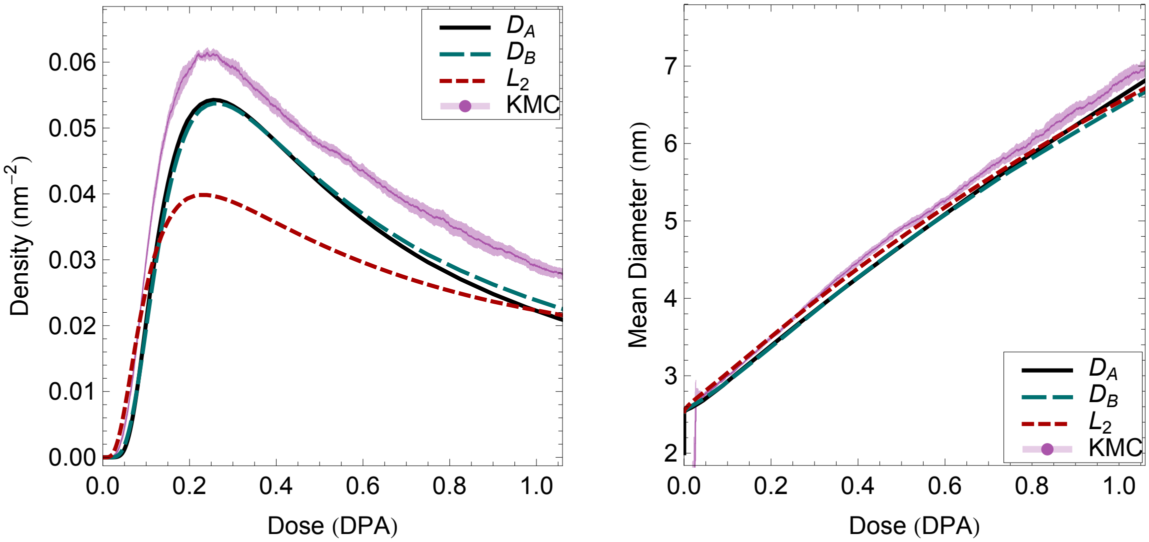

(a) Observable density

(b) Mean diameter

Figure 7.11: Evolution of visible damage in KMC compared to CD models, showing comparisons of visible density and size

age. Additionally, implanting cascades directly introduces the possibility of prompt overlap of existing and newly generated defects introducing physical events not considered in the CD models. The location at which each defect was produced was random, save for two considerations. The probability along the thin foil direction was weighted by the depth distribution of damage, and locations that would lead to the immediate reaction of the new cluster with a previously existing cluster were forbidden.

Figure 7.11 compares the evolution of the observable defect population in KMC simulations to three CD models. The Monte Carlo data shown comes from the average[1] of 10 simulations in $75 \times 75 \times 100$ nm boxes. These are compared against three versions of the CD model, which differ from those presented earlier only in that the dislocation sink strength was not included. These include both a two-mode (D_A) and two-state (D_B) approach to 1D diffusion and the coalescence based model of 3D diffusion (L_2).

The evolution of the visible defect population with respect to dose in the Monte Carlo simulations closely followed that seen in both one dimensional CD calculations. The density of loops consistently exceeded the rate theory calculations by roughly 10 to 20 percent across the entire dose interval. The three dimensional calculations matched neither in magnitude nor in evolution with dose. The mean size evolution closely followed all the rate theory models, which were roughly equivalent for this condition where $r_d = 3b$. Thus, assessing the performance of the rate theory requires a more detailed examination of the defect content of the system.

---

[1] Uncertainty bounds given by two standard deviations of the mean are included in all Monte Carlo data excepting defect size profiles, though in many cases these cannot be resolved in the plotted data

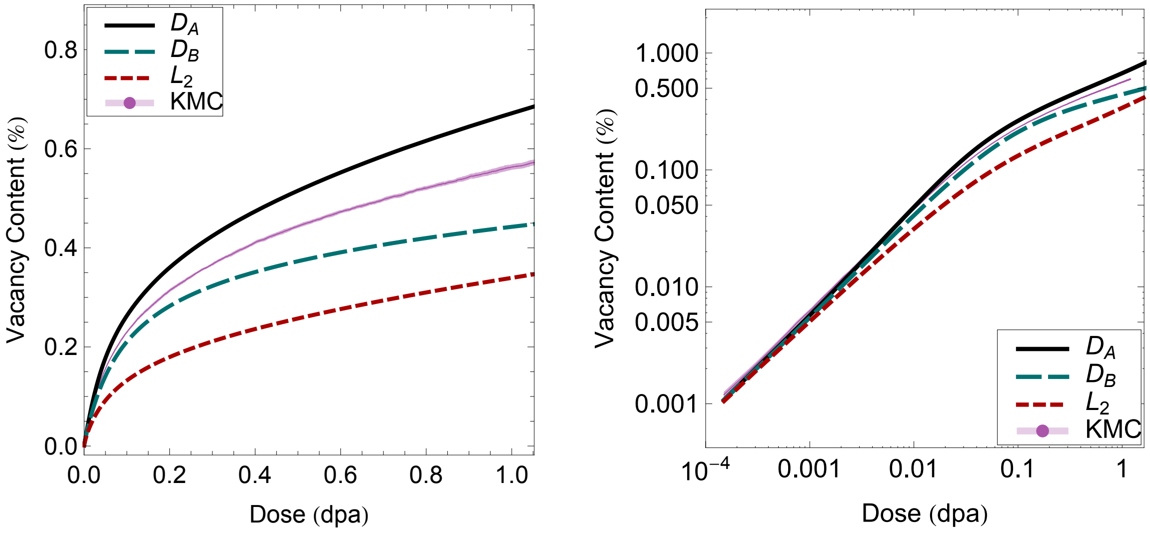

(a) Linear scale (b) Logarithmic scale

Figure 7.12: Net vacancy retention in KMC and CD approaches presented on both linear and logarithmic scales

The total vacancy inventory is shown in Figure 7.12 as a percentage of the atomic concentration. The Monte Carlo vacancy inventory clearly exceeds the three dimensional case and lies between the two calculation methods in the one dimensional case. At early doses, this quantity increases almost linearly at a rate slightly below 5%/dpa in all CD calculations as well as the OKMC simulations. Significant divergence from this prompt behavior begins first in the three dimensional kinetics, but below a tenth of a dpa in all cases. Experimental information on the vacancy inventory of irradiated ferritic alloys collected through positron annihilation spectroscopy is available, although the data is limited and the uncertainty associated with this technique is substantial. Positron measurements on neutron irradiated iron at 70^oC exhibit trends qualitatively similar to the one seen in our models, with prompt vacancy accumulation rates of roughly 2 to 4 %/dpa[144].

Measuring the interstitial population required some additional considerations. As parameterized in these models, vacancies were immobile at room temperature so they cannot reach the free surfaces, which was not the case for interstitials. In a real material, extra interstitials which reach the surface become surface adatoms. In large enough numbers, they form additional layers and cause swelling. This surface swelling was calculated by integrating the flux of clusters at the surface in CD, while the clusters removed by contact with the black absorbers were counted in KMC simulations. Figure 7.13 illustrates the retained and the escaped interstitial content as a function of dose.

The Monte Carlo simulations produced a larger interstitial inventory than any of the rate theory models. This excess correlates closely with the difference in visible cluster density. A continuous increase in the total inventory was seen in all cases except the two-mode

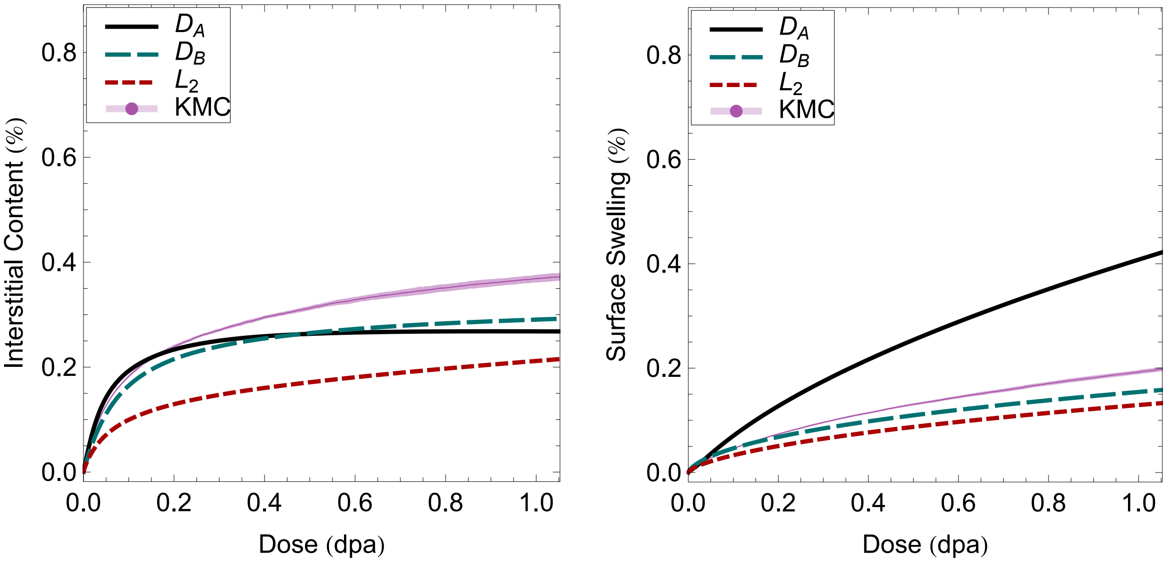

(a) Retention

(b) Loss to surfaces

Figure 7.13: Net retained and escaped interstitial content.

rate theory approach which showed saturation and slight decline. Conversely, the rate of interstitial escape to the free surface was much larger in this case than the other simulations.

In addition to comparing information regarding the aggregate cluster populations, the performance of CD models can be evaluated on the basis of individual species populations. We have thus far avoided the temptation of comparing defect size profiles to experiment, as the TEM data on size distributions is likely unreliable, particularly for small cluster sizes as discussed in Chapter 2. For intermodel comparisons, however, this is perhaps the most powerful analysis available.

To obtain the density profiles from Monte Carlo simulations the defect concentration in the simulation box was averaged over a finite interval. This procedure guaranteed a representative sampling of short lived defects which were not likely to be found in the box at any given step. An exposure time of 1 second (roughly 10^{-3} dpa) produced sufficient statistics for our simulations. The size profiles for small defect clusters is shown in Figure 7.14.

Given the differences in aggregate populations between the CD and KMC models, it is not surprising that the agreement in size profiles was imperfect as well. When analyzing any discrepancies, it is important to distinguish between a difference in magnitude and a change in the shape of the size distribution. For vacancy clusters, the distributions are all in agreement, although they vary in magnitude. For interstitial clusters, however, the two-mode (D_A) calculations provide a clearly inaccurate size distribution, while the three dimensional kinetics generate a profound difference in magnitude. For clusters in this size range, the closest agreement in both shape and magnitude is provided by the two-state model.

For clusters of larger size, any given species was sufficiently rare in the KMC simulations

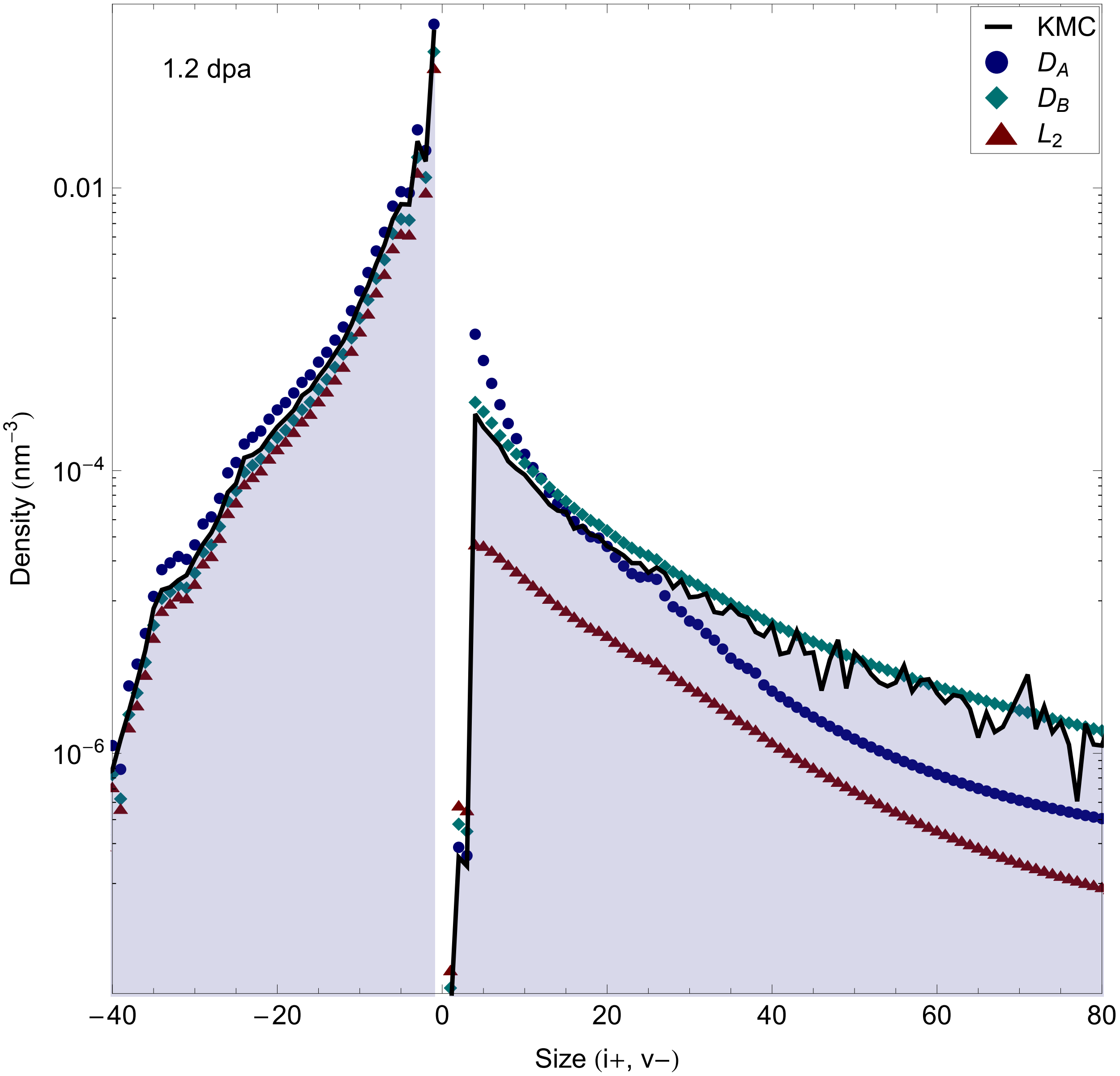

Figure 7.14: Depth averaged defect content as a function of cluster size. CD data are represented by points and KMC data are joined.

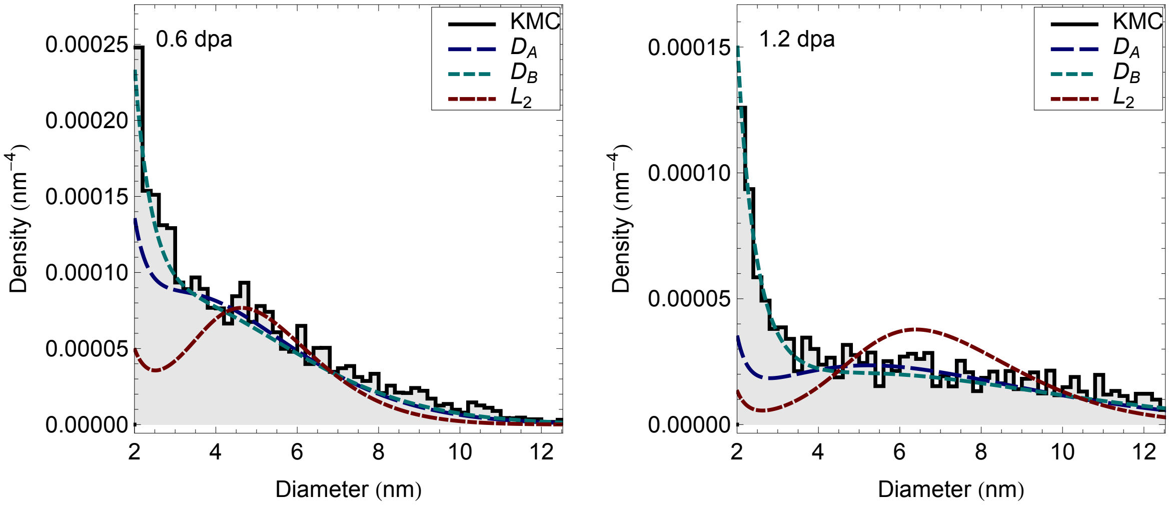

(a) 0.6 dpa (b) 1.2 dpa

Figure 7.15: Density distribution by cluster size for defects larger than 2 nm. CD data are plotted as continuous distributions while KMC populations are averaged over discrete bins.

that good statistics could not be obtained for each cluster individually. Instead, clusters were grouped by radius to generate size profiles for larger clusters. Visible cluster size profiles are compared at select doses in Figure 7.15. The superior performance of the two-state model is evident in this data as well, although the error of the two-mode model was confined to the smaller cluster sizes. The three dimensional kinetics generate an entirely different size profile, which shows a peaked rather than continuously diminishing distribution.

The assortment of defect population indicators agree most favorably with the two-state implementation of one dimensional reaction kinetics. The rate theory approaches consistently underestimated the defect inventory generated by Monte Carlo simulations by every indicator considered. In this regard, both one dimensional kinetic models outperform the three dimensional approach, but neither is clearly superior to the other. The advantage of the two-state model is evident in its excellent reproduction of the Monte Carlo defect size profiles.

There are several possible explanations for the discrepancy in defect inventory magnitudes between the rate theory and Monte Carlo calculations. It may be a simple matter of how one dimensional hops have been implemented in this Monte Carlo approach. Following the detrapping events, cluster glide is represented as purely ballistic rather than diffusive. This may be sufficient to promote glide to the surface over recombination as compared to the mean field models and could explain the difference in populations. This possibility warrants some discussion.

The degree to which loop hopping is diffusive as opposed to ballistic is unclear. According to the detrapping mechanism we proposed earlier, at least part of the motion is ballistic.

If the motion is primarily diffusive, it implies some spatial correlation with the initial trap which is not considered in the mean field kinetics. That possibility is predicated on the assumption that the traps - whatever they may be - survive a detrapping event intact. In short, there is too much uncertainty in the nature of the traps at the present time to attempt to account for such fine grained details.

Alternatively, the differences could result from a more systematic deficiency in the mean field approach. Indeed, higher defect inventories generated by Monte Carlo approaches is a trend common to the findings of other researchers[141–143]. The lower populations present in rate theory models suggest that the mean field approach overestimates the rate of reaction between defect clusters. This is a counterintuitive suggestion, as the primitive cell rates used for 3D reaction kinetics are slower than those derived from the presumably more accurate effective medium approach. If there were a systematic error in the mean field models as formulated here, we would expect it to underestimate reaction rates.

Regardless of the cause of the discrepancies, their magnitude is small when compared to the sensitivity of either kinetic model to basic defect properties. The dimensionality of reaction kinetics, the migration energies of clusters, and particularly the hopping of loops all have a more significant impact on defect evolution. The purpose of these comparisons was twofold, to determine which set of defect parameterizations performed best and whether the mean field kinetic model accurately represented the rates of reaction between defect clusters at all. Comparing across a variety of metrics demonstrates the efficacy of the two-state model for interstitial clusters with one dimensional reaction kinetic assumptions. Though inconsistencies do exist, they pale in comparison to the propagation of uncertainties in basic defect properties. In other words the mean field assumptions - so long as a proper fundamental kinetic model is imposed - are not the dominant source of error.

Instead, any failure to accurately portray the real system lies primarily in the parameterization of the defects and their properties. As such, the conclusion of the previous section stands. For these kinetic models to provide a precise reproduction of experimental observations of black dot density and size, the cross section for reaction between interstitial clusters must be smaller than what we have implemented here. This can be rationalized either by a repulsive interaction between clusters in some fraction of the possible approach configurations, or a more selective condition for spontaneous reaction than the overlap of dislocation cores.

Inter-cascade diffusion is not the only candidate for the formation of visible damage features in iron. In other metals, the collapse of the defects produced in a single cascade into one central cluster is responsible for observable features. This is unlikely in bcc metals as noted in Chapter 2 and as seen in the cascade structure of iron in Chapter 5. The possibility of collapse following multiple cascades in the same region, however, is not so easily dismissed. We have ignored the possibility of such "cascade overlap" effects. Any attempt to include them in a rate theory based approach would generally entail a reduction in the magnitude of source terms as the background defect concentration increases, and some cascade induced reaction density between existing clusters beyond the thermal diffusion limit.

In effect, a cascade overlap driven rate theory model would look very similar to the trap mediated model we have proposed. Both call for some mechanism for reducing the thermal mobility of interstitial clusters below what is predicted by atomistic methods. Both rely on an irradiation driven mechanism dominating the kinetics of reaction between defect clusters. In this sense, the cascade overlap and trap mediated diffusion paradigms for defect cluster formation are merely restatements of one another, and the differences between them are largely semantic. This is particularly true in light of the detrapping mechanism we have posited, where loops are propelled toward the cascade core. This approach to the ides of cascade overlap involves some second order correction to the present model.

We have not considered the impact of this implicit spatial correlation between mobile interstitial clusters and newly created primary damage on the reaction kinetics, which may provide an alternate mechanism to limit cluster growth. The effects that existing defects might have on cascade development remain a weak link in the multiscale modeling concept employed throughout this work. Including such details proves extremely difficult, as it requires some degree of reverse communication. Rather than the approach seen here where small scale methods are used to parameterize larger ones, considering the direct interaction of primary damage with existing defects in the cascade phase would require atomistic simulations consistent with the state of the larger system. In effect, this demands a database of cascade simulations run against a wide array of pre-existing defect structures. The cost for performing enough MD simulations to cover the phase space of possible background defect populations in any meaningful way is beyond prohibitive.

Chapter 8

Conclusions

This work has used a series of kinetic models to assess and explain the development of "black dot" damage microstructures in ferritic alloys at temperatures below 600 K. Such models quantify the rates at which small clusters agglomerate into larger ones, which eventually become sufficiently large to be seen as visible damage. They can also provide an assessment of the basic properties of the defect clusters which drive microstructural evolution. The primary objective in this respect was to unify disparate sources of information regarding interstitial cluster properties into a unified, cohesive explanation of their behavior. We sought to demonstrate that a model of interstitial clusters that incorporated all their known properties also reproduced the evolution of visible damage in a way more naive approaches could not.

8.1 Model Performance

Any physically based model of radiation damage must start from a description of the lattice defects, as created from recoil events. This model takes a very focused approach to primary damage, characterizing specific ion irradiation conditions with a high a degree of fidelity. The aim is to accurately reproduce not only the spatial distribution of defects throughout an *in situ* foil, but also to accurately asses the initial clustering state of these defects as well. A combination of molecular dynamics and Monte Carlo enable such a description.

With primary damage well characterized, the challenge of kinetic models becomes a matter of accurately assessing the mobility and interaction properties of defects and defect clusters. In iron, the greatest uncertainty at the present time arguably revolves around the mobility of interstitial clusters. Many kinetic models consider interstitial clusters above a certain size to be immobile. This convention is in strong contrast to revelations of the properties of these clusters raised by molecular dynamics simulations. Crowdion bundles diffuse with very low activation energies, on the order a few dozen meV, and should be even more mobile that the isolated interstitial in iron even up to visible cluster sizes according to MD simulations. This magnitude of mobility is not observed in experiments, and would clearly prohibit the thermal stability of any interstitial type dislocation loops in the microstructure.

With a traditional model assuming low interstitial cluster mobility, reaction-diffusion rate theory based models function only with Frenkel pair damage. When an accurate account of the primary damage state which includes a significant fraction of interstitials in clusters is included and interstitial clusters are considered to be immobile, diffusion based models break down. Instead of giving rise to any variety of visible size microstructural features in this regime, kinetic models instead fail via a nucleation catastrophe in which an unphysically high density of cascade damage develops without recombining or coalescing into extended defect structures.

The discrepancy between the apparent and ideal mobility of crowdion bundles is explained by the phenomenon of trapping. The free glide of dislocations is impeded by impurities, and there is no apparent reason why nanometer size dislocation loops should pose an exception. The logical consequence of such interactions is a trap mediated diffusion medium, in which the low activation free glide of crowdion bundles is disturbed locally by impurities, which form a distribution of discrete trapping sites.

There is a variety of experimental and modeling evidence that supports this concept of interstitial cluster behavior in iron. These range from TEM observations of discontinuous cluster motion to molecular statics calculations which show string binding energies between crowdion bundles and various impurity structures. There is some uncertainty at this juncture, however, as to the precise nature of the traps. A number of possible trap structures have been proposed, and it is not clear which candidate or candidates actually contribute to crowdion trapping in a real material.

During *in situ* ion irradiation and in some cases electron irradiation, trap mediation gives rise to another interesting aspect of defect behavior. During irradiation, and only during irradiation, defects that appear to be thermally sessile participate in infrequent, rapid, long range, isolated motions dubbed hops. This irradiation induced mobility is plausibly explained by ballistic ejection of an interstitial cluster from a trapping site followed by rapid glide to a new trapping site. Including the full range of trap mediated interstitial behavior in a kinetic model gives rise to a vastly altered trend in the defect evolution.

The nucleation catastrophe of earlier kinetic models does not occur in the trap mediated framework. Our model examined the effects of a variety of possible trap candidates on the microstrucural evolution. The trends in defect density much more closely resemble experimental observations, where early saturation in defect density is followed by a stable or declining loop population. In this sense, the trap mediation approach to interstitial kinetics not only represents a better description of the known properties of interstitial clusters, but also allows an explanation of the formation of black dot microstuructures not available to simpler descriptions of interstitial kinetics.

The performance of cluster dynamics models with trap mediated diffusion is far from perfect. Even at very low temperatures, the standard formulation of cluster dynamics gives fast loop growth rates, on the order of 5 to 10 nm per dpa. This is clearly irreconcilable with typical observations of black dot behavior at room temperature, where growth is slower if it occurs at all. Adjustment of physical parameters - namely the trap density - has the potential to impact the growth rate, but such changes also produce much higher defect densities. The magnitude of density and growth rate seen in experiments simply could not be obtained simultaneously. In an attempt to resolve this discrepancy, we investigated some assumptions of the standard approach which are suspect in a real material, namely isotropic reaction volumes and three dimensional diffusion.

Reaction volumes of dislocation loops are certainly anisotropic, particularly for large loops absorbing point defects. Fully accounting for this is difficult, but some simple improvements have historically been made for classical rate theory applications. The effects of reaction volume modifications are relatively minor compared to the impacts of one dimensional diffusion. When diffusing in one dimension, the kinetics of reaction for a defect scale very differently with reactant sizes and densities, leading to significant fundamental differences in cluster populations.

In a one dimensional paradigm, the cross section for interaction becomes key to formulating the reaction kinetics. These are particularly difficult to define given present knowledge of defect interactions, particularly between defect clusters. Intuition suggests that the relative positions of these clusters often produces repulsive rather than attractive interactions, limiting this cross section, though it is not immediately clear to what extent. Initial Monte Carlo investigations of loop interactions in bcc iron have shown a somewhat stochastic interaction behavior, casting further uncertainty on this effect.

We investigated a number of magnitudes for these cross sections, illustrating that their size greatly impacts the ultimate growth behavior of loops. Smaller cross sections lead to lower growth rates, as migrating crowdion bundles recombine on vacancy clusters rather than absorbing on loops and monomer interstitials become increasingly partitioned to unabsorbed crowdion bundles. Though the density of these sub-visible defects increases with declining reactivity, the peak density of visible defects declines, leading to a change in the predicted size profile which shifts in favor of smaller clusters with a long tail to large sizes.

The cluster evolution in CD models developed to reflect one dimensional diffusion compared favorably with OKMC simulations using the same physical parameters. The agreement between the two suggests that the mean field kinetic assumptions employed to construct CD reaction rates are sound. The physical parameters that define both models, however, are still open to question and the accuracy of several are shrouded in uncertainty. This is particularly true of the interaction cross sections between interstitials, as discussed. A few additional factors, such the trap mechanisms and densities as well as the ultimate vacancy mobility in ferritic alloys remain to be definitively quantified.

Overall, trap mediated diffusion systems give rise to defect populations that qualitatively match the microstructures evident in *in situ* irradiation experiments. The experimental features reproduced by this model include

- a saturation in defect density at low doses,
- weak temperature dependence in ion irradiations,

- a change in temperature dependence in electron irradiations,
- linear or sub-linear growth in size for visible defects, and
- rapid vacancy accumulation at low dose.

Detailed quantitative comparisons were not presented owing to both the uncertainty inherent in parameterizing these models at the present time and the variability in experimental data sets. We have made the case that the loop growth rate is highly susceptible to the coalescence cross section which governs the interaction rate between interstitial clusters. Only if this quantity is small can experimental loop sizes and densities be attained. Should this be confirmed, the trap mediation model provides a pathway for explaining the variablility in experimental data between nominally similar alloys through other sensitive parameters, primarily the trap density.

8.2 Future Work

This work opens the frontier for future similar research into the irradiation behavior of other materials and at other temperatures. Due to the generally high mobility of interstitial clusters, iron is not the only material system in which trap mediation will play some role in the irradiation response at high dose rates. This is true of other bcc materials in particular, for which the structure of defect clusters are similar and crowdion bundles exhibit very similar behavior in simulations.

In the iron system itself, we have restricted our analysis to temperatures below and on the low end of the operating temperature window for F/M steel target applications. This was done deliberately to avoid a few challenging microstructural features that emerge past 600K. The most important of these is the transition of the loop population to an exclusively $\langle 100 \rangle$ character. A microstructural model applicable at higher temperatures requires a mechanism for forming these loops, which remains controversial. On the other hand, kinetic models similar to the one used here hold the potential to evaluate the validity of a variety of proposed mechanisms for $\langle 100 \rangle$ loop formation by comparing the predicted evolution for each mechanism to experimental observations.

This model also introduces the ability to quantitatively evaluate a number of standing observations regarding the differences in behavior between alloys of nominally similar structure or composition. The difference in defect density between high purity iron and other alloys, for example, can be explained by the trap mediated framework simply in terms of an elevated trap density. Establishing such relationships might shed some light on the long term behavioral differences of different alloys, and could identify which components of an alloy are crucial to the defect evolution. Modeling with this level of fidelity, however, would require a more detailed understanding of the composition and action of traps which both remain unclear at the present time. As with the matter of loop character, this presents the opportunity for using the model to validate or reject trap candidates, by comparing modeling predictions of the impact of predicted trap to the behaviors of materials where that trap does and does not occur.

The uncertainties in trap constituency and loop character together complicate this model at high temperatures in iron. We maintain that interstitial carbon, or small complexes thereof, are the most plausible candidate as crowdion traps. Should this interpretation prove correct, the migration of carbon, the potential for thermal dissociation of traps, and the coupling to precipitation behavior undoubtedly alter crowdion bundle behavior in a non-trivial manner. Such effects become evident near the upper bound of the temperature range in this study, where carbon becomes mobile. A more detailed understanding of the thermal behavior of traps, whatever they may be, could introduce some additional thermal dependence to the defect evolution, and alter quantitative predictions of defect distributions.

Numerous challenges complicate the application of kinetic models in a form relevant to in-reactor service conditions. Of these, one of the most significant is reaching the high doses real materials will see, at least an order of magnitude higher than any of the simulations in this body of work. Reaching higher doses will involve longer computation times and larger defect sizes, requiring many more equations. It is not clear whether CD as formulated here can accomplish this task, but doing so will likely require grouping schemes in phase space or other heuristic techniques to reduce the problem size. It may prove more effective to use CD merely to inform coarser grained semi-empirical approaches which suppress the full details of the reaction network in a manner analogous to the suppression of atomic scale resolution in kinetic models.

The terminal objective of this type of modeling effort is to encompass a sufficient understanding of the fundamental behavior of point defect clusters to determine why microstructural features develop. Such understanding allows assessments of the effect of altering the irradiation environment on the evolution of those features. This is important because many experiments aim to emulate high dose neutron irradiation with ion irradiation at dose rates up to four orders of magnitude higher than in-reactor conditions. The extent to which such modifications impact the formation and growth of damage is not evident by inspection, but appropriate kinetic models can shed light on such effects. The temperature shift in void swelling is one such example, concisely explained by classical rate theory.

Modern kinetic models offer the opportunity to evaluate dose rate effects for a variety of phenomenon beyond steady state void swelling, such as black dot development as examined here. For ferritic steels, the target operating temperatures are slightly higher than the regime we have focused on. Thus, the development of models to examine dose rate effects for the application temperature window will likely need to include the improvements already mentioned, $\langle 100 \rangle$ loop formation and a better understanding of the nature of interstitial traps, as well as the abitility to include transmutation helium and its effects on the defect population. Though ambitious, such a model would be a powerful tool in delineating between the features of ion irradiations that correspond to neutron irradiation microstructures, and those that are merely artifacts of the irradiation condition.

Bibliography

[1] S. J. Zinkle, “Fusion materials science: overview of challenges and recent progress”, Phys. Plasmas **12** (2005) 058101.

[2] A. Kimura, “Current status of reduced-activation ferritic/martensitic steels r&d for fusion energy”, Mat. Trans. **46** (2005) 394–404.

[3] N. Baluc, D. Gelles, S. Jitsukawa, A. Kimura, R. Klueh, G. Odette, B. van der Schaaf, and J. Yu, “Status of reduced activation ferritic/martensitic steel development”, J. Nucl. Mater. **367-370** (2007) 33–41.

[4] R. Klueh, D. Gelles, S. Jitsukawa, A. Kimura, G. Odette, B. van der Schaaf, and M. Victoria, “Ferritic/martensitic steels overview of recent results”, J. Nucl. Mater. **307-311** (2002) 455–465.

[5] R. Klueh and A. Nelson, “Ferritic/martensitic steels for next-generation reactors”, J. Nucl. Mater. **371** (2007) 37–52.

[6] D. Gelles, “Void swelling in binary fe-cr alloys at 200 dpa”, J. Nucl. Mater. **225** (1995) 163–174.

[7] F. Garner, M. Toloczko, and B. Sencer, “Comparison of swelling and irradiation creep behavior of fcc-austenitic and bcc-ferritic/martensitic alloys at high neutron exposure”, J. Nucl. Mater. **276** (2000) 123–142.

[8] R. Klueh and J. Vitek, “Tensile properties of 9cr-1movnb and 12cr-1movw steels irradiated to 23 dpa at 390 to 550 ^{o} c”, J. Nucl. Mater. **182** (1991) 230–239.

[9] R. Klueh, K. Ehrlich, and F. Abe, “Ferritic/ martensitic steels: promises and problems”, J. Nucl. Mater. **191-194** (1992) 116–124.

[10] K. Farrell and T. Byun, “Tensile properties of ferritic/martensitic steels irradiated in hfir, and comparison with spallation irradiation data”, J. Nucl. Mater. **318** (2003) 274–282.

[11] M. L. Jenkins, C. A. English, and B. L. Eyre, “Heavy-ion irradiation of α-iron”, Philos. Mag. A **38** (1978) 97–114.

[12] D. Kaoumi, J. Adamson, and M. Kirk, “Microstructure evolution of two model ferritic/martensitic steels under in situ ion irradiation at low doses (02 dpa)”, J. Nucl. Mater. **445** (2014) 12–19.

[13] C. Topbasi, A. T. Motta, and M. A. Kirk, "In situ study of heavy ion induced radiation damage in nf616 (p92) alloy", J. Nucl. Mater. **425** (2012) 48–53.

[14] M. Horiki, T. Yoshiie, M. Iseki, and M. Kiritani, "Invisible and visible point defect clusters in neutron irradiated iron", J. Nucl. Mater. **271-172** (1999) 256–260.

[15] Z. Yao, M. Hernandez-Mayoral, M. Jenkins, and M. Kirk, "Heavy-ion irradiations of fe and fecr model alloys part 1: damage evolution in thin-foils at lower doses", Philos. Mag. **88** (2008) 2851–2880.

[16] M. Hernandez-Mayoral, Z. Yao, M. L. Jenkins, and M. A. Kirk, "Heavy-ion irradiations of fe and fe-cr model alloys part 2: damage evolution in thin-foils at higher doses", Philos. Mag. **88** (2008) 2881–2897.

[17] L. Horton, J. Bentley, and K. Farrell, "A t.e.m. study of neutron irradiated iron", J. Nucl. Mater. **108-109** (1982) 222–233.

[18] M. Kirk, I. Robertson, M. Jenkins, T. Black, and J. Vetrano, "The collapse of defect cascades to dislocation loops", J. Nucl. Mater. **149** (1987) 21–28.

[19] I. Robertson, M. Kirk, and W. King, "Formation of dislocation loops in iron by self-ion irradiations at 40k", Scripta Met. **18** (1984) 317–320.

[20] I. Robertson, M. Jenkins, and C. English, "Low-dose neutron-irradiation damage in α-iron", J. Nucl. Mater. **108-109** (1982) 209–221.

[21] M. Kiritani, "Defect interaction processes controlling the accumulation of defects produced by high energy recoils", J. Nucl. Mater. **251** (1997) 237–251.

[22] B. Masters, "Dislocation loops in irradiated iron", Philos. Mag. **11** (1965) 881.

[23] Z. Yao, M. Jenkins, M. Hernndez-Mayoral, and M. Kirk, "The temperature dependence of heavyion damage in iron: a microstructural transition at elevated temperatures", Philos. Mag. **90** (2010) 4623–4634.

[24] M. A. Kirk, P. M. Baldo, A. C. Liu, E. A. Ryan, R. C. Birtcher, Z. Yao, S. Xu, M. L. Jenkins, M. Hernandez-mayoral, D. Kaoumi, and A. T. Motta, "In situ transmission electron microscopy and ion irradiation of ferritic materials", Microscopy Research and Technique **72** (2009) 182–186.

[25] A. Brailsford and R. Bullough, "The rate theory of swelling due to void growth in irradiated materials", J. Nucl. Mater. **44** (1972) 121–135.

[26] A. Brailsford, R. Bullough, and M. Hayns, "Point defect sink strengths and void swelling", J. Nucl. Mater. **60** (1976) 246–256.

[27] A. Brailsford and R. Bullough, "The theory of sink strengths", Phil. Trans. R. Soc. Lond. A **302** (1981) 87–137.

[28] F. A. Nichols, "On the estimation of sink-absorption terms in reaction-rate-theory analysis of radiation damage", J. Nucl. Mater. **75** (1978) 32–41.

[29] D. R. Olander, *Fundamental aspects of nuclear reactor fuel elements* (National Technical Information Service, Springfield, Virginia, 1976) Chap. 19.

[30] G. S. Was, *Fundamentals of radiation materials science* (Springer, New York, 2007) Chap. 5.

[31] L. Mansur and E. Lee, "Theoretical basis for unified analysis of experimental data and design of swelling-resistant alloys", J. Nucl. Mater. **179-181** (1991) 105–110.

[32] L. Mansur, "Correlation of neutron and heavy-ion damage", J. Nucl. Mater. **78** (1978) 156–160.

[33] L. Mansur, "Theory and experimental background on dimensional changes in irradiated alloys", J. Nucl. Mater. **216** (1994) 97–123.

[34] T. Okita and W. Wolfer, "A critical test of the classical rate theory for void swelling", J. Nucl. Mater. **327** (2004) 130–139.

[35] C. W. B.N. Singh a, H. Trinkaus b, "Production bias and cluster annihilation: why necessary?", J. Nucl. Mater. **212-215** (1994) 168–174.

[36] H. Trinkaus, B. Singh, and A. Foreman, "Glide of interstitial loops produced under cascade damage conditions: possible effects on void formation", J. Nucl. Mater. **199** (1992) 1–5.

[37] H. Trinkaus, B. Singh, and S. Golubov, "Progress in modelling the microstructural evolution in metals under cascade damage conditions", J. Nucl. Mater. **283-287** (2000) 89–98.

[38] H. Wiedersich, "Implications of defect clusters formed in cascades on free defect generation and microstructural development", J. Nucl. Mater. **205** (1993) 40–51.

[39] B. Singh and J. Evans, "Significant differences in defect accumulation behaviour between fcc and bcc crystals under cascade damage conditions", J. Nucl. Mater. **226** (1995) 277–285.

[40] B. Singh, S. Golubov, H. Trinkaus, A. Serra, Y. Osetsky, and A. Barashev, "Aspects of microstructure evolution under cascade damage conditions", J. Nucl. Mater. **251** (1997) 107–122.

[41] M. Mathon, A. Barbu, F. Dunstetter, F. Maury, N. Lorenzelli, and C. de Novion, "Experimental study and modelling of copper precipitation under electron irradiation in dilute fecu binary alloys", J. Nucl. Mater. **245** (1997) 224–237.

[42] A. H. Duparc, C. Moingeon, N. S. de Grande, and A. Barbu, "Microstructure modelling of ferritic alloys under high flux 1 mev electron irradiations", J. Nucl. Mater. **302** (2002) 143–155.

[43] F. Christien and A. Barbu, "Effect of self-interstitial diffusion anisotropy in electron-irradiated zirconium: a cluster dynamics modeling", J. Nucl. Mater. **346** (2005) 272–281.

[44] R. Ning, Y. Li, W. Zhou, Z. Zeng, and X. Juc, "Modeling d retention in w under d ions and neutrons irradiation", J. Nucl. Mater. **430** (2012) 20–26.

[45] X. Hu, D. Xu, and B. D. Wirth, "Quantifying he-point defect interactions in fe through coordinated experimental and modeling studies of he-ion implanted single-crystal fe", J. Nucl. Mater. **442** (2013) S649S654.

[46] J. D. Torre, C.-C. Fu, F. Willaime, A. Barbu, and J.-L. Bocquet, "Resistivity recovery simulations of electron-irradiated iron: kinetic monte carlo versus cluster dynamics", J. Nucl. Mater. **352** (2006) 42–49.

[47] E. Meslin, A. Barbu, L. Boulanger, B. Radiguet, P. Pareige, K. Arakawa, and C. Fu, "Cluster-dynamics modelling of defects in a-iron under cascade damage conditions", J. Nucl. Mater. **382** (2008) 190–196.

[48] J. Marian and V. V. Bulatov, "Stochastic cluster dynamics method for simulations of multispecies irradiation damage accumulation", J. Nucl. Mater. **415** (2011) 84–95.

[49] D. Xu, B. D. Wirth, M. Li, and M. A. Kirk, "Combining in situ transmission electron microscopy irradiation experiments with cluster dynamics modeling to study nanoscale defect agglomeration in structural metals", Acta Mat. **60** (2012) 4286–4302.

[50] H. Trinkaus, V. Naundorf, B. Singh, and C. Woo, "On the experimental determination of the migrating defect fraction under cascade damage conditions", J. Nucl. Mater. **210** (1994) 244–253.

[51] W. M. Young and E. W. Elcock, "Monte carlo studies of vacancy migration in binary ordered alloys: i", Proc. Phys. Soc. **89** (1966) 735–746.

[52] A. B. Bortz, M. H. Kalos, and J. L. Lebowitz, "A new algorithm for monte carlo simulation of ising spin systems*", J. Comp. Phys. **17** (1975) 10–18.

[53] H. Heinisch and B. Singh, "Stochastic annealing simulation of differential defect production in high energy cascades", J. Nucl. Mater **232** (1996) 206–213.

[54] H. Heinisch and B. Singh, "Stochastic annealing simulation of intracascade defect interactions", J. Nucl. Mater **251** (1997) 77–85.

[55] H. Xu, Y. N. Osetsky, and R. E. Stoller, "Cascade annealing simulations of bcc iron using object kinetic monte carlo", J. Nucl. Mater. **423** (2012) 102–109.

[56] S. Plimpton, "Fast parallel algorithms for short-range molecular dynamics", J. Comp. Phys. **117** (1995) 1–19.

[57] G. J. Ackland, M. I. Mendelev, D. J. Srolovitz, S. Han, and A. V. Barashev, "Development of an interatomic potential for phosphorus impurities in α-iron", J. Physics: Condensed Matter **16** (2004) S2629.

[58] N. Juslin and K. Nordlund, "Pair potential for fehe", J. Nucl. Mater. **382** (2008) 143.

[59] A. Janzen and R. Aziz, "An accurate potential energy curve for helium based on ab initio calculations", J. Chem. Phys. **107** (1997) 914.

[60] J. F. Ziegler, J. P. Biersack, and U. Littmark, *The stopping and range of ions in matter* (Pergamon Press, New York, 1985).

[61] H. E. Schaefer, K. Maier, M. Weller, D. Herlach, A. Seeger, and J. Diehl, "Vacancy formation in iron investigated by positron annihilation in thermal equilibrium", Scripta Met. **11** (1977) 803–809.

[62] P. Hautojarvi, T. Judin, A. Vehanen, J. YliKauppila, J. Johanason, J. Verdone, and P. Moser, "Annealing of vacancies in electron-irradiated α-iron", Solid State Comm. **29** (1979) 855–858.

[63] J. Diehl, U. Merold, and M. Weller, "Information on vacancy migration in α-iron from annealing experiments", Scripta. Met. **11** (1977) 811–816.

[64] S. Takaki, J. Fuss, H. Kuglers, U. Dedek, and H. Schultz, "The resistivity recovery of high purity and carbon doped iron following low temperature electron irradiation", Radiation Effects **79** (1983) 87–122.

[65] H. Schultz, "Fe", in *The landolt-börnstein database*, edited by H. Ullmaier (Springer Materials).

[66] C. Domain and C. S. Becquart, "Ab initio calculations of defects in fe and dilute fe-cu alloys", Phys. Rev. B **65** (2001) 024103.

[67] M. Kiritani, H. Takata, K. Moriyama, and F. E. Fujita, "Mobility of lattice vacancies in iron", Philos. Mag. A **40** (1979) 779–802.

[68] C. Becquart and C. Domain, "Ab initio contribution to the study of complexes formed during dilute fecu alloys radiation", Nucl. Instrum. Methods B **202** (2003) 44–50.

[69] C. C. Fu, J. D. Torre, F. Willaime, J. L. Bocquet, and A. Barbu, "Multiscale modelling of defect kinetics in irradiated iron", Nature Mat. **4** (2005) 68–74.

[70] F. Djurabekova, L. Malerba, R. Pasianot, P. Olsson, and K. Nordlund, "Kinetics versus thermodynamics in materials modeling: the case of the divacancy in iron", Philos. Mag. **90** (2010) 2585–2595.

[71] H. Matsui, S Takehana, and M. W. Guinan, "Resistivity recovery in high purity iron after fission- and fusion-neutron irradiation", J. Nucl. Mater. **155-157** (1988) 1284–1289.

[72] C. Domain, C. S. Becquart, and J. Foct, "Ab initio study of foreign interstitial atom (c, n) interactions with intrinsic point defects in α-fe", Phys. Rev. B **69** (2004) 144112.

[73] C. J. Ortiz, M. J. Caturla, C. C. Fu, and F. Willaime, "Influence of carbon on the kinetics of he migration and clustering in α-fe from first principles", Phys. Rev. B **80** (2009) 134109.

[74] T. Jourdan, C. C. Fu, L. Joly, J. L. Bocquet, M. J. Caturla, and F. Willaime, "Direct simulation of resistivity recovery experiments in carbon-doped *alpha*-iron", Phys. Scr. **T145** (2011) 014049.

[75] K. Tapasa, A. Barashev, D. Bacon, and Y. Osetsky, "Computer simulation of carbon diffusion and vacancycarbon interaction in α-iron", Acta Mat. **55** (2007) 1–11.

[76] C. J. Forst, J. Slycke, K. J. V. Vliet, and S. Yip, "Point defect concentrations in metastable fe-c alloys", Phys. Rev. Lett. **96** (2006) 175501.

[77] D. Terentyev, Y. Osetsky, and D. Bacon, "Competing processes in reactions between an edge dislocation and dislocation loops in a body-centred cubic metal", Scripta. Mat. **62** (2010) 697–700.

[78] C. C. Fu, F. Willaime, and P. Ordejon, "Stability and mobility of mono- and di-interstitials in α-fe", Phys. Rev. Lett. **92** (2004) 175503.

[79] F. Willaime, C. Fu, M. Marinica, and J. D. Torre, "Stability and mobility of self-interstitials and small interstitial clusters in α-iron: ab initio and empirical potential calculations", Nucl. Instrum. Methods B **228** (2005) 92–99.

[80] R. A. Johnson, "Interstitials and vacancies in α iron", Phys. Rev. **134** (1964) A1329–A1336.

[81] B. Wirth, G. Odette, D. Maroudas, and G. Lucas, "Energetics of formation and migration of self-interstitials and self-interstitial clusters in α-iron", J. Nucl. Mater. **244** (1997) 185–194.

[82] D. A. Terentyev, L. Malerba, and M. Hou, "Dimensionality of interstitial cluster motion in bcc-fe", Phys. Rev. B **75** (2007) 104108.

[83] B. Wirth, G. Odette, D. Maroudas, and G. Lucas, "Dislocation loop structure, energy and mobility of self-interstitial atom clusters in bcc iron", J. Nucl. Mater. **276** (2000) 33–40.

[84] B. L. Eyre and R. Bullough, "On the formation of interstitial loops in b.c.c. metals", Philos. Mag. **12** (1965) 31–39.

[85] J. Marian, B. D. Wirth, and J. M. Perlado, "Mechanism of formation and growth of $\langle 100 \rangle$ interstitial loops in ferritic materials", Phys. Rev. Lett. **88** (2002) 255507.

[86] S. L. Dudarev, R. Bullough, and P. M. Derlet, "Effect of the $\alpha - \gamma$ phase transition on the stability of dislocation loops in bcc iron", Phys. Rev. Lett. **100** (2008) 135503.

[87] K. Arakawa, M. Hatanaka, E. Kuramoto, K. Ono, and H. Mori, "Changes in the burgers vector of perfect dislocation loops without contact with the external dislocations", Phys. Rev. Lett. **96** (2006) 125506.

[88] Y. Osetsky, D. Bacon, A. Serra, B. Singh, and S. Golubov, "Stability and mobility of defect clusters and dislocation loops in metals", J. Nucl. Mater. **276** (200) 65–77.

[89] Y. N. Osetsky, D. J. Bacon, A. Serra, B. N. Singh, and S. I. Golubov, "One-dimensional atomic transport by clusters of self-interstitial atoms in iron and copper", Philos. Mag. **83** (2003) 61–91.

[90] N. Soneda and T. D. de La Rubia, "Migration kinetics of the self-interstitial atom and its clusters in bcc fe", Philos. Mag. A **81** (2001) 331–343.

[91] K. Arakawa, K. Ono, M. Isshiki, K. Mimura, M. Uchikoshi, and H. Mori, "Observation of the one-dimensional diffusion of nanometer-sized dislocation loops", Science **318** (2007) 956.

[92] K. Tapasa, A. Barashev, D. Bacon, and Y. Osetsky, "Computer simulation of the interaction of carbon atoms with self-interstitial clusters in α-iron", J. Nucl. Mater. **361** (2007) 52–61.

[93] D. Terentyev, N. Anento, A. Serra, V. Jansson, H. Khater, and G. Bonny, "Interaction of carbon with vacancy and self-interstitial atom clusters in α-iron studied using metalliccovalent interatomic potential", J. Nucl. Mater **408** (2011) 272–284.

[94] N. Anento and A. Serra, "Carbonvacancy complexes as traps for self-interstitial clusters in fec alloys", J. Nucl. Mater. **440** (2013) 236–242.

[95] K. Arakawa, M. Hatanaka, H. Mori, and K. Ono, "Effects of chromium on the one-dimensional motion of interstitial-type dislocation loops in iron", J. Nucl. Mater. **329-333** (2004) 1194–1198.

[96] D. Terentyev, P. Olsson, L. Malerba, and A. Barashev, "Characterization of dislocation loops and chromium-rich precipitates in ferritic ironchromium alloys as means of void swelling suppression", J. Nucl. Mater **362** (2007) 167–173.

[97] Y. Satoh, H. Matsui, and T. Hamaoka, "Effects of impurities on one-dimensional migration of interstitial clusters in iron under electron irradiation", Phys. Rev. B **77** (2008) 094135.

[98] M.-C. Marinica, F. Willaime, and N. Mousseau, "Energy landscape of small clusters of self-interstitial dumbbells in iron", Phys. Rev. B **83** (2011) 049119.

[99] N Anento, A Serra, and Y. N. Osetsky, "Atomistic study of multimechanism diffusion by self-interstitial defects in α-fe", Modelling Simul. Mater. Sci. Eng. **18** (2010) 025008.

[100] D. J. Bacon, Y. N. Osetsky, and Z. Rong, "Computer simulation of reactions between an edge dislocation and glissile self-interstitial clusters in iron", Philos. Mag. **86** (2006) 3921–3936.

[101] A. Nomoto, N. Soneda, A. Takahashi, and S. Ishino, "Interaction analysis between edge dislocation and self interstitial type dislocation loop in bcc iron using molecular dynamics", Mater. Trans. **46** (2005) 463–468.

[102] Z. Rong, Y. N. Osetsky, and D. J. Bacon, "A model for the dynamics of loop drag by a gliding dislocation", Philos. Mag. **85** (2005) 1473–1493.

[103] J. B. Gibson, A. N. Goland, M. Milgram, and G. H. Vineyard, "Dynamics of radiation damage", Phys. Rev. **120** (1960) 1229–1253.

[104] B. Grant, J. M. Harder, and D. J. Bacon, "Interstitial-vacancy recombination for model bcc transition metals", J. Nucl. Mater. **171** (1990) 412–414.

[105] W. G. Wolfer and A. Si-Ahmed, "On the coefficient for bulk recombination of vacancies and interstitials", J. Nucl. Mater. **99** (1981) 117–123.

[106] M. Pelfort, Y. N. Osetsky, and A. Serra,

[107] M. Puigvi, Y. Osetsky, and A. Serra, "Interactions between vacancy and glissile interstitial clusters in iron and copper", Mat. Sci. Eng. **A365** (2004) 101–106.

[108] D. Terentyev and L. Malerba, "Interaction of $\langle 100 \rangle$ and $\langle 111 \rangle$ dislocation loops with point defects in ferritic alloys", J. Nucl. Mater. **377** (2008) 141–146.

[109] N. Anento and A. Serra, "Interaction of a single interstitial atom with small clusters of self interstitials in α-fe", J. Nucl. Mater. **372** (2008) 239–248.

[110] K. L. Wong, H.-J. Lee, J.-H. Shim, B. Sadigh, and B. D. Wirth, "Multiscale modeling of point defect interactions in fecr alloys", J. Nucl. Mater. **386-388** (2009) 227–230.

[111] P. Olsson, C. Domain, and J. Wallenius, "Ab initio study of cr interactions with point defects in bcc fe", Phys. Rev. B **75** (2007) 014110.

[112] P. Olsson, "Ab initio study of interstitial migration in fecr alloys", J. Nucl. Mater. **386-388** (2009) 86–89.

[113] D. Terentyev, P. Olsson, and L. Malerba, "Diffusion of 3d-migrating self-interstitial clusters in diluted and concentrated fecr alloys", J. Nucl. Mater. **386-388** (2009) 140–142.

[114] C. J. Ortiz and M. J. Caturla, "Cascade damage evolution: rate theory versus kinetic monte carlo simulations", J. Computer-Aided Mater. Des. **14** (2007) 171–181.

[115] C. Domain, C. Becquart, and L. Malerba, "Simulation of radiation damage in fe alloys: an object kinetic monte carlo approach", J. Nucl. Mater. **335** (2004) 121–145.

[116] M. Caturla, N. Soneda, E. Alonso, B. Wirth, T. D. de la Rubia, and J. Perlado, "Comparative study of radiation damage accumulation in cu and fe", J. Nucl. Mater. **276** (2000) 13–21.

[117] N. Soneda and T. D. de la Rubia, "Defect production, annealing kinetics and damage evolution in α-fe: an atomic-scale computer simulation", Philos. Mag. A **78** (1998) 995–1019.

[118] M. J. Norgett, M. T. Robinson, and I. M. Torrens, "A proposed method of calculating displacement dose rates", Nucl. Eng. Des. **33** (1975) 50–54.

[119] D. J. Bacon and T. D. de la Rubia, "Molecular dynamics computer simulations of displacement cascades in metals", J. Nucl. Mater. **216** (1994) 275–290.

[120] R. Stoller and A. Calder, “Statistical analysis of a library of molecular dynamics cascade simulations in iron at 100 k”, J. Nucl. Mater. **283-287** (2000) 746–752.

[121] R. Stoller, M. Toloczko, G. Was, A. Certain, S. Dwaraknath, and F. Garner, “On the use of srim for computing radiation damage exposure”, Nucl. Instrum. Methods B **310** (2013) 75–80.

[122] J.-H. Shim, H.-J. Lee, and B. D. Wirth, “Molecular dynamics simulation of primary irradiation defect formation in fe10%cr alloy”, J. Nucl. Mater. **351** (2006) 56–64.

[123] D. Terentyev, L. Malerba, R. Chakarova, K. Nordlund, P. Olsson, M. Rieth, and J. Wallenius, “Displacement cascades in fecr: a molecular dynamics study”, J. Nucl. Mater. **349** (2006) 119–132.

[124] R. Stoller, G. Odette, and B. Wirth, “Primary damage formation in bee iron”, J. Nucl. Mater. **251** (1997) 49–60.

[125] R. Stoller, “The role of cascade energy and temperature in primary defect formation in iron”, J. Nucl. Mater. **276** (2000) 22–32.

[126] W. Phythian, R. S. snd A.J.E. Foreman, A. Calder, and D. Bacon, “A comparison of displacement cascades in copper and iron by molecular dynamics and its application to microstructural evolution”, J. Nucl. Mater. **223** (1995) 145–261.

[127] L. Malerba, “Molecular dynamics simulation of displacement cascades in α-fe: a critical review”, J. Nucl. Mater. **351** (2006) 28–38.

[128] A. P. Selby, D. Xu, N. Juslin, N. A. Capps, and B. D. Wirth, “Primary defect production by high energy displacement cascades in molybdenum”, J. Nucl. Mater. **437** (2013) 19–23.

[129] K. Arakawa, H. Mori, and K. Ono, “Formation process of dislocation loops in iron under irradiations with low-energy helium, hydrogen ions or high-energy electrons”, J. Nucl. Mater. **307-311** (2002) 272–277.

[130] Y. Satoh and H. Matsui, “Obstacles for one-dimensional migration of interstitial clusters in iron”, Philos. Mag. **89** (2009) 1489–1504.

[131] T. Hamaoka, Y. Satoh, and H. Matsui, “One-dimensional motion of interstitial clusters in iron-based binary alloys observed using a high-voltage electron microscope”, J. Nucl. Mater. **433** (2013) 180–187.

[132] C. Topbasi and A. T. Motta, Unpublished results.

[133] A. Seeger and U. Gosele, “Steady-state diffusion of point defects to dislocation loops”, Phys. Lett. **61A** (1977) 423–425.

[134] C. Woo, “The sink strength of a dislocation loop in the effective medium approximation”, J. Nucl. Mater. **98** (1981) 279–194.

[135] H. Xu, R. E. Stoller, Y. N. Osetsky, and D. Terentyev, “Solving the puzzle of $\langle 100\rangle$ interstitial loop formation in bcc iron”, Phys. Rev. Lett. **110** (2013) 265503.

[136] C. Woo, “Theory of irradiation deformation in non-cubic meltals: effecis of anisotropic diffusion”, J. Nucl. Mater. **159** (1988) 237–256.

[137] V. Borodin, “Rate theory for one-dimensional diffusion”, Phisica A **260** (1998) 467–478.

[138] H. Heinisch, B. Singh, and S. Golubov, “The effects of one-dimensional glide on the reaction kinetics of interstitial clusters”, J. Nucl. Mater. **283-287** (2000) 737–740.

[139] A. Barashev, S. Golubov, and H. Trinkaus, “Reaction kinetics of glissile interstitial clusters in a crystal containing voids and dislocations”, Phil Mag. A **81** (2001) 2515–2532.

[140] H. T. B. Singh and S. Golubov, *A general treatment of one- to three-dimensional diffusion reaction kinetics of interstitial clusters: implications for the evolution of voids*, tech. rep. Ris-R-1644(EN) (Ris National Laboratory for Sustainable Energy, 2008).

[141] C. Becquart, A. Barbu, J. Bocquet, M. Caturla, C. Domain, C.-C. Fu, S. Golubov, M. Hou, L. Malerba, C. Ortiz, A. Souidi, and R. Stoller, “Modeling the long-term evolution of the primary damage in ferritic alloys using coarse-grained methods”, J. Nucl. Mater. **406** (2010) 39–54.

[142] A. Barbu, C. S. Becquart, J. Bocquet, J. D. Torre, and C.Domain, “Comparison between three complementary approaches to simulate large fluence irradiation: application to electron irradiation of thin foils”, Philos. Mag. **85** (2005) 541–547.

[143] R. Stoller, S. Golubov, C. Domain, and C. Becquart, “Mean field rate theory and object kinetic monte carlo: a comparison of kinetic models”, J. Nucl. Mater. **382** (2008) 77–90.

[144] M. Eldrup, B. Singh, S. Zinkle, T. Byun, and K. Farrell, “Dose dependence of defect accumulation in neutron irradiated copper and iron”, J. Nucl. Mater. **307-311** (2002) 912–917.

Appendix A

Implementation and Numerical Methods

A.1 Cluster Dynamics

The differential equations governing cluster population form a coupled reaction-diffusion system represented by Eq. (3.1). A cluster dynamics simulation is, in essence, nothing more than the process of numerically integrating these equation. The details of this integration have been deferred throughout the text, and are presented here instead. We outline the integration methods that were considered, discuss our selection among them, and outline some of the more important considerations regarding efficiency and optimization. Additionally, we discuss conservation of mass for the chosen integration scheme, and in CD generally.

A.1.1 Integration Scheme

When selecting an integration scheme it is important to consider the properties of the system of equations being solved. CD is one instance of a broader class of reaction-diffusion systems referred to as chemical or mass action kinetics problems. The numerical method ought to accommodate the properties of physical systems described by these equations, namely:

- negative densities are forbidden,
- matter is conserved and,
- the systems are usually stiff.

The last of these is particularly true of irradiation damage problems, where the mean lifetime of a single interstitial may be no more than a few nanoseconds, while the formation of microstructural features occurs on the order of minutes or hours in ion irradiation experiments, and months or years for materials in service conditions. As a general rule, this implies the use of implicit schemes, which in turn typically involve providing the Jacobian matrix for the system.

Cluster dynamics presents an additional complication, however, owing to the number of participants in the reaction network. Spanning the size range of interest may require thousands of clusters, each cluster may take more than one distinct state, and these equations may be discretized over dozens of spatial nodes. Complications arise not necessarily because the number of equations is overwhelming, but because the resultant reaction network is large and - in the case where most of the clusters are mobile - not particularly sparse. Consequently, the Jacobian matrix required for implicit solvers becomes quite large, even in sparse storage. The basic structure of this matrix is shown in Figure A.1.

It is primarily block diagonal, with a dense reaction block for each mesh point (n_m), with each block spanning a number of rows equal to the number of independent cluster species (n_c) where $n_c \gg n_m$. An adjacent block containing only diagonal entires which arise from the diffusion operator sits on either side of each reaction block. The reaction blocks may become sparse to some degree if only a small subset of clusters are mobile, but that is not the case generally, certainly not for the simulations in this work. Some care must be taken in formulating a solution method scalable to include desirable additional physics, such as additional cluster states which greatly increase the size of the reaction blocks, additional solution dimensions which increase the number of nodes, and so on.

It is tempting to use a scheme which skirts the construction of the Jacobian altogether. A semi-implicit approach might appear attractive for this reason, applying only the diffusion operator implicitly while allowing an explicit treatment of the reaction networks. Applying this to the master equation yields a scheme of the form

$$u^{t+1} - u^{t} = \Delta t \left(D\nabla^2 u^{t+1} - DSu^{t+1} + g - L(u^t) + G(u^t) \right) \tag{A.1}$$

which can be easily solved for the updated solution as

$$u^{t+1} = \left[I - D\Delta t \left(\nabla^2 - S \right) \right]^{-1} \left[u^t + \Delta t \left(g - L(u^t) + G(u^t) \right) \right] \tag{A.2}$$

and requires the inversion of $[I - D\Delta t\,(\nabla^2 - S)]$ only. For the one dimensional spatial discretization used in our simulations, this matrix is tri-diagonal and the system can be solved directly with relative ease. The reaction network, however, is sufficiently stiff in and of itself to render the semi-implicit approach unstable at relatively small step sizes, requiring on the order of 10^8 steps to span experimentally relevant dose increments.

Before abandoning such an approach entirely, we note that the form of these equations can be exploited to increase the stability of a semi-implicit scheme. While the reaction production term $G(u)$ is completely non-linear, the reaction depletion term $L(u)$ can be written in terms of a depletion rate multiplied by the concentration vector, $L(u) = \ell(u)u$. In this manner, the depletion terms can be handled implicitly according to a “linearized” Euler scheme,

$$u^{t+1} = \left[I - \Delta t \left(D\nabla^2 - DS - \ell(u^t) \right) \right]^{-1} \left[u^t + \Delta t \left(g + G(u^t) \right) \right] \tag{A.3}$$

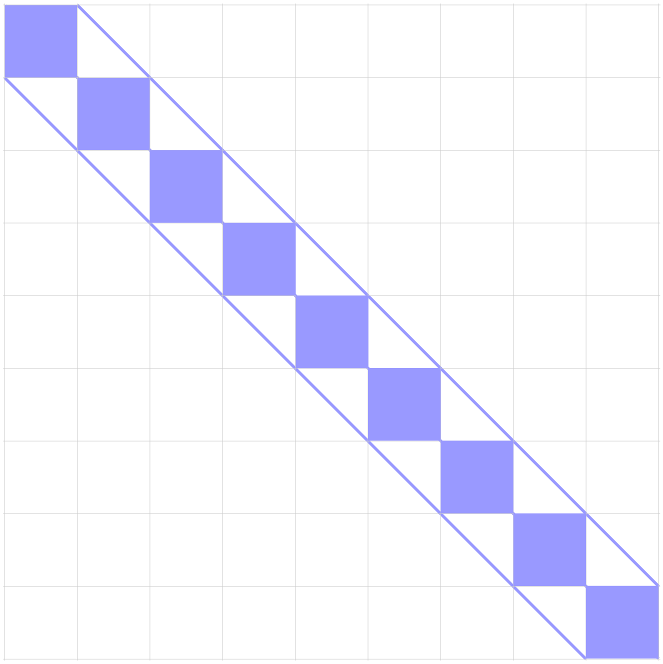

Figure A.1: Jacobain structure in cluster dynamics

for which the matrix to be inverted remains tri-diagonal, and only the magnitude of the components have changed from Eq. (A.2). As $\ell(u)$ and $G(u)$ are constrained by definition to contain only positive entries in mass action kinetics problems, this approach provides an unconditionally stable scheme. Though stable, this scheme violates a different requirement for the meaningful integration of a mass action kinetics problem in that it does not strictly conserve mass.

The alternative, a fully implicit method, requires the calculation of all rates from the right endpoint, u^{t+1}. The backward Euler method, for example, entails a solution of the form

$$u^{t+1} - u^t = \Delta t \left(D\nabla^2 u^{t+1} - DSu^{t+1} + g - L(u^{t+1}) + G(u^{t+1}) \right) \tag{A.4}$$

instead of Eq. (A.2). The solution at the right endpoint is not known when calculating the rates, demanding the use of some form of fixed point iteration, preferably Newton's method. Newton's method requires the system Jacobian which, as discussed earlier, is cumbersome in cluster dynamics. Obtaining exact solutions to Newton updates by inversion of the Jacobian is prohibitively expensive for large systems anyway, and Krylov subspace iterative methods can be used instead. It is not our intention to delve too deeply into the interior mechanics of these methods, but instead to discuss points pertaining to their application to cluster dynamics. In this light, we point out that there are two aspects to efficiently applying these methods, a way to obtain products of the Jacobian and an arbitrary vector, and some preconditioner.

The matrix vector products can be obtained either through an explicit construction of the Jacobian or by a pair of function evaluations to obtain a finite difference approximation of the Frechet derivative. The latter method, known as Jacobian Free Newton-Krylov (JFNK) is preferred, primarily because storing a full Jacobian becomes prohibitively memory intensive[1]. The preconditioning step requires more attention. In short, the purpose of preconditioning is to transform the problem $Ax = b$ by applying another matrix M in a manner similar to $A(M^{-1}M)x = b$. Ideally, the resultant problem $(AM^{-1})y = b$ is solved in fewer iterations than the original problem. For illustrative purposes, consider the limiting case of $M = A$, where the matrix (AM^{-1}) reduces to the identity and the problem is solved without further computation. Of course, the attraction of using iterative methods in the first place stems from difficulty supplying A^{-1}, in this case the Jacobian inverse, rendering such a choice of preconditioner impractical. Instead, some matrix merely similar to A will often suffice.

One such choice is $M = \text{diag}(A)$, the Jacobi preconditioner. In the context of a reaction-diffusion problem it is perhaps more appropriate to include the upper and lower diffusion blocks as well. The resultant tri-diagonal matrix problem equivalent to Eq. (A.3), and can be applied with equivalent ease. Another popular approach to preconditioning takes advantage of the fact that M need never be supplied explicitly, and only the action of M^{-1} is ever required. In this manner, an incomplete LU factorization (ILU) of the Jacobian can supply the action of M^{-1} without concern for the actual form of the corresponding matrix M. The reduction in the number of iterations required to reach convergence for ILU approaches weighs against an increased amount of time spent constructing the preconditioner. This is particularly true of cluster dynamics, where the dense reaction blocks suggest an expense that scales with $n_m \times n_c^3$ in the general case, which becomes prohibitive for realistic systems where n_c stretches easily into the tens of thousands[2].

Rather than using the full Jacobian, one might consider including only a few of the sub- and super-diagonals from each reaction block to to improve the tridiagonal preconditioning approach. Band-limiting the diagonal blocks in this manner significantly reduces the expense of ILU as well as the required storage. Such a preconditioner should at least be more effective than the tridiagonal approach, however there is a physical basis to suggest it is even more efficient than it first appears. The propagation of the solution through phase space (cluster growth) is driven primarily by monomers and other small clusters which have large source terms and high mobility. The Jacobian elements relevant to the interaction of these species

---

[1] The storage requirement for the Jacobian scales with $n_c^2 \times n_m$. The next largest storage requirement is the rate coefficient list which goes as n_c^2. Storing the Jacobian may actually become feasible for particularly low n_m, but is wasteful even in these cases.

[2] Storage also becomes a concern with ILU, and using the full Jacobian to form a preconditioner eliminates the advantages of JFNK.

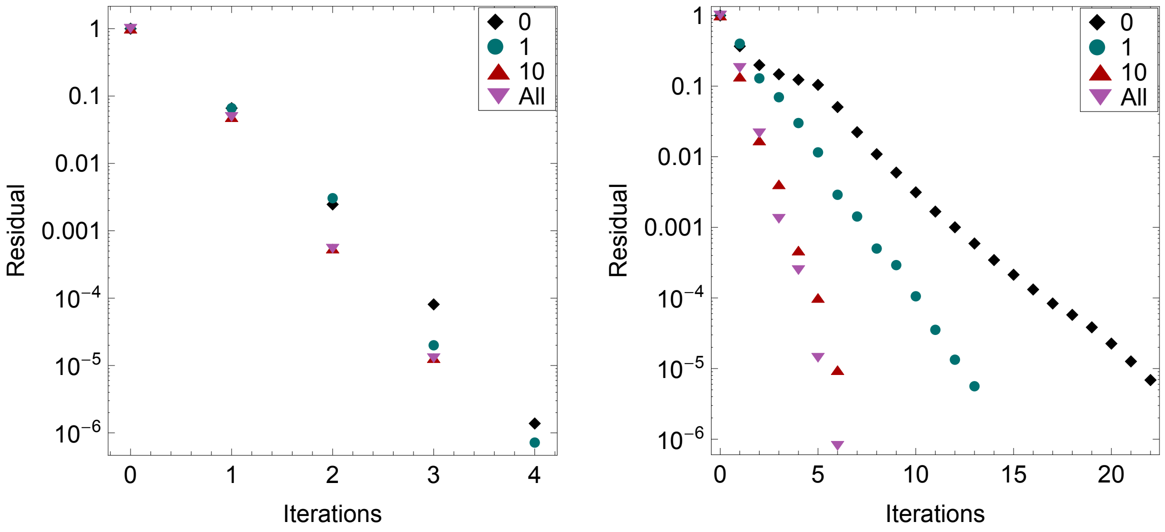

(a) 10^{-3} second timestep

(b) 1 second timestep

Figure A.2: Performance of various preconditioning approaches which include various numbers of sub- and super-diagonals from the reaction block

with the rest of the system lie near the diagonal, and are fully accounted for in a band-limited preconditioner.

The effectiveness of this approach is demonstrated in Figure A.2. Each of four different preconditioners is constructed from an ILU(0) factorization of some portion of the Jacobian. Various numbers of additional diagonals were included from the reaction blocks, alongside the limiting cases of a bare tridiagonal operator (no additional diagonals) and the full matrix (all diagonals). Differences in performance are not large at small time steps, but as the time step grows the sparser preconditioners begin to require more iterations to reach convergence. The bandwidth required to maintain acceptable performance up to large time steps is quite small in comparison to the number of equations, saving a great deal of time and storage over the full matrix approach.

Using approximately 10 diagonals from the reaction block to construct a preconditioner, the simulations easily run on a single processor, and can typically reach a few dpa in a matter of hours. In principle, higher order Rosenbrock or linear multistep methods can be implemented using the same iterative solution methods as backward Euler, however this is not immediately suitable for mass action kinetics problems. Backward Euler precludes the realization of negative concentrations within machine precision, which higher order methods do not. Application of such methods, if pursued, should be coupled with some manner of constraining the solutions to positive values[1].

Within the radiation damage literature, some concerns have been expressed over the conservation of mass in implicit approaches. Some researchers have advanced the notion that backward Euler integration will not conserve mass[2], though it appears that the authors envisioned an approach similar to Eq. (A.3) rather than backward Euler itself. To the contrary, it is a well known property of both Runge Kutta and linear multistep methods (backward Euler can be seen as either) that they preserve linear invariants such as mass[3]. This is true for implicit methods in principle, however in reality the solutions to non-linear systems require the use or iterative methods as discussed. Where a well converged Newton's method is used, the conservation properties are maintained, though this might not be the case for all iterative solution methods[4]. A demonstration that the conservation property is maintained in our implementation is presented below.

Defects introduced as primary damage have three possible fates in the master equation. They are either:

- retained as internal damage either alone or via absorption on another cluster,
- absorbed at internal sinks (network dislocations), or
- lost to the free surface.

As such, it might be said that in the thin foil simulations prevalent throughout this work, mass is not strictly a linear invariant, as the mass flowing into sinks and surfaces is not included explicitly in any of the concentration equations. We can account for this either by adding equations to track the defects absorbed in this manner, or by redefining the system to eliminate these possibilities. For example, the simulation can be performed on only one spatial node with no geometric leakage, eliminating free surface effects. Additionally, the sink density can be set to zero, prohibiting defect loss at internal sinks as well. We refer to these are "bulk" and "clean" simulations, respectively.

In any of these simulations, the internal mass content at any given moment can be calculated by simply integrating the defect concentration equations with respect to depth. Summing the mass of each clusterm_i multiplied by its integral concentration as

$$\Delta_r(t) = \sum_i \int_0^L m_i C_i(x,t) \mathrm{d}x \tag{A.5}$$

gives the mass retained as internal defects. In practice the integration must be performed numerically from node to node, and we invoke the trapezoid rule for this purpose. For a clean calculation, the retained mass is a linear invariant. In other cases, mass stored at sinks and boundaries must be considered.

The sink and boundary mass cannot be calculated on demand from the current populations. Rather, these must be found by integrating the flux of defects to sinks and surfaces respectively from $t = 0$. The net flux to internal sinks at each integration time step is determined by the sink strength, according to

$$\phi_i^s(t) = D_i S_i C_i(t) \tag{A.6}$$

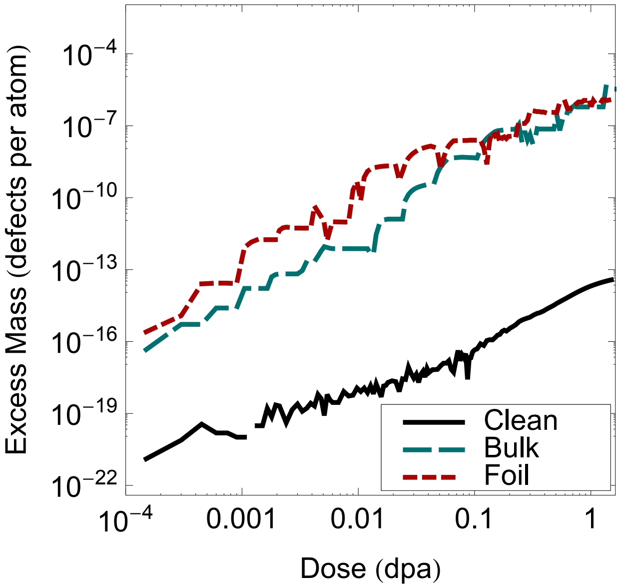

Figure A.3: Mass error as a function of dose

while the flux to boundaries can be calculated to first order using

$$\phi_i^b(t) = D_i \frac{C_i(x_1,t) - C_i(x_0,t)}{x_1 - x_0} \tag{A.7}$$

where x_0 is the surface node and x_1 is the nearest interior node. The excess masses then take the form

$$\Delta_s = \sum_i \int_0^t m_i \phi_i^s(\tau) \mathrm{d}\tau \tag{A.8}$$

for any arbitrary time t. When these are integrated by the same scheme as the rest of the equations, (i.e. backward Euler) the total mass stored in each of the three forms is conserved. Precise conservation of mass would suggest $\Delta_r + \Delta_s + \Delta_b = 0$, and the net excess mass $\epsilon = |\Delta_r + \Delta_s + \Delta_b|$ measures the extent to which conservation is violated. The progression of ϵ is demonstrated in Figure A.3 for various types of simulations.

In the calculations for a clean bulk system, the mass leakage remained below 10^{-13} defects per atom by 1 dpa, barely above machine precision. This is unsurprising, at least to us, and demonstrates our disregard for concerns about conservation of mass from integrating the master equation implicitly. Where sinks or free surfaces were included the error was several orders of magnitude larger. It is not immediately obvious to us why this is the case, though we suspect it involves the factors of m_i in the mass flux to sinks, which are not present in any components of the reaction network. Alternatively, the larger magnitudes could result from some failure of the JFNK approach to adequately conserve mass. There is no clear reason why such a failure would not affect the clean calculations as well, and this possibility seems unlikely.

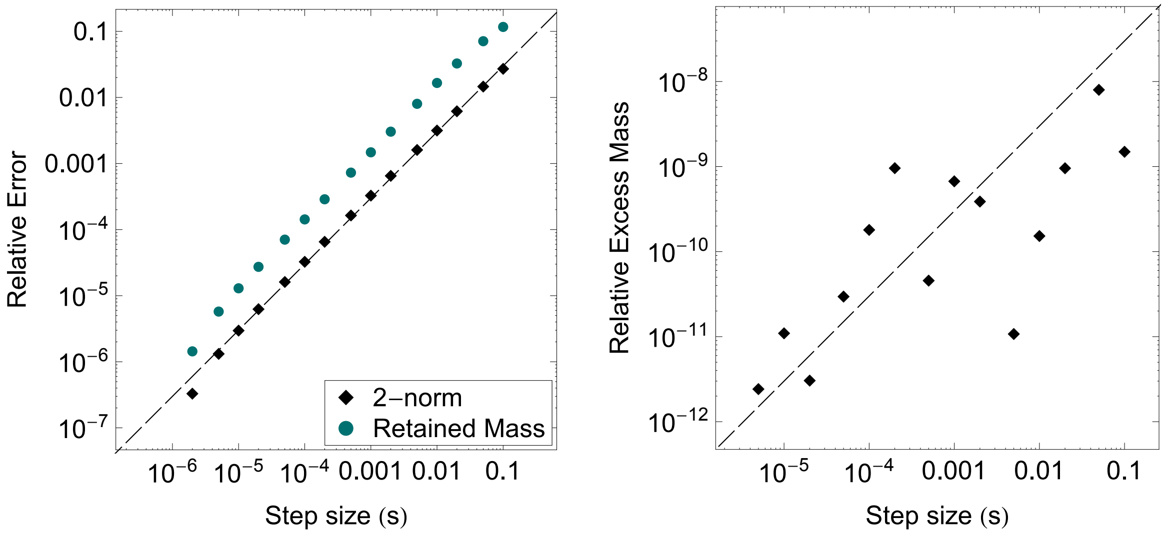

(a) Errors measured by the two norm and the retained mass

(b) Excess mass normalized to retained mass

Figure A.4: Global error at one second (0.0015 dpa) in bulk simulations using backward Euler integration with fixed time steps.

Nevertheless, to investigate this possibility we present the convergence behavior of the system at low doses for a bulk calculation with internal sinks. Figure A.4 shows how the global error at early times behaves with respect to integration step size, measured by several indicators. The first method finds the two norm of the error the numerical solution $||u^t - y(t)||_2 \, / \, ||y(t)||_2$, where the true solution $y(t)$ is estimated by the numerical integration with the shortest time steps. Alternatively, we present the error in the retained mass $|\Delta_r(u^t)/\Delta_r(y(t)) - 1|$. These indicators both converge on first order, as expected for this scheme for valid measurements of the global error. The net excess mass is shown as $\epsilon/\Delta_r(y(t))$, and exhibits a much lower magnitude and no clear convergence behavior. At a minimum, we can conclude that any violation of the conservation of mass is minute in comparison the accumulated errors in the solution itself.

The numerical approach outlined here has a number of advantages. Backward Euler has desirable stability properties and effectively constrains the solution to positive values. When the solutions are found with an effectively preconditioned JFNK technique, the scheme is quite efficient and the bulk of the computational time is spent performing function evaluations. The deviance from mass conservation is much smaller that the truncation errors with a method of this type. Finally, codes of this type are widely implemented, and means of controlling step size are well developed.

A.1.2 Function Evaluations

Each step in the integration process requires at least one direct evaluation of the entire PDE network. We will use the notation $f(u) = D\nabla^2 u - DSu + g - L(u) + G(u)$ to describe this process. As it occurs so frequently it is perhaps most crucial to the code's efficiency. This may not seem worth the trouble of extolling in detail. While applying operators such as ∇^2 is straightforward, computing the contributions of the reaction network to $f(u)$ requires more time and attention.

There are a number of conceivable systems for producing these terms. Perhaps the most intuitive is to directly reproduce the equations - as written on the page - as an algorithm, looping through the concentration vector and generating the entries of $f(u)$ one at a time. This approach is more complicated than it seems at first glance, and a series of special rules and exemptions must be introduced to make it applicable in practice. One might suppose that the implementation is as simple as algorithm A.1 but this is incorrect, and for a number of reasons.

Algorithm A.1 Simple concept for an element by element function evaluation

```
for i=1,nEq do
    $f(i) \leftarrow 0$
    for j=1,nEq do
        $f(i) \leftarrow f(i) - k0(i,j) \times u(i) \times u(j)$
        $m \leftarrow i - j$
        $f(i) \leftarrow f(i) + k0(j,m) \times u(j) \times u(m)$
    end for
end for
```

First, notice that for any given reaction $A + B \to C$ the production of C will be counted twice, once for $\{i = C, j = B\}$, and once for $\{i = C, j = A\}$. To prevent this, the interior loop must be split to separate gain and loss considerations. Each of the new loops require different bounds. Additionally, consider the case when the reactants are identical $A+A \to C$. In such an instance, where $i = j$, the loss rate must be doubled. Furthermore, it is not clear that all reactions are permitted by the phase space available to the problem. For example, no interstitials may be added to a loop already of the maximum size allowed by the problem. Such contributions must be explicitly rejected. Finally, the operation to produce the reactant pair represented in algorithm A.1 as $m = i - j$ is more complicated in general, particularly when additional cluster states are possible.

Considering these factors results in the much more complex and cumbersome Algorithm A.2. We note in passing that reaction networks in which the reaction rate coefficients are time dependent - as is the case for one dimensional diffusers - present additional complications. Furthermore, extracting the information required to construct a Jacobian is complex when approached this way. Instead our code applies all the rules pertaining to allowed reactions only once, to generate a list of valid reactions which is stored. With this information in

Algorithm A.2 Accurate element by element function evaluation

```
for $i = 1, nEq$ do
    $f(i) \leftarrow 0$
    for $j = 1, nEq$ do
        if allowed$(i, j)$ then
            if $i = j$ then
                $f(i) \leftarrow f(i) - 2 \times k0(i,j) \times u(i) \times u(j)$
            else
                $f(i) \leftarrow f(i) - k0(i,j) \times u(i) \times u(j)$
            end if
        end if
        $m \leftarrow$reaction_pair$(i, j)$
        if $j \leq m)$ then
            $f(i) \leftarrow f(i) + k0(j,m) \times u(j) \times u(m)$
        end if
    end for
end for
```

hand, the function evaluation proceeds via a reaction by reaction, rather than element by element as demonstrated in algorithm A.3.

Algorithm A.3 Reaction by reaction function evaluation

```
$f(:) \leftarrow 0$
for $i = 1, nReact$ do
    $dn \leftarrow k0(i) \times u(A_i) \times u(B_i)$
    $f(A_i) \leftarrow f(A_i) - dn$
    $f(B_i) \leftarrow f(B_i) - dn$
    $f(C_i) \leftarrow f(C_i) + dn$
end for
```

In addition to its increased simplicity, we expect the reaction by reaction approach to be more efficient and not merely for its absence of repeated rule evaluations. When cast in this form, it becomes clear that each rate of reaction appears exactly three times in the function evaluation. Though clear and easily exploited in Algortihm A.3, this simple fact is obscured in the element by element approach, resulting in a threefold increase in the number of computations of the form $k_{i,j}u_iu_j$. The reaction by reaction method can also be applied to constructing the Jacobian, if necessary, with similar advantages. As the rate coefficients are nominally independent of concentration, a given reaction only has non-zero derivatives with respect to the concentrations of the two reactants. Thus, to compute the Jacobian, algorithm A.4 will typically suffice, though the case where $A = B$ should in practice be handled slightly differently. A similar approach to both function evaluation and

Jacobian construction is employed for arbitrary cluster transformations of other forms, such as dissociation ($A \to B + C$) or state change($A \to B$).

Algorithm A.4 Reaction by reaction Jacobian construction

```
$J(:,:) \leftarrow 0$
for $i = 1, nReact$ do
    $dA \leftarrow k0(i) \times u(B_i)$
    $dB \leftarrow k0(i) \times u(A_i)$
    $J(A_i, A_i) \leftarrow J(A_i, A_i) - dA$
    $J(B_i, A_i) \leftarrow J(B_i, A_i) - dA$
    $J(C_i, A_i) \leftarrow J(C_i, A_i) + dA$
    $J(A_i, B_i) \leftarrow J(A_i, B_i) - dB$
    $J(B_i, B_i) \leftarrow J(B_i, B_i) - dB$
    $J(C_i, B_i) \leftarrow J(C_i, B_i) + dB$
end for
```

As mentioned earlier, one dimensional diffusion provides a somewhat different form of the reaction network. In this case, the rate coefficients k are not constant, and vary with the total obstacle density in the system. Consequently any implementation of the rate computations must be modified from the 3D formulations according to

$$R_{i,j} = \begin{cases} k_{i,j} u_i u_j & i \in \text{3D} \\ \frac{k^0_{i,j}}{\lambda_i(u)} u_i u_j & i \in \text{1D} \end{cases} \tag{A.9}$$

depending on the geometry of the particular reaction in question. Fortunately, this change involves only a computation of the mean free path for purely one dimensional reactions, which complicates the reaction algorithm only slightly. Constructing the Jacobian, by contrast, becomes significantly more complicated as λ_i varies not just in i and j but against the population even of defects not explicitly involved in the reaction as well. This dependence makes the formation of an exact analytical Jacobian untenable in in the one dimensional case as the number of calculations scales with n_c^3. By contrast, it is only twice as expensive as the function evaluation in the three dimensional case. Applicability to the general problem further motivates the use of JFNK, where the Jacobian is only needed for forming a preconditioner and need not be precise or even complete. Consequently, the higher order terms arising from the mean free path dependence can be safely neglected.

A.2 Object Kinetic Monte Carlo

The purpose of this section is to elucidate the aspects of the kinetic Monte Carlo simulation in this work that are specific to our implementation. As the residence time algorithm is well known and understood, along with its application in the framework of OKMC models, this will not be covered here. Instead, we will focus on the implementation of reaction conditions for defects and their clusters, which is sensitive to assumed reaction geometries. After each instance of a defect jump, that defect should be checked against each other to determine which reaction - if any - takes place. In practice, some grouping scheme should be employed to limit the number of these checks that must be performed at each step. In our implementation, the total volume is divided into smaller sub-volumes. Only those sub-volumes within a distance less than the maximum defect diameter are searched for possible reaction partners.

The simplest reaction volume is the isotropic one. This reaction volume is evident for reactions between two vacancy clusters or vacancy clusters and three dimensional interstitial clusters (those with three or fewer members in our parameterizations). Though extremely intuitive, we will describe this for completeness and to introduce notation that will be used in more complex scenarios. We first define the position of each of two reaction candidates as $\vec{r}_1$ and $\vec{r}_2$ where $\vec{r} = (x, y, z)$ and the vector $d\vec{r}$ describes the distance between them, $d\vec{r} = (dx, dy, dz) = \vec{r}_2 - \vec{r}_1$. In the isotropic case, the reaction condition is determined purely by the magnitude of $d\vec{r}$ exceeding the reactions radius $r_{1,2}$ such that $\sqrt{dx^2 + dy^2 + dz^2} \leq r_{1,2}$.

The reactions involving defects which are parameterized as dislocation loops are not as simple. In these cases, the defects have both a non-isotropic reaction volume and an inherent orientation. There are two possible interactions for defects of this type, those with isotropic defects and those with other non-isotropic defects. We will first discuss the former interaction. In this case, the reaction volume is implemented as a simple torus in the habit plane of the non-isotropic cluster. Determining whether a defect is positioned within such a reaction volume is a matter of computing the shortest euclidean distance to the dislocation line. In all cases, we assumed a habit plane perpendicular to the burgers vector, such that all habit planes were $\{111\}$.

The first step in determining whether an isotropic defect at $\vec{r}_2$ lie within a reaction volume for a non-isotropic defect at $\vec{r}_1$ was to rotate the co-ordinate system such that the torus lie in the x, y plane. This produces a new co-ordinate system in which $d\vec{r}_0 = \hat{R}_\alpha d\vec{r}$, where A is the rotation matrix that maps the $\{111\}$ habit plane of the loop in question onto the x, y plane. There are a total of 4 possible versions of $\hat{R}_\alpha$, one for each $\langle 111 \rangle$ orientation. In this co-ordinate sytem, the locus of points inside a toroidal reaction volume is identified trivially. The complete process is indicated in algorithm A.5, for a loop with radius r_1 and a defect with radius r_2.

Algorithm A.5 Procedure for determining whether a loop reacts with a point defect

```
$\vec{r}_0 \leftarrow \hat{R}_\alpha (\vec{r}_2 - \vec{r}_1)$
$s_0 \leftarrow \sqrt{x_0^2 + y_0^2}$
$d \leftarrow \sqrt{(s_0 - r_1)^2 + z_0^2}$
if $d \leq r_{core} + r_2$ then react
end if
```

The interaction of two non-isotropic clusters is more complex. In this case, the physics

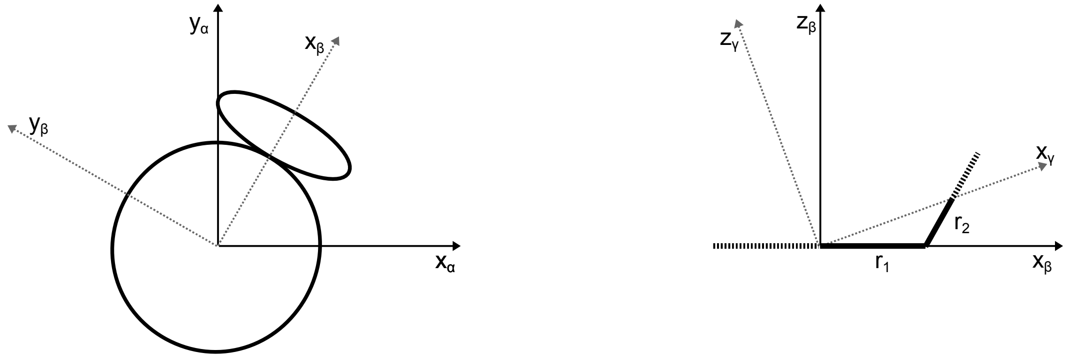

(a) Rotation about the z axis such that the glide direction is perpendicular to y

(b) Rotation about the y axis such that the reaction volume lies in the xy plane

Figure A.5: Coordinate rotations to facilitate checks for coalescence conditions between two dislocation loops.

requires both that dislocation lines overlap and that center of masses do not as discussed in Chapter 7. The reaction volume in this case is centered around the locus of points $\vec{r}_2$ that cause the periphery of two dislocation loops to touch but not cross one another. If the burgers vectors are parallel, these points form a circle in the shared habit plane of the two clusters and the reaction volume is a torus, similar to the previous conditions. Otherwise, these points are approximated by an ellipse, and the reaction volume consistent with the presentation in Chapter 7 is formed by the locus of points located no further than the coalescence radius away from that ellipse.

This reaction condition is more complex to impose, because the plane which the reaction volume lies on depends on the relative size of the loops in question. We impose a three step coordinate transform to map all possible reaction pairs onto more amenable coordinates, allowing evaluation of the reaction conditions. The first rotation is identical to the previous algorithm, leaving the primary loop in the xy plane. The second rotation $\hat{R}_\beta$ is applied about the z axis, such that the secondary loop glide direction lies in the xz plane. For each primary loop orientation, there are three possible secondary loop orientations, for a total of 12 separate instances of $\hat{R}_\beta$. The third rotation is applied about the y axis, such that the reaction volume lies in the xy plane. These coordinate rotations are illustrated in Figure A.5.

Following this procedure, the semi-minor axis of the reaction volume lies in the x direction and the semi-major axis lies in the y direction. The first two rotations are functions only of the loop Burgers vectors. The incline of the reaction volume to the habit plane of the primary loop depends on the size of the secondary loop, and thus the third rotation does as well. The point on the ellipse nearest the location of the secondary has the same angle with respect to the x axis as the secondary loop itself. Thus, the distance between the two points can be calculated, and if it is less than the coalescence distance r_d, a reaction occurs. This is illustrated in Algorithm A.6.

Algorithm A.6 Procedure for determining whether a loop reacts with another loop. The factor of 2/3 in the determination of the minor axis dimension is unique to loops both in {111} habit planes.

```
$b \leftarrow \sqrt{r_1^2 + r_2^2 + (2/3)r_1 r_2}$
$\vec{r}_0 \leftarrow \hat{R}_\gamma \hat{R}_\beta \hat{R}_\alpha d\vec{r}$
$s_0 \leftarrow \sqrt{x_0^2 + y_0^2}$
$dx \leftarrow x_0 - bx_0/s_0$
$dy \leftarrow y_0 - (r1 + r2)y_0/s_0$
if $dx^2 + dy^2 + z_0^2 \leq r_d^2$ then react
end if
```

References

[1] A Sandu, “Positive numerical integration methods for chemical kinetic systems”, J. Comput. Phys. **170** (2001) 589–602.

[2] M. Surh, J. Sturgeon, and W. Wolfer, “Master equation and fokkerplanck methods for void nucleation and growth in irradiation swelling”, J. Nucl. Mater. **325** (2004) 44–52.

[3] H. H. Robertson and M. J. McCann, “A note on the numerical integration of conservative systems of first-order ordinary differential equations”, Comput. J. (1968) 81.

[4] L. F. Shampine, “Linear conservation laws for odes”, Computers Math. Applic **35** (1998) 45–53.